

**UNIVERSITÀ DEGLI STUDI DI NAPOLI
FEDERICO II**



Dottorato di Ricerca in Ingegneria dei Materiali e delle Strutture
XXIII CICLO

***PORO-THERMOELASTIC DUALITY AND
FE-BASED STRATEGIES FOR THE ANALYSIS
OF BIOLOGICAL TISSUES***

Tutors

Prof. P.A. NETTI

Prof. M. FRALDI

Author

Claudia Cristiana Chiara Capone

TABLE OF CONTENTS

•	INTRODUCTION	
•	CHAPTER I - POROELASTICITY THEORY	
1.1	Introduction	p. 1
1.2	Constitutive Equations and Material Constants	p. 1
1.3	Darcy's Law	p. 5
1.4	Limiting cases	p. 7
1.5	Terzaghi's one dimensional consolidation	p. 8
•	CHAPTER II – BIOT'S MODEL EXTENSIONS: STEADY-STATE CASES	
2.1	Anisotropic Poroelastic Theory	p. 12
2.1.1	Introduction	p. 12
2.1.2	The stress-strain- pore pressure constitutive relation	p. 13
2.1.3	The fluid content-stress-pore pressure constitutive relation	p. 17
2.1.4	Darcy's Law	p. 20
2.1.5	The matrix material and pore fluid incompressibility constraints for poroelasticity	p. 20
2.1.6	The undrained elastic coefficients	p. 24
2.1.7	Expression of mass and momentum conservation	p. 26
2.1.8	The basic equations of poroelasticity	p. 27
2.1.9	The basic equation of incompressible poroelasticity	p. 29
2.1.10	Compressible and incompressible constituents in anisotropic poroelasticity: The problem of unconfined compression of a disk	p. 30
2.2	Isotropic poroelastic models with non linear permeability and elasticity	p. 43
•	CHAPTER III – UNIFIED MIXTURE THEORY	
3.1	Mixture Theory	p. 49

3.1.1	Introduction	p. 49
3.1.2	Kinematics of mixtures	p. 51
3.1.3	The conservation laws for mixture	p. 55
3.2	Biphasic Theory	p. 61
3.2.1	Introduction	p. 61
3.2.2	Balance equations	p. 62
3.2.3	Constitutive Equations	p. 65
3.2.4	Confined Compression	p. 65
	• CHAPTER IV – POROELASTICITY – THERMOELASTICITY DUALITY (PTD)	
4.1	Introduction	p. 68
4.2	Coupled non - linear poroelastic problem	p. 69
4.3	Coupled non - linear thermoelastic problem	p. 71
4.4	Coupling between poroelasticity and thermoelasticity	p. 72
4.5	On the influence of coupling terms in poroelasticity and thermoelasticity	p. 75
	• CHAPTER V – REMARKS ON THE FINITE ELEMENT METHOD	
5.1	The Finite Element Method (FEM)	p. 83
5.2	The finite element modeling package ANSYS®	p. 86
5.3	Element Solid70	p. 88
5.3.1	Input Data	p. 89
5.3.2	Output Data	p. 91
	• CHAPTER VI – FEM APPLICATIONS	
6.1	Introduction	p. 92
6.2	Drug delivery to solid tumors	p. 92
6.2.1	Introduction	p. 92
6.2.2	FE model of drug delivery to solid tumors	p. 96
6.3	The role of osteon microstructure in bone growth and remodeling	p. 105
6.3.1	Introduction	p. 105
6.3.2	FE simulation of a typical osteon unit	p. 108

- **APPENDIX**
- A.1 **Geometry and morphological features of osteons** p. 117
- A.2 **Derivation of the overall mechanical behavior of osteons from their Microstructure** p. 119
 - A.2.1 Local material properties at the lamella level p. 119
 - A.2.2 Overall material properties at the osteonal level p. 120
- A.3 **Sensitivity analysis for the out-of-diagonal block coefficients** p. 121
- A.4 **The role in mechanoregulation of osteonal spiraling twisting** p. 126
- A.5 **Analytical Poroelastic solution for a solid FGMC composed by two phases under radial pressure** p. 132

- **CHAPTER VII – CONCLUSIONS AND FUTURE PERSPECTIVES**
- 7.1 **Conclusions** p. 138
- 7.2 **Future Perspectives** p. 138

- **REFERENCES**

INTRODUCTION

Poroelasticity is a continuum theory for the analysis of porous media consisting of an elastic matrix containing interconnected fluid-saturated pores. The presence of a freely moving fluid in a porous medium influences its mechanical properties. In physical terms, the theory postulates that when a porous material is subjected to stress, the resulting matrix deformation leads to volumetric changes in the pores. Since the pores are fluid-filled, the presence of the fluid not only acts as a stiffener of the material, but also results in the flow of the pore fluid (diffusion) between regions of higher and lower pore pressure. If the fluid is viscous the behavior of the material system becomes time dependent. Two mechanisms play a crucial role in the interaction between the fluid and the solid matrix: (i) an increase of pore pressure induces a dilation of the solid matrix and (ii) a compression of the solid matrix causes a rise of the pore pressure, if the fluid cannot escape the pore network. These coupled mechanisms confer an apparent time-dependent character to the mechanical properties of a porous medium. Moreover, if the excess pore pressure caused by the compression of the solid matrix can dissipate through diffusive fluid mass transport, then the solid matrix experiences further deformation.

The poroelasticity theory was born in geomechanics applications to describe soils behavior. In 1923, Terzaghi proposed a model of one dimensional consolidation to analyze the influence of pore fluid on soil deformation, but the first author who introduced a complete theory of linear poroelasticity was Biot in his papers (in 1935 and 1941), dealing with soil consolidation (quasi-static) and wave propagation (dynamic) problems in geomechanics. Moreover, Biot noted also the complete mathematical analogy between poroelastic and thermoelastic problems. Poroelasticity has been widely used also to model biological tissues, such as bone, cartilage, arterial walls, brain and osteons, because almost all tissues have an interstitial fluid in their pores. The interstitial fluid plays the role of actor in many crucial functions, like the transport of nutrients from the vasculature to the cells in the tissue or of waste products for removal. In some tissues, the pore fluid pressure creates a turgor that stiffens a soft tissue structure, and in other tissues it is part of the intercellular communication system. In tissues, deformation of the porous medium has a significant effect on the movement of pore fluid, although fluid pressure and fluid

movement generally have only a small effect on deformation of the porous medium. Cowin (Cowin, 1999) described fluid flow in bone tissue employing the poroelasticity theory. Bone, in fact, behaves like certain porous rocks. Bone deformation causes the interstitial fluid flow, a key element for bone adaptation and survival. Also cartilage can be modeled employing the poroelasticity theory. One of the most important functions of the fluid in articular cartilage is to lubricate joints and, thus, protect them from wearing. The mechanism of the fluid flow in bone and cartilage is so 'designed' to protect the biological structure from damage resulting from dynamic loading. Basser (Basser, 1992) described, instead, brain tissue employing the poroelasticity theory. Also, this theory results a fundamental tool in the analysis of fluid and macromolecular transport in solid tumors (Netti et al., 1995). Poroelasticity theory has been recently employed to describe remodeling processes and interstitial fluid transport in osteons (Yoon and Cowin, 2008, Rémond et al. 2008). Many analytical and numerical approaches have been proposed in order to solve poroelastic problems describing the behavior of biological tissues. The main difficulty associated to numerical strategies concerns the solution of the *coupled* poroelastic equations for determining the solid response in terms of deformation and filtration. The proposal of this work is to find a strategy to numerically solve poroelastic problems employing the Finite Element Method (FEM). In particular, the strategy presented is based on the well known similarity between thermoelasticity and poroelasticity theories. This analogy allows to solve transient poroelastic problems as corresponding thermoelastic ones, interpreting the temperature as a pressure and thermal gradients as velocities. With this aim, the relationship between thermoelasticity and poroelasticity is formulated in terms of dimensionless parameters to ensure numerical stability, because the elasticity moduli, filtration coefficients and porosity have essentially different orders of magnitude. Thus, the dimensionless equations obtained are implemented in numerical FEM-based computations. Such transferring to equivalent thermoelastic problems enables to apply the FEM package ANSYS[®] 11, which provides opportunities to solve coupled thermoelastic problems in transient non linear settings. The PhD dissertation is organized into seven sections. In Chapter I, the basic equations of the classical poroelasticity theory, first developed by Biot, are preliminarily presented. This theory has been, then, extended to take into account also isotropic models with anisotropic permeability and/or non linear elasticity, as illustrated in Chapter II. Chapter III, instead, is an overview on the mixture theory, another important instrument to describe the behavior of porous media. To this purpose, the basic differences between the two theories are

illustrated. In Chapter IV, the poroelastic - thermoelastic duality theory is fully developed by recollecting and summarizing a number of approaches. As highlighted before, this chapter represents the fulcrum of this thesis, because by exploiting the similarities between thermoelasticity and poroelasticity theories, many otherwise insurmountable poroelastic problems can be completely approached by standard FE protocols. Chapter V is an overview on the Finite Element Method (FEM) and on the above mentioned code ANSYS[®]. Chapter VI describes two example applications, solved with the software ANSYS[®] 11. The first one is concerning a very important problem of drug delivery in solid tumors. The second example is, instead, related to the investigation of the role played by trigonal-like microstructure in osteons in bone adaptive, growth and remodeling processes. Finally, Chapter VII illustrates the conclusions and the future perspectives.

CHAPTER I

POROELASTICITY THEORY

1.1 Introduction

Poroelasticity theory allows the study of the behavior of fluid-saturated elastic porous media. A porous material is a solid containing an interconnected network of pores (voids) filled with a fluid (liquid or gas). The solid matrix and the pore fluid are supposed to be continuous, forming two interpenetrating continua (e.g., a sponge). The Biot formulation of the constitutive equations for a fluid-filled porous material started with the introduction of two new variables: the pore pressure, p , representing another stress component, and the variation in fluid content, ζ , which is a strain component. ζ represents the volume of fluid added or removed from a control volume and, so, the increment in fluid content is, essentially, the “fluid strain”. Poroelasticity theory is based on two fundamental hypothesis. First of all, there is a linear relationship between the stress, $(\boldsymbol{\sigma}, p)$, and the strain, $(\boldsymbol{\varepsilon}, \zeta)$, and the deformation process is supposed irreversible, that is to say that no energy is dissipated during a closed loading cycle. The linear constitutive equations can, thus, be obtained by extending the classical elasticity theory, taking into account the new introduced variables. Moreover, poroelasticity theory includes also the Terzaghi’s Principle of Effective Stress, i.e. the total stress in a given point is the sum of the solid stress and the contribute of the pore pressure.

1.2 Constitutive Equations and Material Constants

There are several ways to formulate the constitutive equations of poroelasticity, based on the possibility to select different sets of independent variables. The constitutive equation stress-strain for a linear anisotropic poroelastic continuum is

$$\boldsymbol{\sigma} = \mathbb{C} : \boldsymbol{\varepsilon} - \boldsymbol{\alpha} p \quad (1.1)$$

where $\boldsymbol{\sigma}$ and $\boldsymbol{\varepsilon}$ are the second order stress and strain tensor, respectively, \mathbb{C} is the fourth rank tensor of the elastic constants, describing the constitutive properties of the solid matrix, $\boldsymbol{\alpha}$ is the *Biot- Willis coefficient*, defined in the following and p is the pore pressure.

Without considering the pore pressure, equation (1.1) degenerates in the classical elastic relationship. The coefficient α can be different in the three spatial directions. In the hypothesis of isotropy, $\boldsymbol{\alpha} = \alpha \mathbf{I}$.

The strain-stress equation is, instead,

$$\boldsymbol{\varepsilon} = \mathbf{S} : (\boldsymbol{\sigma} + \boldsymbol{\alpha} p) \quad (1.2)$$

where \mathbf{S} is the fourth rank tensor of the compliance constants. Considering the pore pressure as the coupling term, for an isotropic medium, equation (1.1) simplifies in

$$\boldsymbol{\sigma} = 2\mu_{solid} \boldsymbol{\varepsilon} + \lambda_{solid} e \mathbf{I} - \alpha p \mathbf{I} \quad (1.3)$$

where μ_{solid} and λ_{solid} are the Lamé's constants of the solid matrix, \mathbf{I} is the identity tensor and e is the trace of the strain tensor. It has to be noticed that the term $\boldsymbol{\sigma} + \alpha p \mathbf{I}$ plays the role of an effective stress. The coefficient α is often interpreted as an effective stress coefficient. The strain-stress equation is, instead

$$2\mu_{solid} \boldsymbol{\varepsilon} = \boldsymbol{\sigma} - \frac{v}{1+v} tr \boldsymbol{\sigma} \mathbf{I} + \frac{\alpha(1-2v)}{1+v} p \mathbf{I} \quad (1.4)$$

where v is the Poisson's coefficient of the solid matrix. If, instead, the variation in fluid content, ζ , is used as coupling parameter, the constitutive equations become

$$2\mu_{solid} \left(\boldsymbol{\varepsilon} - \frac{B}{3} \zeta \mathbf{I} \right) = \boldsymbol{\sigma} - \frac{v_u}{1+v_u} tr \boldsymbol{\sigma} \mathbf{I} \quad (1.5)$$

$$\boldsymbol{\sigma} = 2\mu_{solid} \boldsymbol{\varepsilon} + \frac{2\mu_{solid} v_u}{1-2v_u} e \mathbf{I} - \alpha M \zeta \mathbf{I} \quad (1.6)$$

The term $2\mu_{solid} \left(\boldsymbol{\varepsilon} - \frac{B}{3} \zeta \mathbf{I} \right)$ represents the effective strain, B is the *Skempton's coefficient*, defined in the following and v_u is the undrained Poisson's coefficient.

The introduction of the pore pressure / variation in fluid content into the constitutive equation needs the use on another equation to solve the problem. The continuity equation

will be used to this purpose. The response of the pore fluid can be modeled through two different equations.

For an isotropic medium,

$$2\mu_{solid}\zeta = \frac{\alpha(1-2\nu)}{1+\nu} \left(tr\boldsymbol{\sigma} + \frac{3}{B}p \right) \quad (1.7)$$

or

$$p = \frac{K_u B}{\alpha} (\zeta - \alpha e) \quad (1.8)$$

The coefficient α is the *Biot–Willis coefficient*, defined as

$$\alpha \equiv \left. \frac{\partial \zeta}{\partial e} \right|_{p=const} = \frac{K}{H} \quad (1.9)$$

It represents the ratio of fluid added to the change in *bulk* volume (e is the dilatation, associated to the volumetric change in the solid matrix). Furthermore, K is the drained bulk modulus, $\left(\lambda_{solid} + \frac{2}{3}\mu_{solid} \right)$, and $1/H$ is the poroelastic expansion coefficient, which measures the change in the variation of fluid content respect to a change in the average applied stress at constant pore pressure.

A key feature of the response of fluid-infiltrated porous material is the difference between undrained and drained cases, representing limiting behaviors of the material. The undrained case refers to the condition where the fluid is trapped in the porous solid and, thus, $\zeta = 0$. The drained case, instead, is characterized by a zero pore pressure, $p = 0$.

B is, instead, the *Skempton's coefficient*, given by

$$B \equiv - \left. \frac{\partial p}{\partial \sigma} \right|_{\zeta=const} = - \left. \frac{\partial e}{\partial \zeta} \right|_{T=const} = \frac{R}{H} \quad (1.10)$$

Skempton's coefficient measures how load is distributed between the solid and the fluid and its value is a number between zero and one. It tends to one for completely saturated materials (i.e., load is shared by pores filled completely with fluid) while it tends to zero for void space pores (e.g., highly compressible gases), as the solid framework must support

all the load. Furthermore, $1/R$ is the *unconstrained specific storage coefficient*. It tends to zero for an incompressible fluid, because a large increase in fluid pressure will cause an insignificant increase in fluid volume. R and H characterize the coupling between the solid and fluid stress and strain. Finally, K_u is the *undrained bulk modulus*, defined as

$$K_u \equiv \left. \frac{\partial \sigma}{\partial \varepsilon} \right|_{\zeta = \text{const}} = \frac{K}{1 - \alpha B} \quad (1.11)$$

and it varies in $[K, \infty]$. The bulk moduli have their familiar interpretation of the change in volume under hydrostatic pressure. The last parameter to be defined is the *constrained specific storage coefficient*, S_E ,

$$S_E = \left. \frac{\partial \zeta}{\partial p} \right|_{e = \text{const}} = \frac{1}{M} = \frac{\alpha}{K_u B} \quad (1.12)$$

and it represents the ratio of the variation in fluid content respect to a change in pore pressure under different conditions. M is the *Biot modulus*.

In the undrained condition, the volumetric strain, e , is directly proportional to pressure,

$$e = -\frac{p}{K_u B} \quad (1.13)$$

In the drained condition, $p = 0$, equation (1.7) becomes

$$\zeta = \alpha e \quad (1.14)$$

Equation (1.14) underlines that the coefficient α represents the ratio of the fluid gained (or lost) in a material element to the volume change of that element, when the pore pressure returns to its initial state. Moreover, α cannot exceed the unity because the volume of fluid gained (or lost) by an element cannot overgrow the total volume change of that element. α varies in $[0, 1]$. The undrained and drained conditions represent also the instantaneous and the long term behavior of a poroelastic medium, subjected to a suddenly applied loading. For example, if a step loading is applied to a poroelastic medium, the pore fluid does not have the possibility to flow between neighboring material elements, hence $\zeta = 0$. After a long time, instead, the pore pressure will equilibrate with the pore pressure imposed at the

boundary. If this pore pressure is zero, the long-term response of the material will be characterized by the disappearance of the pore pressure everywhere, i.e. $p = 0$. Undrained response denotes, thus, conditions where the characteristic time scale of the loading is too short to allow fluid movement to take place between material elements by diffusive mass transport, while drained response characterizes conditions where the pore pressure has returned to its original value.

1.3 Darcy's Law

Darcy's law is a constitutive equation describing the flow of fluid through a porous medium. It was empirically deduced by Darcy in the latter part of the 19th century during his experiments on the flow of water through sand, but it can be also derived from Navier-Stokes equations by dropping the inertial terms. It has been shown that, though having limitations, Darcy's law is valid for Newtonian liquids at low velocities and, thus, Darcy's law has often been employed in the study of the flow of biological fluids through tissues. According to Darcy's law, the fluid flux is directly proportional to the permeability of the material through which the fluid is flowing and the pressure gradient driving the flow, while it is inversely proportional to the fluid viscosity. Mathematically,

$$\mathbf{q}_{fluid} = -\frac{1}{\mu_{fluid}} \mathbf{K}_p (\nabla p - \rho \mathbf{g}) \quad (1.15)$$

where μ_{fluid} is the fluid viscosity, ρ is the fluid density, \mathbf{g} is the gravity acceleration and the minus sign ensures that fluid flows from high to low pressure. The tensor \mathbf{K}_p is the anisotropic permeability tensor, because the permeability of the solid through which the fluid is flowing is not necessarily the same in all directions. In the hypothesis of isotropy respect to the permeability, $\mathbf{K}_p = \kappa \mathbf{I}$, where κ is a constant. The permeability has dimension of length squared and it is related to the pore geometry. It depends strongly on the porosity, defined as $\phi = \frac{V_{fluid}}{V_{tot}}$. The permeability is generally linked to the porosity through a power law, strictly depending on pore geometry. Finally, the fluid velocity within the pores is related to the flux by the porosity.

The fluid velocity is

$$\mathbf{v} = \frac{\mathbf{q}_{fluid}}{\phi} \quad (1.16)$$

The flux is divided by porosity to take into account that only a fraction of the total volume is available for flow.

Assuming that the material properties have been measured, the unknowns of a poroelastic problem result 11: six stress components, three displacement components (yielding six strains), one pore pressure, and one increment of fluid content. Hence, 11 equations need to solve the problem: seven constitutive equations (six stress and one increment of fluid content), three force equilibrium equations (one for each direction), and one fluid continuity equation.

The momentum equation is

$$\nabla \cdot \boldsymbol{\sigma} = -\mathbf{b} \quad (1.17)$$

where \mathbf{b} are the body forces in the three directions. The continuity equation for the fluid phase is

$$\frac{\partial \zeta}{\partial t} = -\nabla \cdot \mathbf{q}_{fluid} + Q(\underline{x}, t) \quad (1.18)$$

where $Q(\underline{x}, t)$ represents a source term.

Substituting Darcy's law and equation (1.8) in equation (1.18) and neglecting inertial effects and the source term, yields to

$$\alpha \frac{\partial e}{\partial t} = -\frac{1}{M} \frac{\partial p}{\partial t} + \frac{\kappa}{\mu_{fluid}} \Delta p \quad (1.19)$$

Equation (1.19) is an heat equation in p .

Thus, the system passes through a sequence of equilibrium states; however, this path is irreversible due to frictional drag loss as the fluid flows past the solid matrix. As will be shown below, using a displacement–pressure formulation results in a system of four

coupled equations (by substituting the strain–displacement, Darcy’s law, and the constitutive relationships into the conservation equations) with the unknowns being three displacements and one pore pressure. Coupling of the equations comes from the pressure (p) term in the equations of force equilibrium and from the volumetric strain (e) in the fluid flow equation.

1.4 Limiting cases

If the solid matrix is incompressible, then $\alpha = 1$. For an infinite incompressible fluid, instead, $B = 1$ and $K_u = \infty$. Combining these two assumptions, $\frac{1}{M} = 0$ and $\zeta = e$. In this case, then, the volumetric change of the solid matrix is equal to the volume of the fluid exchanged. Under these assumptions, equation (1.19) becomes

$$\frac{\partial e}{\partial t} = \frac{\kappa}{\mu_{fluid}} \Delta p \quad (1.20)$$

Equation (1.20) is the statement that the time rate of change of the dilatation is equal to the time rate of change of the increment of fluid content. If both the solid and fluid are incompressible, any movement of an incompressible fluid into a space must correspondingly increase the volume (i.e., dilatation) of that space. It is important to recognize that the assumption of incompressible solid and fluid components does not mean that loading will not cause deformation of the tissue. Indeed, compressive loading leads to relative motion between the solid and fluid, whereby the pore size changes as fluid is effluxed from the material due to pressure gradients. Concomitantly, the solid network experiences a collapse in size as it comes to occupy the space previously occupied by the fluid.

1.5 Terzaghi's one dimensional consolidation

The classical one dimensional consolidation problem of Terzaghi (Terzaghi, 1943) is analyzed employing the poroelasticity theory. A soil layer of thickness L , resting on a rigid impermeable base is subjected to a constant load, applied through a permeable platen on the free surface. x_3 indicates the direction of nonzero strain and, so, $\varepsilon_{11} = \varepsilon_{22} = 0$ and $\varepsilon_{33} = \varepsilon$. Equation (1.3), thus, becomes

$$\sigma_{33} = (\lambda_{solid} + 2\mu_{solid})\varepsilon - \alpha p \quad (1.21)$$

Equation (1.19) can be written as

$$\frac{1}{M} \frac{\partial p}{\partial t} - k \frac{\partial^2 p}{\partial x_3^2} = -\alpha \frac{\partial \varepsilon}{\partial t} \quad (1.22)$$

where $k = \frac{\kappa}{\mu_{fluid}}$ and $e = \varepsilon$. The term $\frac{\partial \varepsilon}{\partial t}$ can be evaluated from equation (1.21)

$$\frac{\partial \varepsilon}{\partial t} = \frac{1}{(\lambda_{solid} + 2\mu_{solid})} \frac{\partial \sigma_{33}}{\partial t} + \frac{\alpha}{(\lambda_{solid} + 2\mu_{solid})} \frac{\partial p}{\partial t} \quad (1.23)$$

Replacing equation (1.23) in equation (1.22), the following relationship is obtained

$$\frac{1}{M} \frac{\partial p}{\partial t} - k \frac{\partial^2 p}{\partial x_3^2} = -\frac{\alpha}{(\lambda_{solid} + 2\mu_{solid})} \frac{\partial \sigma_{33}}{\partial t} - \frac{\alpha^2}{(\lambda_{solid} + 2\mu_{solid})} \frac{\partial p}{\partial t} \quad (1.24)$$

Neglecting the body forces, the momentum balance equation reduces to

$$\frac{\partial \sigma_{33}}{\partial x_3} = 0 \quad (1.25)$$

σ_{33} , thus, does not depend on x_3 and, so, the partial derivative with respect to time can be replaced with the total time derivative. Equation (1.24) is rewritten as

$$\frac{\partial p}{\partial t} - C_1 \frac{\partial^2 p}{\partial x_3^2} = -C_2 \frac{d\sigma_{33}}{dt} \quad (1.26)$$

where the material coefficients have been collected in C_1 and C_2 .

If a step load is applied to the loading platen, i.e. at $t = 0$ $\sigma_{33} = -\frac{F}{A}H(t)$, for all times greater than $t = 0^+$, $\frac{d\sigma_{33}}{dt} = 0$.

Equation (1.26), then, becomes

$$\frac{\partial p}{\partial t} = C_1 \frac{\partial^2 p}{\partial x_3^2} \quad (1.27)$$

The initial condition is

$$p(x_3, 0^+) = p_0 \quad (1.28)$$

and the boundary conditions are

$$\begin{aligned} p(0, t) &= 0 \\ \frac{\partial p}{\partial x_3}(L, t) &= 0 \end{aligned} \quad (1.29)$$

The first boundary condition reflects that the platen is porous, while the second one is associated to the infinite permeability of the base.

The solution of equation (1.27), subjected to the conditions (1.28) and (1.29) is

$$p(x_3, t) = 2p_0 \sum_{n=1}^{\infty} \frac{1}{\lambda_n} \sin\left(\lambda_n \frac{x_3}{L}\right) e^{-\lambda_n^2 \frac{C_1}{L^2} t} \quad (1.30)$$

where $\lambda_n = \frac{(2n-1)\pi}{2}$. To evaluate the displacement field, equations (1.25) and (1.21) are combined to obtain

$$(\lambda_{solid} + 2\mu_{solid}) \frac{\partial^2 u_3}{\partial x_3^2} = \alpha \frac{\partial p}{\partial x_3} \quad (1.31)$$

The displacement field is, thus, obtained replacing the time derivative of equation (1.30) in equation (1.31)

$$u_3(x_3, t) = -2p_0 \left(\frac{\alpha}{\lambda_{solid} + 2\mu_{solid}} \right) \sum_{n=1}^{\infty} \frac{1}{\lambda_n^2} \cos\left(\lambda_n \frac{x_3}{L}\right) e^{-\lambda_n^2 \frac{C_1}{L^2} t} + f(t) + g(t) \quad (1.32)$$

To complete the solution, two boundary conditions are necessary. The first condition is $u_3(L, t) = 0$, which implies that $g(t) = -f(t)L$. The second condition outcrops from the stress condition and the equation (1.21):

$$\sigma_{33}(0, t) = \frac{-F}{A} = (\lambda_{solid} + 2\mu_{solid}) \frac{\partial u_3}{\partial x_3}(0, t) - \alpha p(0, t) \quad (1.33)$$

and, so,

$$\frac{\partial u_3}{\partial x_3}(0, t) = \frac{-F}{A(\lambda_{solid} + 2\mu_{solid})} \quad (1.34)$$

This condition determines that $f(t) = \frac{-F}{A(\lambda_{solid} + 2\mu_{solid})}$ and, thus, equation (1.32) can be rewritten as

$$u_3(x_3, t) = \frac{F}{A(\lambda_{solid} + 2\mu_{solid})}(L - x_3) +$$

$$-2p_0 \left(\frac{\alpha}{\lambda_{solid} + 2\mu_{solid}} \right) \sum_{n=1}^{\infty} \frac{1}{\lambda_n^2} \cos\left(\lambda_n \frac{x_3}{L}\right) e^{-\lambda_n^2 \frac{C_1}{L^2} t} \quad (1.35)$$

In the incompressibility hypothesis for both fluid and solid, $\alpha = 1$, $\frac{1}{M} = 0$ and $C_1 = k(\lambda_{solid} + 2\mu_{solid})$. Moreover, the initial stress is transferred immediately through the pore fluid and, as a consequence, $p_0 = \frac{F}{A}$. Under these conditions, the consolidation problem is equivalent to the confined compression of a biphasic material, as highlighted in the following.

CHAPTER II

BIOT'S MODEL EXTENSIONS: STEADY-STATE CASES

2.1 Anisotropic Poroelastic Theory

2.1.1 Introduction

The poroelasticity theory of Biot, first presented in his paper of 1941 for an isotropic porous medium, has been extended to consider also the anisotropy of both the solid matrix and the permeability. Cowin (Cowin, 2007), thus, developed a poroelastic theory extending Biot's statements, combining and modifying the theories for the elastic solids, the viscous fluids and for the fluid flow through porous media. In the following presentation, a slightly unconventional tensor-matrix notation is employed to represent second and fourth rank tensors in 3D as vector and second rank tensors, respectively, in 6D (denoted with the symbol $\widehat{\cdot}$). There are three sets of elastic constants employed in this poroelastic theory, the drained $\widehat{\mathbf{S}}^d$, the undrained, $\widehat{\mathbf{S}}^u$, and those of the matrix material, $\widehat{\mathbf{S}}^m$. The RVE associated with the determination of the first two sets of elastic constants is a bigger one, containing the pores, while for the evaluation of the elastic constants for the matrix material, a smaller RVE is employed, containing no pores. The elastic compliance matrices for these materials have a similar representation:

$$\widehat{\mathbf{S}}^x = \begin{bmatrix} \widehat{S}_{11}^x & \widehat{S}_{12}^x & \widehat{S}_{13}^x & \widehat{S}_{14}^x & \widehat{S}_{15}^x & \widehat{S}_{16}^x \\ \widehat{S}_{12}^x & \widehat{S}_{22}^x & \widehat{S}_{23}^x & \widehat{S}_{24}^x & \widehat{S}_{25}^x & \widehat{S}_{26}^x \\ \widehat{S}_{13}^x & \widehat{S}_{23}^x & \widehat{S}_{33}^x & \widehat{S}_{34}^x & \widehat{S}_{35}^x & \widehat{S}_{36}^x \\ \widehat{S}_{14}^x & \widehat{S}_{24}^x & \widehat{S}_{34}^x & \widehat{S}_{44}^x & \widehat{S}_{45}^x & \widehat{S}_{46}^x \\ \widehat{S}_{15}^x & \widehat{S}_{25}^x & \widehat{S}_{35}^x & \widehat{S}_{45}^x & \widehat{S}_{55}^x & \widehat{S}_{56}^x \\ \widehat{S}_{16}^x & \widehat{S}_{26}^x & \widehat{S}_{36}^x & \widehat{S}_{46}^x & \widehat{S}_{56}^x & \widehat{S}_{66}^x \end{bmatrix} \quad (2.1)$$

Seven scalar stress variables and seven scalar strain variables are involved in poroelasticity. The seven scalar stress variables are the six components of the stress tensor $\hat{\boldsymbol{\sigma}}$ and the pore pressure p . The seven scalar strain variables are the six components of the strain $\hat{\boldsymbol{\varepsilon}}$ and the variation in (dimensionless) fluid content ζ . These variables can be considered as conjugate pairs of stress measure $(\hat{\boldsymbol{\sigma}}, p)$ and strain measures $(\hat{\boldsymbol{\varepsilon}}, \zeta)$, appearing in the following form for the work done on the poroelastic medium, $dW = \boldsymbol{\sigma} : d\boldsymbol{\varepsilon} + pd\zeta$. The poroelastic theory considered here is fully saturated, which means that the volume fraction of fluid is equal to the porosity of the solid matrix.

2.1.2 The stress-strain- pore pressure constitutive relation

The basic hypothesis of the poroelasticity theory is that the average strain $\hat{\boldsymbol{\varepsilon}}$ in the RVE of the saturated porous medium is related both to the average stress $\hat{\boldsymbol{\sigma}}$ in the RVE and to the fluid pressure p in the fluid-filled pores. For this reason, the stress-strain-pore pressure constitutive relation is expressed as follows:

$$\hat{\boldsymbol{\varepsilon}} = \widehat{\mathbf{S}}^d \cdot \hat{\boldsymbol{\sigma}} + \widehat{\mathbf{S}}^d \cdot \hat{\mathbf{A}}p \quad (2.2)$$

while the stress-pore pressure-strain relation is:

$$\hat{\boldsymbol{\sigma}} + \hat{\mathbf{A}}p = \widehat{\mathbf{C}}^d \cdot \hat{\boldsymbol{\varepsilon}} \quad (2.3)$$

where $\widehat{\mathbf{S}}^d$ represents the drained anisotropic compliance elastic constants of the saturated porous medium and $\widehat{\mathbf{C}}^d$ is its reciprocal, the drained anisotropic elasticity tensor. The 6D vector (3D symmetric second rank tensor \mathbf{A}) $\hat{\mathbf{A}}$ is the Biot effective stress coefficient vector (6D) or tensor (3D). The porous elastic material is viewed as a composite of an elastic solid and a pore fluid.

The Biot effective stress coefficient vector $\hat{\mathbf{A}}$ depends on the difference between effective drained elastic constants $\hat{\mathbf{S}}^d$ and the solid matrix material elastic compliance tensor $\hat{\mathbf{S}}^m$, as illustrated in the following relationship:

$$\hat{\mathbf{A}} = (\hat{\mathbf{1}} - \hat{\mathbf{C}}^d \cdot \hat{\mathbf{S}}^m) \cdot \hat{\mathbf{U}} \quad (2.4)$$

where $\hat{\mathbf{U}} = [1,1,1,0,0,0]^T$ is the six dimensional vector representation of the three dimensional unit tensor. The vector $\hat{\mathbf{U}}$ is distinct from the unit tensor in six dimensions, denoted by $\hat{\mathbf{1}}$. The components of $\hat{\mathbf{A}}$ depend on both the matrix and drained elastic constants. Moreover, if the symmetry of $\hat{\mathbf{S}}^m$ is less than transversely isotropic and/or its axis of symmetry is not coincident with the transversely isotropic axis of symmetry of $\hat{\mathbf{C}}^d$, then the 6D vector $\hat{\mathbf{C}}^d \cdot \hat{\mathbf{S}}^m \cdot \hat{\mathbf{U}}$ has, in general, six non zero components and the solution of the problems is quite complicated. If, instead, both $\hat{\mathbf{C}}^d$ and $\hat{\mathbf{S}}^m$ are transversely isotropic respect to a common axis, then

$$\hat{\mathbf{A}} = [A_1, A_1, A_3, 0, 0, 0]^T \quad (2.5)$$

where

$$\begin{aligned} \hat{A}_1 &= 1 - (\hat{C}_{11}^d + \hat{C}_2^d)(\hat{S}_{11}^m + \hat{S}_{12}^m + \hat{S}_{13}^m) - \hat{C}_{13}^d(2\hat{S}_{13}^m + \hat{S}_{33}^m) \\ \hat{A}_3 &= 1 - 2\hat{C}_{13}^d(\hat{S}_{11}^m + \hat{S}_{12}^m + \hat{S}_{13}^m) - \hat{C}_{33}^d(2\hat{S}_{13}^m + \hat{S}_{33}^m) \end{aligned}$$

If $\hat{\mathbf{C}}^d$ and $\hat{\mathbf{S}}^m$ are isotropic, it follows that

$$\hat{\mathbf{A}} = \alpha \hat{\mathbf{U}} \quad \text{where} \quad \alpha = [1 - (K^d / K^m)] \quad (2.6)$$

where α is the isotropic effective stress coefficient. The hypothesis that $\hat{\mathbf{S}}^m$ is isotropic does not mean that the real matrix material is actually isotropic, but rather that there is only a little error in assuming its isotropy because, while the symmetry of the drained elastic

constants, $\widehat{\mathbf{C}}^d$ is strictly associated to the arrangement of pores, the symmetry of the material surrounding the pores, $\widehat{\mathbf{S}}^m$, has only a minor effect. The name of the Biot effective stress coefficient vector $\widehat{\mathbf{A}}$ springs out from its involvement in the definition of the effective stress $\widehat{\boldsymbol{\sigma}}^{eff}$,

$$\widehat{\boldsymbol{\sigma}}^{eff} = \widehat{\boldsymbol{\sigma}} + \widehat{\mathbf{A}}p \quad (2.7)$$

This definition of the effective stress reduces the stress–strain–pressure relation (2.2) to the same form as Hooke’s law, thus

$$\widehat{\boldsymbol{\varepsilon}} = \widehat{\mathbf{S}}^d + \widehat{\boldsymbol{\sigma}}^{eff} \quad (2.8)$$

The effectiveness of the representation (2.8) is associated to the possibility to consider the fluid-saturated porous material as an ordinary elastic material subjected to the ‘‘effective stress’’ $\widehat{\boldsymbol{\sigma}}^{eff}$ rather than to the (ordinary) stress $\widehat{\boldsymbol{\sigma}}$.

Matrix elastic compliance tensor $\widehat{\mathbf{S}}^m$ may be determined using a micromechanical analysis, starting from the knowledge of the drained elastic compliance tensor $\widehat{\mathbf{S}}^d$. For example, in the case of a porous medium, characterized by an isotropic matrix material and dilute and spherical shaped pores, the drained elastic material is isotropic and the bulk and shear moduli, K^d e G^d , are linked to the matrix bulk and shear moduli, K^m e G^m , and Poisson’s ratio ν^m by:

$$K^d = K^m - \frac{\phi K^m}{1 - \frac{K^m}{K^m + \frac{4}{3}G^m}} \quad \frac{G^d}{G^m} = 1 - \frac{15(1-\nu^m)\phi}{7-5\nu^m} \quad (2.9)$$

where ϕ is the porosity associated with the spherical pores.

Once the porosity ϕ and the drained constants K^d and G^d are known, equations (2.9) can be used to evaluate the matrix bulk and shear moduli, K^m and G^m , recalling that for an isotropic material, Poisson's ratio ν^m is related to K^m and G^m by:

$$\nu^m = \frac{(3K^m - 2G^m)}{(6K^m + 2G^m)} \quad (2.10)$$

The Biot effective stress coefficient vector needs some considerations about its derivation, based on the relationship subsisting between the response of the fluid-saturated porous material and that of the drained material by considering the loading

$$\mathbf{t} = \boldsymbol{\sigma} \cdot \mathbf{n} \text{ on } O_o \quad \text{and} \quad \mathbf{t} = -p\mathbf{n} \text{ on } O_p$$

where O_o and O_p represent the outer boundary of the porous medium and the pore boundary, respectively. This loading condition is, then, divided in the superposition of two separate loadings:

$$\mathbf{t} = -p\mathbf{n} \text{ on } O_o \quad \text{and} \quad \mathbf{t} = -p\mathbf{n} \text{ on } O_p \quad (\text{loading } a)$$

and

$$\mathbf{t} = \boldsymbol{\sigma} \cdot \mathbf{n} + p\mathbf{n} \text{ on } O_o \quad \text{and} \quad \mathbf{t} = 0 \text{ on } O_p \quad (\text{loading } b)$$

Loading *a* determines uniform hydrostatic pressure p in the matrix material and, thus, an uniform strain, in the hypothesis of homogeneous porous material. The strain in the porous material and that in the matrix material are, then, the same because uniform straining of the matrix material are associated to the same straining of the pore space.

For this reason, resulting strain $\widehat{\boldsymbol{\varepsilon}}^a$ in the homogeneous matrix material is, then, uniform and it is expressed as

$$\widehat{\boldsymbol{\varepsilon}}^a = -p\widehat{\mathbf{S}}^m \cdot \widehat{\mathbf{U}} \quad (2.11)$$

where the tensor equation $\boldsymbol{\sigma} = -p\mathbf{1}$ in 3D is rearranged in 6D as $\widehat{\boldsymbol{\sigma}} = -p\widehat{\mathbf{U}}$. For the loading condition (b), instead, the pore pressure is zero, and, so, the exterior surface loading ($\mathbf{t} = \boldsymbol{\sigma} \cdot \mathbf{n} + p\mathbf{n}$ on O_0) can be considered as being applied to the drained elastic material. In this condition, resulting strain $\widehat{\boldsymbol{\varepsilon}}^b$ has the form

$$\widehat{\boldsymbol{\varepsilon}}^b = \widehat{\mathbf{S}}^d \cdot (\widehat{\boldsymbol{\sigma}} + p\widehat{\mathbf{U}}) \quad (2.12)$$

The total strain, due to the loading *a* plus *b*, results, thus,

$$\widehat{\boldsymbol{\varepsilon}} = \widehat{\boldsymbol{\varepsilon}}^a + \widehat{\boldsymbol{\varepsilon}}^b = \widehat{\mathbf{S}}^d \cdot \widehat{\boldsymbol{\sigma}} + p(\widehat{\mathbf{S}}^d - \widehat{\mathbf{S}}^m) \cdot \widehat{\mathbf{U}} \quad (2.13)$$

or, rearranging the terms, it follows that

$$\widehat{\boldsymbol{\varepsilon}} = \widehat{\mathbf{S}}^d \cdot (\widehat{\boldsymbol{\sigma}} + \widehat{\mathbf{1}} - \widehat{\mathbf{C}}^d \widehat{\mathbf{S}}^m) \cdot \widehat{\mathbf{U}} p \quad (2.14)$$

From the comparison of equations (2.14) and (2.2), the definition of the Biot effective stress coefficient vector, given by (2.4), outcrops.

2.1.3 The fluid content-stress-pore pressure constitutive relation

The fluid content–stress–pore pressure constitutive relation involves all the basic field variables for poroelasticity, the total stress $\widehat{\boldsymbol{\sigma}}$, the pore pressure p , the strain in the solid

matrix $\hat{\boldsymbol{\varepsilon}}$, and the variation in (dimensionless) fluid content ζ . The variation in fluid content ζ is defined as the variation of the fluid volume per unit volume of the porous material due to diffusive fluid mass transport and, so, it is the difference between the strain of the pore space and the strain of the fluid volume in the pore space. The variation in fluid content, ζ , is linearly related to both stress, $\hat{\boldsymbol{\sigma}}$, and pore pressure, p :

$$\zeta = \hat{\mathbf{A}} \cdot \hat{\mathbf{S}}^d \cdot \hat{\boldsymbol{\sigma}} + C_{eff}^d p \quad \text{where} \quad C_{eff}^d = \frac{1}{K_{Reff}^d} - \frac{1}{K_{Reff}^m} + \phi \left(\frac{1}{K^f} - \frac{1}{K_{Reff}^m} \right) \quad (2.15)$$

or related, using the relationship (2.3), to both strain $\hat{\boldsymbol{\varepsilon}}$ and pressure p by :

$$\zeta = \hat{\mathbf{A}} \cdot \hat{\boldsymbol{\varepsilon}} + \Lambda p \quad \text{where} \quad \Lambda = C_{eff}^d - \hat{\mathbf{A}} \cdot \hat{\mathbf{S}}^d \cdot \hat{\mathbf{A}} \quad (2.16)$$

The super and subscripted K 's appearing in the previous equations are the different bulk moduli. To define the other bulk moduli of equation (2.15), it has to be noticed that, in the hypothesis of isotropy,

$$\hat{\mathbf{U}} \cdot \hat{\mathbf{S}} \cdot \hat{\mathbf{U}} = \frac{3(1-2\nu)}{E} = \frac{1}{K} \quad (2.17)$$

Moreover, the Reuss effective bulk modulus is the lower bound of the effective bulk modulus for an anisotropic material, while the Voigt effective bulk modulus is the upper bound, i. e.

$$(\hat{\mathbf{U}} \cdot \hat{\mathbf{S}} \cdot \hat{\mathbf{U}})^{-1} = K_{Reff} \leq K_{eff} \leq K_{Veff} = (\hat{\mathbf{U}} \cdot \hat{\mathbf{S}}^{-1} \cdot \hat{\mathbf{U}}) / 9$$

In the hypothesis of isotropy, the two bounds coincide with the isotropic bulk modulus, K , and, thus,

$$\frac{1}{K_{Reff}} = \frac{1}{K_R} = \frac{1}{K_{eff}} = \frac{1}{K_{Veff}} = \frac{1}{K_V} = (\widehat{\mathbf{U}} \cdot \widehat{\mathbf{S}} \cdot \widehat{\mathbf{U}})^{-1} = \frac{(\widehat{\mathbf{U}} \cdot \widehat{\mathbf{S}}^{-1} \cdot \widehat{\mathbf{U}})}{9} = \frac{3(1-2\nu)}{E} = \frac{1}{K}$$

where E is the Young's modulus and ν is the Poisson's ratio and the subscript eff disappears because, in this case, the bulk moduli are the actual ones. In the poroelasticity theory, $\widehat{\mathbf{U}} \cdot \widehat{\mathbf{S}} \cdot \widehat{\mathbf{U}}$ is defined as the inverse of the effective bulk modulus when the material is not isotropic. Thus, for orthotropic drained and matrix elastic compliance tensor, $\widehat{\mathbf{S}}^d$ and $\widehat{\mathbf{S}}^m$, respectively, it is possible to introduce the following definitions, employed in (2.15),

$$\frac{1}{K_{eff}^d} = \widehat{\mathbf{U}} \cdot \widehat{\mathbf{S}}^d \cdot \widehat{\mathbf{U}} = \frac{1}{E_1^d} + \frac{1}{E_2^d} + \frac{1}{E_3^d} - \frac{2\nu_{23}^d}{E_2^d} - \frac{2\nu_{31}^d}{E_3^d} - \frac{2\nu_{12}^d}{E_1^d} \quad (2.18)$$

$$\frac{1}{K_{eff}^m} = \widehat{\mathbf{U}} \cdot \widehat{\mathbf{S}}^m \cdot \widehat{\mathbf{U}} = \frac{1}{E_1^m} + \frac{1}{E_2^m} + \frac{1}{E_3^m} - \frac{2\nu_{23}^m}{E_2^m} - \frac{2\nu_{31}^m}{E_3^m} - \frac{2\nu_{12}^m}{E_1^m} \quad (2.19)$$

These equations allow to rewrite Λ , (2.16), as function of the effective bulk moduli. From equation (2.4), (2.17) and (2.18),

$$\widehat{\mathbf{A}} \cdot \widehat{\mathbf{S}}^d \cdot \widehat{\mathbf{A}} = \frac{1}{K_{Reff}^d} - \frac{1}{K_{Reff}^m} + \widehat{\mathbf{U}} \cdot \widehat{\mathbf{S}}^m \cdot \widehat{\mathbf{C}}^d \cdot \widehat{\mathbf{S}}^m \cdot \widehat{\mathbf{U}} \quad (2.20)$$

Substituting this result into (2.16) and employing (2.15) to remove C_{eff}^d , it follows that:

$$\Lambda = \phi \left(\frac{1}{K^f} - \frac{1}{K_{Reff}^m} \right) - \widehat{\mathbf{U}} \cdot \widehat{\mathbf{S}}^m \cdot \widehat{\mathbf{C}}^d \cdot \widehat{\mathbf{S}}^m \cdot \widehat{\mathbf{U}} \quad (2.21)$$

2.1.4 Darcy's Law

The other constitutive relation of poroelasticity is Darcy's law, relating the fluid mass flow rate, $\rho_f \mathbf{v}$, to the gradient (∇p) of the pore pressure p

$$\rho_f \mathbf{v} = -\mathbf{H}(p)\nabla p(\mathbf{x}, t), \mathbf{H}(p) = \mathbf{H}^T(p) \quad (2.22)$$

The tensor \mathbf{H} does not depend on the pore pressure and it may be represented by $\mathbf{H} = \frac{\rho_{f0} \mathbf{K}_p}{\phi \mu}$ where \mathbf{K}_p is the intrinsic Darcy's law permeability tensor, ρ_{f0} is a reference value of the fluid density and μ is the fluid viscosity. The intrinsic anisotropic permeability tensor \mathbf{K}_p has units of length squared and it depends exclusively on the porous structure and not on the fluid in the pores; thus Darcy's law takes the form

$$\mathbf{q} = (\phi \rho_f / \rho_{f0}) \mathbf{v} = -(\mathbf{K}_p / \mu) \nabla p(\mathbf{x}, t), \mathbf{K}_p = (\mathbf{K}_p)^T \quad (2.23)$$

It has been shown that the symmetry in \mathbf{K}_p holds for material symmetries greater than monoclinic and the volume flux \mathbf{q} has the same dimension of a velocity because it represents the volume flow rate per unit area. In the case of isotropic permeability, Darcy's Law is written in the form

$$\mathbf{q} = (\phi \rho_f / \rho_{f0}) \mathbf{v} = -k \nabla p(\mathbf{x}, t) \quad (2.24)$$

where $k = \frac{\kappa}{\mu}$ is the hydraulic conductivity and κ indicates the constant value of permeability in the hypothesis of isotropy.

2.1.5 The matrix material and pore fluid incompressibility constraints for poroelasticity

In the poroelasticity theory, the incompressibility constituent specific constraints concern both the matrix material or the pore fluid. These two incompressibility constraints require

that both materials experience no volume change at any stress level. These constraints introduce an indeterminate pressure in both the fluid and in the matrix material, that must be equal at any location in both materials from the requirement of local force equilibrium. The two assumptions are, thus, compatible. The incompressibility constraint for the fluid implies that the reciprocal of the bulk modulus of the fluid tend to zero as the instantaneous density tends to the initial density,

$$\lim_{\rho_f \rightarrow \rho_{f0}} \frac{1}{K^f} \rightarrow 0 \quad (2.25)$$

or that the fluid density ρ_f is constant; thus, ρ_f and its initial value ρ_{f0} are equal. Under these assumptions, Darcy's law (2.23) becomes

$$\mathbf{q} = \phi \mathbf{v} = -(1/\mu) \mathbf{K}_p \nabla p(x, t), \mathbf{K}_p = (\mathbf{K}_p)^T \quad (2.26)$$

The incompressibility constraint for the matrix material requires, instead, that the dilatational strain

$$\widehat{\mathbf{U}} \cdot \widehat{\boldsymbol{\epsilon}}^m = \text{tr} \boldsymbol{\epsilon}^m = \boldsymbol{\epsilon}_{kk}^m = \widehat{\mathbf{U}} \cdot \widehat{\mathbf{S}}^m \cdot \widehat{\boldsymbol{\sigma}}^m = \widehat{\boldsymbol{\sigma}}^m \cdot \widehat{\mathbf{S}}^m \cdot \widehat{\mathbf{U}} \quad (2.27)$$

vanishes for all possible stress states $\widehat{\boldsymbol{\sigma}}^m$; thus

$$\widehat{\mathbf{U}} \cdot \widehat{\boldsymbol{\epsilon}}^m = 0 \Rightarrow \widehat{\mathbf{U}} \cdot \widehat{\mathbf{S}}^m = \widehat{\mathbf{S}}^m \cdot \widehat{\mathbf{U}} = 0 \quad (2.28)$$

The components of the vector $\widehat{\mathbf{U}} \cdot \widehat{\mathbf{S}}^m = \widehat{\mathbf{S}}^m \cdot \widehat{\mathbf{U}}$ are given by

$$\widehat{\mathbf{U}} \cdot \widehat{\mathbf{S}}^m = \frac{1}{3} \left[\frac{1}{K_1^m}, \frac{1}{K_2^m}, \frac{1}{K_3^m}, \frac{1}{K_4^m}, \frac{1}{K_5^m}, \frac{1}{K_6^m} \right] \quad (2.29)$$

where:

$$\frac{1}{K_\alpha^m} = S_{\alpha 1}^m + S_{\alpha 2}^m + S_{\alpha 3}^m \quad \text{with } \alpha = (1, \dots, 6) \quad (2.30)$$

in the more general case of no (triclinic) symmetry, while in the cases of orthotropic, transversely isotropic and isotropic symmetries, respectively

$$\begin{aligned}
 \widehat{\mathbf{U}} \cdot \widehat{\mathbf{S}}^m &= \frac{1}{3} \left[\frac{1}{K_1^m}, \frac{1}{K_2^m}, \frac{1}{K_3^m}, 0, 0, 0 \right], \frac{1}{3K_1^m} = \frac{1 - \nu_{12}^m - \nu_{13}^m}{E_1^m} \\
 \frac{1}{3K_2^m} &= \frac{1 - \nu_{21}^m - \nu_{23}^m}{E_2^m}, \frac{1}{3K_3^m} = \frac{1 - \nu_{13}^m - \nu_{32}^m}{E_3^m} \\
 \widehat{\mathbf{U}} \cdot \widehat{\mathbf{S}}^m &= \frac{1}{3} \left[\frac{1}{K_1^m}, \frac{1}{K_2^m}, \frac{1}{K_3^m}, 0, 0, 0 \right], \frac{1}{3K_3^m} = \frac{1 - 2\nu_{31}^m}{E_3^m} \\
 \frac{1}{3K_1^m} &= \frac{1}{3K_2^m} = \frac{1 - \nu_{12}^m - \nu_{13}^m}{E_1^m} = \frac{1 - \nu_{21}^m - \nu_{23}^m}{E_2^m}, \\
 \widehat{\mathbf{U}} \cdot \widehat{\mathbf{S}}^m &= \frac{1}{3} [1, 1, 1, 0, 0, 0], \frac{1}{3K^m} = \frac{1 - 2\nu^m}{E^m}
 \end{aligned} \tag{2.31}$$

The incompressibility condition $\widehat{\mathbf{U}} \cdot \widehat{\mathbf{S}}^m = \widehat{\mathbf{S}}^m \cdot \widehat{\mathbf{U}} = 0$, as shown in (2.29), implies that $\widehat{\mathbf{S}}^m$ may be singular, i.e. $\det \widehat{\mathbf{S}}^m = 0$.

From (2.28) and (2.31), the incompressibility condition $\widehat{\mathbf{U}} \cdot \widehat{\mathbf{S}}^m = \widehat{\mathbf{S}}^m \cdot \widehat{\mathbf{U}} = 0$ is expressed in terms of Poisson's ratios for the orthotropic, transversely isotropic and isotropic symmetries by

$$\begin{aligned}
 \nu_{12}^m &= \frac{1}{2} \left(1 + \frac{E_1^m}{E_2^m} - \frac{E_1^m}{E_3^m} \right), \nu_{13}^m = \frac{1}{2} \left(1 + \frac{E_1^m}{E_3^m} - \frac{E_1^m}{E_2^m} \right), \nu_{23}^m = \frac{1}{2} \left(1 + \frac{E_2^m}{E_3^m} - \frac{E_2^m}{E_1^m} \right) \\
 \nu_{12}^m &= 1 - \frac{E_1^m}{2E_3^m}, \nu_{13}^m = \frac{E_1^m}{2E_3^m}, \nu_{31}^m = \frac{1}{2} \quad \text{and} \quad \nu^m = \frac{1}{2}
 \end{aligned} \tag{2.32}$$

The two incompressibility constraints influence all the constitutive equations except the Darcy's law, which is unchanged because, in both the analyzed cases, it is based on the assumption that the movement of the boundaries of the pores is a negligible higher order term. For this reason, the law has the same form in the compressible and incompressible cases as for a rigid porous material.

The stress-strain-pore pressure relation for the incompressible case becomes

$$\hat{\boldsymbol{\varepsilon}} = \hat{\mathbf{S}}^d \cdot (\hat{\boldsymbol{\sigma}} + \hat{\mathbf{U}}p) \quad (2.33)$$

for $\hat{\mathbf{U}} \cdot \hat{\mathbf{S}}^m = 0$ since the Biot effective stress coefficient tensor $\hat{\mathbf{A}}$, under these conditions, becomes

$$\hat{\mathbf{A}} = \hat{\mathbf{U}} \quad (2.34)$$

The definition of the effective stress $\hat{\boldsymbol{\sigma}}^{eff}$ changes in

$$\hat{\boldsymbol{\sigma}}^{eff} = (\hat{\boldsymbol{\sigma}} + \hat{\mathbf{U}}p) \quad (2.35)$$

Since the reciprocal of K_{Reff}^m and K^f are zero in the incompressible case, the fluid content–stress–pore pressure relation becomes

$$\zeta = \hat{\mathbf{U}} \cdot \hat{\mathbf{S}}^d \cdot \hat{\boldsymbol{\sigma}} + \frac{p}{K_{Reff}^d} \quad \text{where} \quad C_{eff}^d = \frac{1}{K_{Reff}^d} = \hat{\mathbf{U}} \cdot \hat{\mathbf{S}}^d \cdot \hat{\mathbf{U}} \quad (2.36)$$

while the fluid content-strain-pore pressure constitutive relation assumes the form

$$\zeta = \hat{\mathbf{U}} \cdot \hat{\boldsymbol{\varepsilon}} \quad \text{and} \quad \Lambda = 0 \quad (2.37)$$

Also equation (2.19) is modified in the case of incompressibility

$$\frac{1}{K_{Reff}^m} = \hat{\mathbf{U}}^T \cdot \hat{\mathbf{S}}^m \cdot \hat{\mathbf{U}} = 0 \quad (2.38)$$

for $\hat{\mathbf{U}} \cdot \hat{\mathbf{S}}^m = 0$.

The pore pressure evaluated from equation (2.16) is given by

$$p = \frac{1}{\Lambda} [\zeta - (\hat{\mathbf{A}} \cdot \hat{\boldsymbol{\epsilon}})] \quad (2.39)$$

For incompressibility

$$\Lambda \rightarrow 0 \quad \text{and} \quad [\zeta - (\hat{\mathbf{A}} \cdot \hat{\boldsymbol{\epsilon}})] \rightarrow 0 \quad (2.40)$$

and, thus, the pressure p given by the equation (2.39) results indeterminate as the porous medium constituents become incompressible. To apply equation (2.35), is, then, necessary to introduce a Lagrange multiplier. Moreover, there are two very different meanings associated with the symbol for pore pressure p . In the compressible case, p is a thermodynamic variable, evaluated through an equation of state, containing the temperature and the specific volume of the fluid as independent variables. In the incompressible case, instead, p is a Lagrange multiplier whose value is determined through the boundary conditions and it is, thus, independent of the temperature and the specific volume of the fluid.

2.1.6 The undrained elastic coefficients

In the undrained case, no fluid movement in the poroelastic medium is possible and, thus, the variation in fluid content, ζ , is zero. In this case, equation (2.15) may be solved for p and, so, the pore pressure is related to the solid stress $\hat{\boldsymbol{\sigma}}$ by $p = -\hat{\mathbf{B}} \cdot \hat{\boldsymbol{\sigma}}$, where

$$\hat{\mathbf{B}} = \frac{1}{C_{\text{eff}}^d} \hat{\mathbf{S}}^d \cdot \hat{\mathbf{A}} = \frac{1}{C_{\text{eff}}^d} (\hat{\mathbf{S}}^d - \hat{\mathbf{S}}^m) \cdot \hat{\mathbf{U}} \quad (2.41)$$

$\hat{\mathbf{B}}$ is the *Skempton compliance difference tensor*. In the incompressible case, employing the equations (2.41), (2.36) and (2.28), the *Skempton compliance difference tensor* becomes

$$\hat{\mathbf{B}} = K_{\text{Reff}}^d \hat{\mathbf{S}}^d \cdot \hat{\mathbf{U}} \quad (2.42)$$

Using equation (2.18), it follows that

$$\widehat{\mathbf{U}} \cdot \widehat{\mathbf{B}} = K_{\text{Reff}}^d \widehat{\mathbf{U}} \cdot \widehat{\mathbf{S}}^d \cdot \widehat{\mathbf{U}} = \mathbf{1} \quad (2.43)$$

In the isotropic compressible case, the *Skempton compliance difference tensor* results

$$\widehat{\mathbf{B}} = \frac{S}{3} \widehat{\mathbf{U}} \quad \text{or} \quad \widehat{B}_1 = \widehat{B}_2 = \widehat{B}_3 = \frac{S}{3}, \widehat{B}_4 = \widehat{B}_5 = \widehat{B}_6 = 0 \quad (2.44)$$

where S is the *Skempton parameter*:

$$S = \frac{\alpha}{C^d K^d} \quad (2.45)$$

Also in this case, the bulk moduli are the actual ones. Moreover, as $p = -\widehat{\mathbf{B}} \cdot \widehat{\boldsymbol{\sigma}}$, in the hypothesis of isotropic and compressible medium, $p = -\frac{S}{3} \widehat{\mathbf{U}} \cdot \widehat{\boldsymbol{\sigma}} = -\frac{S}{3} \text{tr} \widehat{\boldsymbol{\sigma}}$. If, instead, $K^f = K^m$, then $C^d = \frac{\alpha}{K^d}$ and $S = 1$ for both the compressible and incompressible cases.

In the isotropic incompressible case, $S = 1$ and, so, $p = -\frac{1}{3} \widehat{\mathbf{U}} \cdot \widehat{\boldsymbol{\sigma}} = -\frac{1}{3} \text{tr} \widehat{\boldsymbol{\sigma}}$, $K^d = \frac{1}{C^d}$ and $\widehat{\mathbf{A}} = \widehat{\mathbf{U}}$. In the hypothesis of compressibility, the undrained elastic coefficients $\widehat{\mathbf{S}}^u$ are linked to the drained elastic constants $\widehat{\mathbf{S}}^d$ and the tensor $\widehat{\mathbf{A}}$ by

$$\widehat{\mathbf{S}}^u = \widehat{\mathbf{S}}^d - \widehat{\mathbf{S}}^d \cdot \widehat{\mathbf{A}} \otimes \widehat{\mathbf{B}} = \widehat{\mathbf{S}}^d - \frac{1}{C_{\text{eff}}^d} (\widehat{\mathbf{S}}^d \cdot \widehat{\mathbf{A}} \otimes \widehat{\mathbf{S}}^d \cdot \widehat{\mathbf{A}}) \quad (2.46)$$

In the incompressible case, instead, the undrained elastic coefficients $\widehat{\mathbf{S}}^u$ are related to the drained elastic constants $\widehat{\mathbf{S}}^d$ by

$$\widehat{\mathbf{S}}^u = \widehat{\mathbf{S}}^d - K_{\text{Reff}}^d (\widehat{\mathbf{U}} \cdot \widehat{\mathbf{S}}^d \otimes \widehat{\mathbf{S}}^d \cdot \widehat{\mathbf{U}}) \quad (2.47)$$

as a consequence of equation (2.45) with the application of (2.36) and (2.37).

When equation (2.47) is dotted with $\widehat{\mathbf{U}}$ and the (2.37) employed again, the undrained elastic coefficients are also incompressible in the case of assumed incompressibility of the matrix material and the fluid,

$$\widehat{\mathbf{U}} \cdot \widehat{\mathbf{S}}^u = \widehat{\mathbf{U}} \cdot \widehat{\mathbf{S}}^d - K_{\text{Ref}}^d (\widehat{\mathbf{U}} \cdot \widehat{\mathbf{S}}^d \cdot \widehat{\mathbf{U}} \otimes \widehat{\mathbf{S}}^d \cdot \widehat{\mathbf{U}}) = \widehat{\mathbf{U}} \cdot \widehat{\mathbf{S}}^d - \widehat{\mathbf{S}}^d \cdot \widehat{\mathbf{U}} = 0 \quad (2.48)$$

In the isotropic compressible case, equation (2.45) reduces to formulas for the undrained bulk modulus K^u ($K^u = (\widehat{\mathbf{U}}^T \cdot \widehat{\mathbf{S}}^u \cdot \widehat{\mathbf{U}})^{-1}$) and the undrained Poisson's ratio ν^u in terms of K^f , ν^f , K^d , K^m and ϕ . Thus

$$K^u = K^d + \frac{K^f (1 - \frac{K^d}{K^m})^2}{\frac{K^f}{K^m} (1 - \frac{K^d}{K^m} - \phi) + \phi} \quad \text{and} \quad \nu^u = \frac{3\nu^d + S(1 - 2\nu^d)(1 - \frac{K^d}{K^m})}{3 - S(1 - 2\nu^d)(1 - \frac{K^d}{K^m})} \quad (2.49)$$

In the isotropic incompressible case, the relationships (2.49) reduce to $\frac{1}{K^u} = 0$ and $\nu^u = \frac{1}{2}$, consistent with the general result for incompressibility for the undrained constant set. As a consequence, $E^u = 3G$.

2.1.7 Expression of mass and momentum conservation

The conservation of mass is expressed, in general, by the continuity equation,

$$\frac{\partial \rho}{\partial t} + \nabla \cdot (\rho \mathbf{v}) = 0 \quad (2.50)$$

The form of the mass conservation equation (2.50) is modified by first replacing ρ by $\phi \rho_f$ and, then, dividing the equation by ρ_{f0} ; thus

$$\frac{1}{\rho_{f0}} \frac{\partial \phi \rho_f}{\partial t} + \frac{1}{\rho_{f0}} \nabla \cdot (\phi \rho_f \mathbf{v}) = 0 \quad (2.51)$$

Replacing equation (2.23) in equation (2.51) and setting $\frac{\partial \zeta}{\partial t} = \frac{1}{\rho_{f0}} \frac{\partial \phi \rho_f}{\partial t}$, the equation of continuity becomes

$$\frac{\partial \zeta}{\partial t} + \nabla \cdot \mathbf{q} = 0 \quad (2.52)$$

In the case of incompressibility, $\rho_f = \rho_{f0}$ and equation (2.51) can be rewritten as

$$\frac{\partial \phi}{\partial t} + \nabla \cdot (\phi \mathbf{v}) = 0 \quad (2.53)$$

The stress equations of motion in 3D,

$$\rho \ddot{\mathbf{u}} = \nabla \cdot \boldsymbol{\sigma} + \rho \mathbf{b}, \quad \boldsymbol{\sigma} = \boldsymbol{\sigma}^T \quad (2.54)$$

are written in the conventional notation because they have no simple representation in the 6D vector notation; $\ddot{\mathbf{u}}$ represents the accelerations and \mathbf{b} the body forces.

2.1.8 The basic equations of poroelasticity

Resuming what just said before, the poroelasticity theory presented here is described by a system of 18 equations in eighteen scalar unknowns. The 18 scalar unknowns are the six components of the stress tensor $\boldsymbol{\sigma}$, the fluid pressure p , the fluid density ρ_f , the variation in fluid content ζ , the six components of the strain tensor $\boldsymbol{\varepsilon}$ and the three components of the displacement vector \mathbf{u} . The 18 scalar equations of the theory of poroelastic solids are the six equations of the strain–stress–pressure relation, (2.2), the six strain displacement relations, $2\boldsymbol{\varepsilon} = ((\nabla \otimes \mathbf{u})^T + \nabla \otimes \mathbf{u})$, the three equations of motion, (2.54), the one fluid content–stress–pressure relation (or the one fluid content–strain–pressure relation), (2.15), the mass conservation equation, (2.52), and a relation between the fluid pressure and the

density $p = p(\rho)$, not specified here. The parameters of a poroelasticity problem are the Biot effective stress coefficients $\widehat{\mathbf{A}}$, the drained effective elastic constants of porous matrix material $\widehat{\mathbf{S}}$, C_{eff}^d , the fluid viscosity μ , the intrinsic permeability tensor \mathbf{K}_p , and the body force \mathbf{d} , which are all assumed to be known. If the displacement vector \mathbf{u} is the independent variable, no further equations are necessary. If, instead, the displacement vector is a dependent variable, use of the compatibility equations is necessary to ensure that the displacements are consistent. There are many methods to solve poroelastic problems for compressible media. The choice of the solution method is strictly associated to the known information and the fields that are to be calculated. One possible approach consists in solving for the variation in fluid content ζ if the stress or the strain field is known or may be calculated without reference to the variation in fluid content ζ . To obtain the diffusion equation for the variation in fluid content, the Darcy's law, (2.23), is first substituted into the expression (2.52) for the conservation of mass and, subsequently, the pore pressure is eliminated using equation (2.39), thus

$$\frac{\partial \zeta}{\partial t} - \frac{1}{\mu \Lambda} \widehat{\mathbf{K}}_p \cdot \widehat{\mathbf{O}} \zeta = - \frac{1}{\mu \Lambda} \widehat{\mathbf{K}}_p \cdot \widehat{\mathbf{O}} [\widehat{\mathbf{A}} \cdot \widehat{\boldsymbol{\varepsilon}}] \quad (2.55)$$

Equation (2.55) shows that the time rate of change of the fluid content ζ is due either to fluid flux or to volume changes caused by the strain field. It is possible to rewrite the right hand side of equation (2.55) in terms of stress, obtaining

$$\frac{\partial \zeta}{\partial t} - \frac{1}{\mu C_{eff}^d} \widehat{\mathbf{K}}_p \cdot \widehat{\mathbf{O}} \zeta = - \frac{1}{\mu C_{eff}^d} \widehat{\mathbf{K}}_p \cdot \widehat{\mathbf{O}} [\widehat{\mathbf{A}} \cdot \widehat{\mathbf{S}}^d \cdot \widehat{\boldsymbol{\sigma}}] \quad (2.56)$$

Also the diffusion equations for the pressure field are employed in the solution of poroelastic problems. The first diffusion equation for the pore pressure field is obtained starting from the substitution of the Darcy's law, (2.23), into the expression (2.52) for the conservation of mass and, subsequently, eliminating the variation in fluid content ζ using the equation (2.15), thus

$$\frac{\partial p}{\partial t} - \frac{1}{\mu \Lambda} \widehat{\mathbf{K}}_p \cdot \widehat{\mathbf{O}} p = - \frac{1}{\Lambda} \widehat{\mathbf{A}} \cdot \frac{\partial \widehat{\boldsymbol{\varepsilon}}}{\partial t} \quad (2.57)$$

The alternative form for the diffusion equation for the pore pressure field is obtained rewriting the right hand side of equation (2.57) in terms of stress, thus

$$\frac{\partial p}{\partial t} - \frac{1}{\mu C_{eff}^d} \widehat{\mathbf{K}}_P \cdot \widehat{\mathbf{O}}p = -\frac{1}{C_{eff}^d} (\widehat{\mathbf{U}} \cdot (\widehat{\mathbf{S}}^m - \widehat{\mathbf{S}}^d) \cdot \frac{\partial \widehat{\mathbf{g}}}{\partial t}) \quad (2.58)$$

For an orthotropic material, equation (2.58) assumes the form:

$$\begin{aligned} C_{eff} \frac{\partial p}{\partial t} - \frac{1}{\mu} K^P_{11} \frac{\partial^2 p}{\partial x_1^2} - \frac{1}{\mu} K^P_{22} \frac{\partial^2 p}{\partial x_2^2} - K^P_{33} \frac{\partial^2 p}{\partial x_3^2} = & -\left\{ \left(\frac{1}{E_1^d} - \frac{\nu_{12}^d}{E_1^d} - \frac{\nu_{31}^d}{E_3^d} - \frac{1}{E_1^m} - \frac{\nu_{12}^m}{E_1^m} - \frac{\nu_{23}^m}{E_3^m} \right) \frac{\partial \sigma_{11}}{\partial t} + \right. \\ & \left. + \left(\frac{1}{E_2^d} - \frac{\nu_{12}^d}{E_1^d} - \frac{\nu_{32}^d}{E_2^d} - \frac{1}{E_2^m} - \frac{\nu_{12}^m}{E_1^m} - \frac{\nu_{23}^m}{E_2^m} \right) \frac{\partial \sigma_{22}}{\partial t} + \left(\frac{1}{E_3^d} - \frac{\nu_{23}^d}{E_2^d} - \frac{\nu_{31}^d}{E_3^d} - \frac{1}{E_3^m} - \frac{\nu_{23}^m}{E_2^m} - \frac{\nu_{31}^m}{E_3^m} \right) \frac{\partial \sigma_{33}}{\partial t} \right\} \end{aligned} \quad (2.59)$$

The boundary conditions on the pore pressure field usually employed in the solution of this differential equation are:

- (i) the specification of the external pore pressure p at the boundary (a lower pressure permits flow across the boundary),
- (ii) the specification of the pressure gradient ∇p at the boundary (a zero pressure gradient permits no flow across the boundary),
- (iii) the specification of some linear combination of (i) and (ii).

2.1.9 The basic equation of incompressible poroelasticity

The compressible poroelasticity as a system of 18 equations in 18 scalar unknowns presented in the previous section may be specialized to the case of incompressibility, obtaining a system of seventeen equations in seventeen scalar unknowns because the fluid density is a constant, $\rho_f = \rho_{f0}$, and no more an unknown of the problem and, so, the equation relating the fluid pressure to the fluid density $p = p(\rho)$ is not considered. The other seventeen equations in seventeen scalar unknowns are determined employing the relationships previously introduced in the hypothesis of incompressibility.

Under these conditions, diffusion equation (2.58) becomes

$$\frac{\partial p}{\partial t} - \frac{K_{Reff}^d}{\mu} \widehat{\mathbf{K}} \cdot \widehat{\mathbf{O}} p = -K_{Reff}^d (\widehat{\mathbf{U}} \cdot \widehat{\mathbf{S}}^d \cdot \frac{\partial \widehat{\mathbf{G}}}{\partial t}) \quad (2.60)$$

For an orthotropic material, equation (2.60) reduces to:

$$\begin{aligned} \frac{1}{K_{Reff}^d} \frac{\partial p}{\partial t} - \frac{1}{\mu} K^P_{11} \frac{\partial^2 p}{\partial x_1^2} - \frac{1}{\mu} K^P_{22} \frac{\partial^2 p}{\partial x_2^2} - K^P_{33} \frac{\partial^2 p}{\partial x_3^2} = -\left\{ \left(\frac{1}{E_1^d} - \frac{\nu_{12}^d}{E_1^d} - \frac{\nu_{31}^d}{E_3^d} - \frac{1}{E_1^m} + \right. \right. \\ \left. \left. - \frac{\nu_{12}^m}{E_1^m} - \frac{\nu_{23}^m}{E_3^m} \right) \frac{\partial \sigma_{11}}{\partial t} + \left(\frac{1}{E_2^d} - \frac{\nu_{12}^d}{E_1^d} - \frac{\nu_{32}^d}{E_2^d} - \frac{1}{E_2^m} - \frac{\nu_{12}^m}{E_1^m} - \frac{\nu_{23}^m}{E_2^m} \right) \frac{\partial \sigma_{22}}{\partial t} + \right. \\ \left. + \left(\frac{1}{E_3^d} - \frac{\nu_{23}^d}{E_2^d} - \frac{\nu_{31}^d}{E_3^d} - \frac{1}{E_3^m} - \frac{\nu_{23}^m}{E_2^m} - \frac{\nu_{31}^m}{E_3^m} \right) \frac{\partial \sigma_{33}}{\partial t} \right\} \end{aligned} \quad (2.61)$$

The boundary conditions on the pore pressure field are the same considered for the compressible case. It is important to note that only the algebraic coefficients of the different terms are changed by the transition to incompressible components; the order and type of derivatives occurring in the differential equations are unchanged.

2.1.10 Compressible and incompressible constituents in anisotropic poroelasticity: The problem of unconfined compression of a disk

Cowin and Mehrabadi (Cowin and Mehrabadi, 2007) employed the equations of anisotropic poroelasticity to found the solution for the problem of unconfined compression of a disk to illustrate the effects of compressibility vs. incompressibility and transverse isotropy vs. isotropy. In the unconfined compression test, a thin cylinder is compressed between two parallel rigid and impermeable smooth plates. The specimen is assumed to have no frictional contact with the end plates so that it is free to expand radially; thus, there are no end effects. The fluid can pass freely across the lateral boundaries (the curved surfaces of the thin cylinder) while the passage is not permitted across the boundaries forming the flat end plates of the thin cylinder for the presence of two parallel rigid and impermeable smooth plates that are squeezing the thin cylinder. Both creep and stress-relaxation tests can be performed. This test is very useful to analyze biomechanics of

cartilaginous tissues, as illustrated in the papers of Cohen et al. (Cohen et al., 1998), who found the solution for the unconfined compression test of a thin cylinder of an incompressible material, in the hypothesis of transversely isotropic incompressible material. Cowin and Mehrabadi (Cowin and Mehrabadi, 2007) determined the solution for the transversely isotropic compressible material, also specializing it to these earlier solutions. The results presented may be used to model also other biological tissues such as osteons.

To solve the problem, cylindrical coordinates are employed and the displacement field components, the pressure and the variation in fluid content are assumed to have the following functional dependencies:

$$u_r = u(r, t), u_z = z\varepsilon(t), p = p(r, t), \zeta = \zeta(r, t) \quad (2.62)$$

$\hat{\boldsymbol{\varepsilon}}$ can be expressed in terms of $u(r, t)$ and $\varepsilon(t)$:

$$\hat{\boldsymbol{\varepsilon}} = \left[\frac{\partial u}{\partial r}, \frac{u}{r}, \varepsilon(t), 0, 0, 0 \right]^T \quad (2.63)$$

Since the shear strains are zero, also the shear stresses are zero; thus, the vector representing stress is:

$$\hat{\boldsymbol{\sigma}} = [\sigma_{rr}, \sigma_{\theta\theta}, \sigma_{zz}, 0, 0, 0]^T \quad (2.64)$$

In this problem, $\widehat{\mathbf{C}}^d$ and $\widehat{\mathbf{S}}^m$ are supposed to be transversely isotropic respect to a common axis and, so,

$$\widehat{\mathbf{C}}^d = \begin{bmatrix} \widehat{C}_{rr}^d & \widehat{C}_{r\theta}^d & \widehat{C}_{rz}^d & 0 & 0 & 0 \\ \widehat{C}_{r\theta}^d & \widehat{C}_{rr}^d & \widehat{C}_{rz}^d & 0 & 0 & 0 \\ \widehat{C}_{rz}^d & \widehat{C}_{rz}^d & \widehat{C}_{zz}^d & 0 & 0 & 0 \\ 0 & 0 & 0 & \widehat{C}_{44}^d & 0 & 0 \\ 0 & 0 & 0 & 0 & \widehat{C}_{44}^d & 0 \\ 0 & 0 & 0 & 0 & 0 & \widehat{C}_{66}^d \end{bmatrix} \quad (2.65)$$

where

$$\begin{aligned} \widehat{C}_{rr}^d &= \frac{\Delta_2}{\Delta_1} E_1^d, \quad \widehat{C}_{r\theta}^d = \frac{1-\Delta_2}{\Delta_1} E_1^d, \quad \widehat{C}_{rz}^d = \frac{\nu_{31}^d}{\Delta_1} E_1^d = \frac{\nu_{13}^d}{\Delta_1} E_3^d, \quad \widehat{C}_{zz}^d = \frac{1-\nu_{12}^d}{\Delta_1} E_3^d \\ \Delta_1 &= 1-\nu_{12}^d - 2\nu_{31}^d\nu_{13}^d, \quad \Delta_2 = \frac{1-\nu_{31}^d\nu_{13}^d}{1+\nu_{12}^d}, \quad \Delta_3 = \frac{(1-2\nu_{31}^d)\Delta_2}{\Delta_1} \end{aligned} \quad (2.66)$$

The compliance tensor for the material matrix is:

$$\widehat{S}^m = \begin{bmatrix} \frac{1}{E_1^m} & \frac{-\nu_{12}^m}{E_1^m} & \frac{-\nu_{13}^m}{E_1^m} & 0 & 0 & 0 \\ \frac{-\nu_{12}^m}{E_1^m} & \frac{1}{E_1^m} & \frac{-\nu_{13}^m}{E_1^m} & 0 & 0 & 0 \\ \frac{-\nu_{13}^m}{E_1^m} & \frac{-\nu_{13}^m}{E_1^m} & \frac{1}{E_3^m} & 0 & 0 & 0 \\ 0 & 0 & 0 & \frac{1}{G_3^m} & 0 & 0 \\ 0 & 0 & 0 & 0 & \frac{1}{G_3^m} & 0 \\ 0 & 0 & 0 & 0 & 0 & \frac{1}{G_1^m} \end{bmatrix} \quad (2.67)$$

with

$$\begin{aligned} \frac{1}{K_1^m} &= 3(1-\nu_{12}^m - \nu_{13}^m) / E_1^m \\ \frac{1}{K_3^m} &= 3(1-2\nu_{31}^m) / E_3^m \\ \frac{1}{K_{Reff}^m} &= \frac{2}{3K_1^m} + \frac{2}{3K_3^m} \\ \frac{1}{K_{Reff}^d} &= \frac{2(1-\nu_{12}^d - \nu_{13}^d)}{E_1^d} + \frac{1-2\nu_{31}^d}{E_3^d} \end{aligned} \quad (2.68)$$

In this case, because both \widehat{C}^d and \widehat{S}^m are transversely isotropic with respect to a common axis, the Biot effective stress coefficient vector is given by the equation (2.5),

$$\widehat{\mathbf{A}} = [\widehat{A}_r, \widehat{A}_r, \widehat{A}_z, 0, 0, 0]^T \quad (2.69)$$

where

$$\begin{aligned} \widehat{A}_r &= 1 - \frac{E_1^d}{3(1-\nu_{12}^d - 2\nu_{31}^d\nu_{13}^d)} \left(\frac{1}{K_1^m} + \frac{\nu_{31}^d}{K_3^m} \right) \\ \widehat{A}_z &= 1 - \frac{E_3^d}{3(1-\nu_{12}^d - 2\nu_{31}^d\nu_{13}^d)} \left(\frac{2\nu_{13}^d}{K_1^m} + \frac{1-\nu_{12}^d}{K_3^m} \right) \end{aligned} \quad (2.70)$$

Fluid : $\rho_f = \rho_{f0} = \text{const}$

$$\text{Solid : } \underbrace{\text{tr} \widehat{\boldsymbol{\varepsilon}}^m = \text{tr} (\widehat{\mathbf{S}}^m \cdot \widehat{\boldsymbol{\sigma}}^m)}_{\downarrow} = 0 \rightarrow \widehat{\mathbf{S}}^m \cdot \widehat{\mathbf{U}} = 0$$

$$\frac{1}{K_1^m} = \frac{1}{K_3^m} = 0, \quad \left\{ \begin{array}{l} \nu_{12}^m = 1 - \frac{E_1^m}{2E_3^m}, \\ \nu_{13}^m = \frac{E_1^m}{2E_3^m}, \quad \Lambda = 0, \quad \zeta = \widehat{\mathbf{U}} \cdot \widehat{\boldsymbol{\varepsilon}}, \quad \widehat{\mathbf{A}} = \widehat{\mathbf{U}} \\ \nu_{31}^m = \frac{1}{2} \end{array} \right.$$

Employing the stress-pore pressure-strain constitutive equation, the components of the stress vector are:

$$\begin{aligned} \sigma_{rr} &= -\widehat{A}_r p + \widehat{C}_{rr}^d \frac{\partial u}{\partial r} + \widehat{C}_{r\theta}^d \frac{u}{r} + \widehat{C}_{rz}^d \varepsilon(t), \\ \sigma_{\theta\theta} &= -\widehat{A}_r p + \widehat{C}_{r\theta}^d \frac{\partial u}{\partial r} + \widehat{C}_{rr}^d \frac{u}{r} + \widehat{C}_{rz}^d \varepsilon(t), \\ \sigma_{zz} &= -\widehat{A}_z p + \widehat{C}_{rz}^d \left(\frac{\partial u}{\partial r} + \frac{u}{r} \right) + \widehat{C}_{zz}^d \varepsilon(t). \end{aligned} \quad (2.71)$$

The only equation of equilibrium that is not satisfied automatically is

$$\frac{\partial \sigma_{rr}}{\partial r} + \frac{\sigma_{rr} - \sigma_{\theta\theta}}{r} = 0 \quad (2.72)$$

Substitution of the non-zero stress components (2.71) into the equilibrium equation (2.72) and, subsequently, integrating with respect to r , the following expression is obtained

$$\frac{\partial u}{\partial r} + \frac{u}{r} = \frac{1}{r} \frac{\partial}{\partial r} (ru) = \frac{\hat{A}_r}{\hat{C}_{rr}^d} p(r,t) + f(t) \quad (2.73)$$

where $f(t)$ is an arbitrary function of time obtained in the integration with respect to r .

The expression (2.73) is employed to evaluate two expressions for the quantity $\hat{\mathbf{A}} \cdot \hat{\boldsymbol{\varepsilon}}$, depending on the variation in fluid content ζ and on pressure p :

$$\begin{aligned} \hat{\mathbf{A}} \cdot \hat{\boldsymbol{\varepsilon}} &= \frac{\hat{A}_r^2}{\hat{C}_{rr}^d} p(r,t) + \hat{A}_z \varepsilon(t) + \hat{A}_r f(t) \\ \hat{\mathbf{A}} \cdot \hat{\boldsymbol{\varepsilon}} &= \frac{1}{J} \left\{ \hat{A}_r^2 \zeta + \Lambda \hat{C}_{rr}^d \left[\hat{A}_z \varepsilon(t) + \hat{A}_r f(t) \right] \right\} \end{aligned} \quad (2.74)$$

where

$$J = \hat{A}_r^2 + \Lambda \hat{C}_{rr}^d$$

It has to be noticed that the quantity J is equal in both compressible and incompressible cases. In the case of transverse isotropy,

$$J = \left[1 - \frac{E_1^d}{3(1 - \nu_{12}^d - 2\nu_{31}^d \nu_{13}^d)} \left(\frac{1}{K_1^m} + \frac{\nu_{31}^d}{K_3^m} \right) \right]^2 + \Lambda \frac{E_1^d (1 - \nu_{31}^d \nu_{13}^d)}{(1 + \nu_{12}^d)(1 - \nu_{12}^d - 2\nu_{31}^d \nu_{13}^d)} \quad (2.75)$$

A diffusive differential equation for the pore pressure is obtained by substituting the first equation (2.74) into the equation (2.57)

$$\frac{\partial^2 p}{\partial r^2} + \frac{1}{r} \frac{\partial p}{\partial r} - \frac{1}{c} \frac{\partial p}{\partial t} = \frac{\mu}{K_{rr}} \left(\hat{A}_z \frac{\partial \varepsilon}{\partial t} + \hat{A}_r \frac{\partial f}{\partial t} \right) \quad (2.76)$$

and a diffusive differential equation for the variation in fluid content is determined substituting the second equation (2.74) into the equation (2.55)

$$\frac{\partial^2 \zeta}{\partial r^2} + \frac{1}{r} \frac{\partial \zeta}{\partial r} - \frac{1}{c} \frac{\partial \zeta}{\partial t} = 0 \quad (2.77)$$

where

$$c = \frac{K_{rr} \widehat{C}_{rr}^d}{\mu J} \quad (2.78)$$

A comparison of equations (2.76) and (2.77) highlights that both the pore pressure and the variation in fluid content satisfy the same differential equation, but the differential equation for pressure has an inhomogeneous part and, so, it is more convenient to solve the differential equation for the variation in fluid content, to find, then, the pore pressure, by equating the two expressions (2.74) for $\widehat{\mathbf{A}} \cdot \widehat{\boldsymbol{\varepsilon}}$. For this purpose, an equation that can be solved for the pressure $p(r, t)$ in terms of the variation in fluid content $\zeta(r, t)$ and the strain applied to the plates $\varepsilon(t)$ is necessary,

$$p(r, t) = \frac{\widehat{C}_{rr}^d}{J} \left\{ \zeta(r, t) - \widehat{A}_z \varepsilon(t) + \widehat{A}_r f(t) \right\} \quad (2.79)$$

The differential equation (2.73) for the displacement field $u(r, t)$ can be rearranged in terms of the variation in fluid content $\zeta(r, t)$ and the strain applied to the plates $\varepsilon(t)$ by substituting for the pressure $p(r, t)$ from (2.79) into (2.73),

$$\frac{\partial u}{\partial r} + \frac{u}{r} = \frac{1}{r} \frac{\partial}{\partial r} (ru) = \frac{1}{J} \left\{ \widehat{A}_r \zeta(r, t) - \widehat{A}_r \widehat{A}_z \varepsilon(t) + \Lambda \widehat{C}_{rr}^d f(t) \right\} \quad (2.80)$$

To solve the differential equation (2.77), it is necessary first to express it in terms of dimensionless arguments by introducing a dimensionless time τ and a dimensionless radius λ , thus

$$\tau = \frac{ct}{b^2}, \quad \lambda = \frac{r}{b} \quad (2.81)$$

Equation (2.77), thus, becomes

$$\frac{\partial^2 \zeta}{\partial \lambda^2} + \frac{1}{\lambda} \frac{\partial \zeta}{\partial \lambda} - \frac{\partial \zeta}{\partial \tau} = 0 \quad (2.82)$$

and it is solved employing the Laplace transform. In the following, the Laplace transform of a function is indicated by a tilde (\sim) over the function and the independent variable will shift from t to s . The Laplace transform of (2.77) becomes a Bessel differential equation in the variation in fluid content $\tilde{\zeta}(\lambda, s)$,

$$\frac{\partial^2 \tilde{\zeta}}{\partial \lambda^2} + \frac{1}{\lambda} \frac{\partial \tilde{\zeta}}{\partial \lambda} - s \tilde{\zeta} = 0 \quad (2.83)$$

The solution to (2.83) is given by Detournay and Cheng (Detournay and Cheng, 1993) and can be written as

$$\tilde{\zeta}(\lambda, s) = Jg(s)I_0(\lambda\sqrt{s}) \quad (2.84)$$

where I_0 is a modified Bessel function of the first kind, $g(s)$ is an arbitrary function of the transformed variable to be determined, and the coefficient J , defined by (2.74), is introduced for convenience. The solution of (2.83) also contains a term proportional to a modified Bessel function of the second kind. However, the function has a singularity as λ tends to 0 and, so, the requirement for a finite solution at $\lambda=0$ justifies to impose the arbitrary function of the transformed variable associated with the second kind of Bessel function equal to zero. To eliminate the function $f(\tau)$ or, actually, its Laplace transform $\tilde{f}(s)$, the boundary condition on the pore pressure at $\lambda=1$ is used. Employing the solution (2.84), the Laplace transform of (2.79) yields the following formula for the Laplace transform of the pressure $\tilde{p}(\lambda, s)$:

$$\tilde{p}(\lambda, s) = \frac{\hat{C}_{rr}^d}{J} \left\{ Jg(s)I_0(\lambda\sqrt{s}) - \hat{A}_z \tilde{\varepsilon}(s) - \hat{A}_r \tilde{f}(s) \right\} \quad (2.85)$$

The function $\tilde{f}(s)$ is evaluated imposing that the pore fluid pressure is zero at the curved lateral surface $\lambda = 1$, thus

$$\tilde{f}(s) = \frac{1}{\widehat{A}_r} \left[Jg(s)I_0(s) - \widehat{A}_z \tilde{\varepsilon}(s) \right] \quad (2.86)$$

Substituting (2.86) into (2.85), the Laplace transform of the pressure $\tilde{p}(r, s)$ is obtained as

$$\tilde{p}(\lambda, s) = \widehat{C}_{rr}^d g(s) \left\{ I_0(\lambda\sqrt{s}) - I_0(\sqrt{s}) \right\} \quad (2.87)$$

Substituting the solution (2.84) for the Laplace transform of the variation in fluid content $\tilde{\zeta}(\lambda, s)$ into the Laplace transform of the differential equation (2.80) for the displacement $\tilde{u}(r, s)$ and employing (2.86), it follows that

$$\frac{1}{b\lambda} \frac{\partial}{\partial \lambda} (\lambda \tilde{u}) = \widehat{A}_r g(s) I_0(\lambda\sqrt{s}) - \frac{\widehat{A}_z}{\widehat{A}_r} \tilde{\varepsilon}(s) + \frac{\Lambda \widehat{C}_d^{rr}}{\widehat{A}_r} g(s) I_0(\sqrt{s}) \quad (2.88)$$

Integration of this differential equation yields

$$\tilde{u}(\lambda, s) = \frac{1}{2} b\lambda \left\{ \widehat{A}_r g(s) \left[2h(\lambda, s) + \frac{\Lambda \widehat{C}_d^{rr}}{\widehat{A}_r^2} \right] I_0(\sqrt{s}) - \frac{\widehat{A}_z}{\widehat{A}_r} \tilde{\varepsilon}(s) \right\} \quad (2.89)$$

where the function $h(\lambda, s)$,

$$h(\lambda, s) \equiv \frac{I_1(\lambda\sqrt{s})}{\lambda\sqrt{s}I_0(\sqrt{s})} \quad (2.90)$$

has been introduced. This function monotonically decreases from a value of $\frac{1}{2}$ at $s = 0$ to a value of 0 as s tends to infinity. The function $g(s)$ is evaluated by calculating the stress T_{rr} on the curved lateral boundary at $\lambda = 1$ and imposing that it is equal to zero. The formula

(2.89) for $\tilde{u}(\lambda, s)$ is, thus, substituted in the Laplace transform of the first expression in (2.71) for the radial stress σ_{rr} ; the function $g(s)$ is found to be given by

$$g(s) = \frac{B\tilde{\varepsilon}(s)}{[C - Dh(1, s)]I_0(\sqrt{s})} \quad (2.91)$$

where B , C , and D are given by

$$\begin{aligned} B &= \frac{1}{2\Delta_2} (\widehat{A}_z - 2\nu_{31}\widehat{A}_r) \\ C &= \widehat{A}_r^2 + \frac{\Lambda E_1}{2\Delta_1} \quad \text{and} \quad D = \frac{\widehat{A}_r^2}{\Delta_2} (2\Delta_2 - 1) \end{aligned} \quad (2.92)$$

Replacing the expression (2.91) in the equation (2.84), the Laplace transform of the variation in fluid content $\tilde{\zeta}(\lambda, s)$ may be written as

$$\tilde{\zeta}(\lambda, s) = \frac{B\tilde{\varepsilon}(s)}{[C - Dh(1, s)]} \frac{I_0(\lambda\sqrt{s})}{I_0(\sqrt{s})} \quad (2.93)$$

and the Laplace transform of the radial displacement becomes

$$\tilde{u}(\lambda, s) = -\frac{b\lambda}{2\widehat{A}_r} \left[\widehat{A}_z - B \frac{\Lambda \widehat{C}_d^{rr} + 2\widehat{A}_r^2 h(\lambda, s)}{C - Dh(1, s)} \right] \tilde{\varepsilon}(s) \quad (2.94)$$

Substituting (2.91) into (2.87), it is possible to express $\tilde{p}(\lambda, s)$ as

$$\frac{\tilde{p}(\lambda, s)}{\widehat{C}_{rr}^d - \widehat{C}_{r\theta}^d} = \frac{B\widehat{A}_r^2}{D} \left[\frac{I_0(\lambda\sqrt{s})}{I_0(\sqrt{s})} - 1 \right] \frac{\tilde{\varepsilon}(s)}{[C - Dh(1, s)]} \quad (2.95)$$

To evaluate the total force $P(t)$ applied to the circular flat plate, the first step consists in the combination of the equation (2.73) with the last of (2.71) to obtain a representation for the stress component σ_{zz} in terms of only $p(r,t)$ and $\varepsilon(t)$, thus

$$\sigma_{zz} = -\frac{\widehat{A}_z \widehat{C}_{rr}^d - \widehat{A}_r \widehat{C}_{rz}^d}{\widehat{C}_{rr}^d} p(r,t) + \widehat{C}_{rz}^d f(t) + \widehat{C}_{zz}^d \varepsilon(t) \quad (2.96)$$

The total force $P(t)$ applied to the circular flat plate is then expressed as

$$\begin{aligned} P(t) &= 2\pi \int_0^b \sigma_{zz} r dr = -\frac{2\pi}{\widehat{C}_{rr}^d} \left(\widehat{A}_z \widehat{C}_{rr}^d - \widehat{A}_r \widehat{C}_{rz}^d \right) \int_0^b p r dr + \pi b^2 \widehat{C}_{zz}^d \varepsilon(t) + \\ &+ \pi b^2 \widehat{C}_{rz}^d f(t) \end{aligned} \quad (2.97)$$

Substituting the expression (2.95) for $\tilde{p}(\lambda, s)$ and the expression (2.86) for $\tilde{f}(s)$ into the Laplace transform of (2.97),

$$\begin{aligned} \tilde{P}(s) &= 2\pi b^2 \int_0^1 \tilde{\sigma}_{zz} \lambda d\lambda = -\frac{2\pi b^2}{\widehat{C}_{rr}^d} \left(\widehat{A}_z \widehat{C}_{rr}^d - \widehat{A}_r \widehat{C}_{rz}^d \right) \int_0^1 \tilde{p} \lambda d\lambda + \pi b^2 \widehat{C}_{zz}^d \varepsilon(s) \\ &+ \pi b^2 \widehat{C}_{rz}^d \tilde{f}(s) \end{aligned} \quad (2.98)$$

with some rearrangement of terms, the following relationship is obtained

$$\frac{2\tilde{P}(s)}{\pi b^2 \left(\widehat{C}_{rr}^d - \widehat{C}_{r\theta}^d \right)} = \frac{M - Nh(1, s)}{C - Dh(1, s)} \tilde{\varepsilon}(s) \quad (2.99)$$

where M and N are defined by the relations

$$\begin{aligned} M &= C_{eff}^d \frac{E_3}{2\Delta_2 - 1} \\ N &= \frac{2E_3}{2\Delta_2 - 1} \left(C_{eff}^d - J \frac{\Delta_1}{E_1 \Delta_2} \right) \end{aligned} \quad (2.100)$$

The result (2.99) can be used both to evaluate the total load $P(t)$ generated on a specimen by an arbitrary strain history $\varepsilon(t)$ or to determine $\varepsilon(t)$ if the total load $P(t)$ is prescribed. The displacement field and the pore pressure field may be evaluated for an imposed load history by solving the equation for $\tilde{\varepsilon}(s)$ and, then, substituting the result into the equations for the displacement field and the pore pressure field. In that way, the solution for the linear poroelastic, transversely isotropic, unconfined-compression, creep and stress-relaxation analysis is completed. Before inverting these expressions, it is necessary to observe some mathematical properties of the Laplace transform solution equations for $\tilde{u}(\lambda, s)$, $\tilde{p}(\lambda, s)$ and $\tilde{P}(s)$, recalling the initial and final value theorems. For these theorems,

$$\lim_{s \rightarrow 0} s \tilde{f}(s) = \lim_{t \rightarrow \infty} f(t) \quad \text{and} \quad \lim_{s \rightarrow \infty} \tilde{f}(s) = \lim_{t \rightarrow 0} f(t)$$

These conditions are satisfied by the solutions for displacement field, pressure field and the total force. The problem considered concerns the application of a step loading $\varepsilon(t) = \varepsilon_0 H(t)$, whose Laplace transform is $\tilde{\varepsilon}(s) = \frac{\varepsilon_0}{s}$. Applying the initial and final value theorems, the following relationships are obtained,

$$u(1, 0) = -\frac{b\varepsilon_0}{2\hat{A}_r} \left(\hat{A}_z - \frac{B}{C} \Lambda \hat{C}_{rr}^d \right) \quad (2.101)$$

and

$$u(1, \infty) = -\frac{b\varepsilon_0}{2\hat{A}_r} \left(\hat{A}_z - \frac{2BJ}{2C - D} \right) \quad (2.102)$$

Equation (2.102) shows that the displacement at the outer boundary of the disk is initially larger than the final displacement, $u(1, 0) > u(1, \infty)$, because there is no fluid flow initially and, thus, the disk behaves like an incompressible object, whose elasticity is determined by the undrained elastic constants. Due to the compressive loading, in the axial direction there is a volume reduction of the disk which may be balanced by an equal volume expansion in the radial direction. As time increases, the fluid flows from the disk across the lateral

boundaries. The displacement of the outer boundary of the disk, thus, diminishes to an equilibrium value, determined by the drained elastic constants. The inverse Laplace transforms of the solution equations is obtained employing standard methods. These solutions are all of the fractional form $p(s)/q(s)$, the inverse of which is

$$\mathcal{L}^{-1}\left[\frac{p(s)}{q(s)}\right] = \sum_{n=1}^{\infty} \frac{p(\alpha_n)}{q'(\alpha_n)} e^{\alpha_n ct/b^2}$$

where $p(s)$ and $q(s)$ are analytic at $s = \alpha_n$ and α_n are simple poles of p/q . In stress relaxation, the axial compressive strain history is given by $\varepsilon(t) = \varepsilon_0 H(t)$, where $H(t)$ is the Heaviside step function and $\tilde{\varepsilon}(s) = \frac{\varepsilon_0}{s}$. The resulting dimensional load history $P(t)$ may, then, be evaluated using the method proposed by Cohen et al. (Cohen et al., 1998) for the transversely isotropic incompressible case.

For a compressible material, subjected to a step loading, the application of this method will yield,

$$\frac{P(t)}{\pi b^2} = E_3^d \varepsilon_0 + E_1^d \varepsilon_0 \left(b^2 / c \right) \Delta_3' \sum_{n=1}^{\infty} A_n e^{\alpha_n^2 ct/b^2} \quad (2.103)$$

where

$$A_n = \frac{1}{C^2 \Delta_2'^2 \alpha_n^2 - \Delta_1' / (1 + \nu_{12})} \quad (2.104)$$

and

$$\begin{aligned} \Delta_1' &= \Delta_1 \frac{\hat{A}_r^2}{J}, \Delta_2' = \Delta_2 \frac{1}{J}, \\ \Delta_3' &= \Delta_3 \frac{\nu_{31} \Delta_1}{\nu_{13} (1 - 2\nu_{31})^2 J^2} \left(C_{eff}^d J \frac{E_1}{\Delta_1} - 2J + \Lambda \frac{E_1}{1 + \nu_{12}} \right) \end{aligned} \quad (2.105)$$

In equation (2.103), α_n are the roots of the characteristic equation $J_1(x) - \frac{C}{D} x J_0(x) = 0$, where $J_0(x)$ and $J_1(x)$ are Bessel functions. If the constituents are incompressible, the expressions (2.105) reduce to

$$\Delta'_1 = \Delta_1, \Delta'_2 = \Delta_2, \Delta'_3 = \Delta_3 \quad (2.106)$$

Substituting (2.106) into (2.103) and (2.104), it then follows from (2.103) that for the incompressible case

$$\frac{P(t)}{\pi b^2} = E_3^d \varepsilon_0 + E_1^d \varepsilon_0 (b^2 / c) \sum_{n=1}^{\infty} \frac{1}{\Delta_2^2 \alpha_n^2 - \Delta_1 / (1 + \nu_{12})} e^{\alpha_n^2 ct / b^2} \quad (2.107)$$

The expression (2.107) for $P(t)$ is identical to Eq. (15) of Cohen et al. (Cohen et al., 1998). Cohen et al. (Cohen et al., 1998) also obtained an analytical solution for the experimentally significant case of a ramp loading for the transversely isotropic incompressible material. The ramp loading is characterized by a constant strain rate $\dot{\varepsilon}_0$ and a period of duration t_0 during which the applied strain is rising linearly from a value of 0 to $t_0 \dot{\varepsilon}_0$. After time t_0 , the value of $\varepsilon(t)$ is constant at $t_0 \dot{\varepsilon}_0$. In terms of the Heaviside step function $H(t)$,

$$\varepsilon(t) = \dot{\varepsilon}_0 [tH(t) - (t - t_0)H(t - t_0)] \quad (2.108)$$

For the specified ramp loading, the solution for $P(t)$ is given by

$$\begin{aligned} \frac{P(t)}{\pi b^2} &= \dot{\varepsilon}_0 E_3^d + E_1^d \varepsilon_0 (b^2 / c) \Delta'_3 \left[\frac{1}{8} - \sum_{n=1}^{\infty} \frac{A_n}{\alpha_n^2} e^{-\alpha_n^2 ct / b^2} \right] \\ &\text{for } 0 < t < t_0 \text{ and} \\ \frac{P(t)}{\pi b^2} &= \dot{\varepsilon}_0 E_3^d - E_1^d \dot{\varepsilon}_0 (b^2 / c) \Delta'_3 \left\{ \sum_{n=1}^{\infty} \frac{A_n}{\alpha_n^2} \left[e^{-\alpha_n^2 ct / b^2} - e^{-\alpha_n^2 c(t-t_0) / b^2} \right] \right\} \\ &\text{for } t > t_0 \end{aligned} \quad (2.109)$$

Using (2.106), it is easy to show that the expressions (2.109) for $P(t)$ reduce to the corresponding equations of Cohen et al. (Cohen et al., 1998) for the incompressible case. The compressible case results represent a good model for bone tissue experiments, while the incompressible ones are ideal for cartilaginous tissue experiments.

2.2 Isotropic poroelastic models with non linear permeability and elasticity

Experimental studies on biological structures highlight that hard and soft tissues are porous media exhibiting very different behaviors, above all for the levels of strains experienced. Hard tissues are usually characterized by small strains levels, while soft tissues can be subjected to large strains. Poroelasticity theory has been, thus, extended to take into account non linear effects associated to the permeability as well as to the elastic behavior. An example is furnished by hydrated soft tissues for which the permeability is strain dependent. To model this aspect, several forms of empirical equations for deformation-dependent permeability have been proposed to analyze the fluid flow within a tissue under mechanical loading. This effect plays an important role in both the mechanics of tissues and the associated fluid transport. For articular cartilage and intervertebral disc, Holmes and Mow (Holmes and Mow, 1990) proposed the following relationship between the permeability K^P and the stretch ratio, λ

$$K_p(\lambda) = K_0 \left(\frac{\lambda - 1 + \phi_0}{\phi_0} \right)^\zeta \exp \left[m(\lambda^2 - 1) / 2 \right] \quad (2.110)$$

ensuring that the permeability decreases with compression. In the equation (2.110), K_0 is the zero strain permeability, m and ζ are non dimensional parameters relating K_p to λ and ϕ is the porosity. The subscript 0 indicates zero strain values. The relationship between the porosity and the stretch ratio is given by $\phi = 1 - \frac{1 - \phi_0}{\lambda}$. The monoaxial stretch λ is evaluated as the ratio between the compressed sample height and the original one. As

$\lambda \rightarrow 1$, small deformations will occur and, so, $K_p(\lambda) = K_0$ and $\phi = \phi_0$. The relationship (2.110) can also be used to model solute transport in agarose gels (Urciuolo et al. 2008).

Lai and Mow (Lai and Mow, 1980) proposed, instead, an easier form of this relationship

$$K_p(\lambda) = K_0 \exp[m(\lambda - 1)] \quad (2.111)$$

Also in this case, as $\lambda \rightarrow 1$, small deformation will occur. Riches et al. (Riches et al. 2002), found rather a link between the permeability and the porosity, expressed by the equation

$$K_p = K_0 \left(\frac{\phi}{\phi_0} \right)^n \quad (2.112)$$

where n is a non dimensional material parameter. When $\phi = \phi_0$, $k = k_0$. Moreover, Argoubi et al. (Argoubi et al., 1996) determined a connection between the tissue permeability and both the porosity and the stretch ratio

$$K_p = K_0 \left(\frac{\phi}{\phi_0} \right)^2 \exp[m(\lambda - 1)] \quad (2.113)$$

It has to be noticed that equations (2.111) and (2.113) are estimated in the hypothesis of small deformations. In finite deformation, instead, large strains can significantly alter the tissue porosity. Consequently, the solid and fluid fractions and the permeability are related to the tissue dilatation. Heneghan et al. (Heneghan et al. 2008) compared the different approaches to determine the more appropriate model to describe the compressive behavior and the convective transport of nutrients within the intervertebral disc, as shown in Figure 2.1. The plot is referred to the parameter values proposed by the authors.

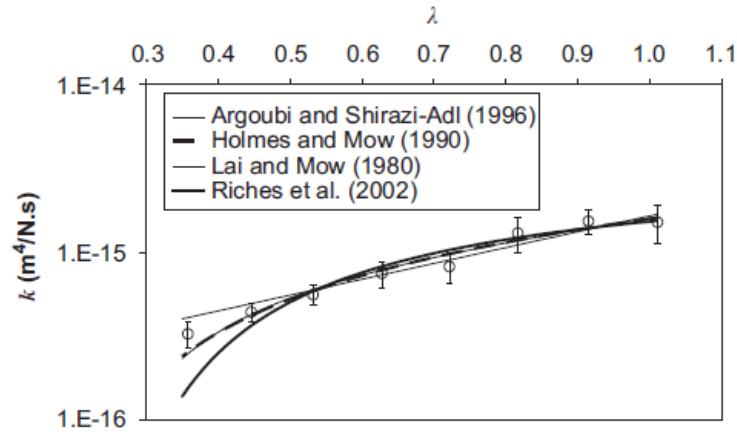


Figure 2.1

Plot of k against λ comparing the four permeability equations proposed (Heneghan et al. 2008)

They concluded that the intervertebral disc behavior, characterized by a decreasing permeability with compression, is best described by the model proposed by Holmes and Mow (Holmes and Mow, 1990), (2.110), based on finite deformation, as shown in equation (2.114)

$$K(\lambda) = 1.59 \times 10^{-15} \left(\frac{\lambda - 0.2}{0.8} \right)^{1.13} \exp \left[-0.02(\lambda^2 - 1) / 2 \right] \quad (2.114)$$

Besides, non linear effects are associated also to the elastic behavior of soft tissues. In most studies of the compressive properties of articular cartilage, only infinitesimal strain theories have been used to analyze experimental data. However, physiologic joint loads and stresses are usually quite high and, so, cartilage could easily be subject to finite deformation under many physiological situations. Various forms of the finite deformation biphasic theory have been developed to describe cartilaginous tissues (Holmes and Mow, 1990). These theories, have various strain-energy and strain-dependent permeability functions, and are mathematically valid under various material assumptions. Ateshian et al. (Ateshian et al. 1997) demonstrated that the finite deformation biphasic theory developed by Holmes and Mow (Holmes and Mow, 1990) can describe both the kinetic and equilibrium compressive behaviors of cartilage under high strain fields. In the finite deformation theory proposed by Holmes and Mow (Holmes and Mow, 1990), the solid

matrix is supposed to be isotropic. According to the biphasic theory, previously exposed, the stresses in the solid and fluid phases are

$$\begin{aligned}\boldsymbol{\sigma}^f &= -\varphi^f p \mathbf{I} \\ \boldsymbol{\sigma}^s &= -\varphi^s p \mathbf{I} + \boldsymbol{\sigma}^m\end{aligned}\quad (2.115)$$

and the principal components of the stress tensor of the solid matrix, $\boldsymbol{\sigma}^m$, are related to the principal components of stretch, λ_1 , λ_2 and λ_3 by the following constitutive relations

$$\sigma_i^m = \frac{1}{2} H_{A0} \Phi \frac{\lambda_i}{\lambda_j \lambda_k} \left\{ \frac{1-3\nu}{1-\nu} + \frac{\nu}{1-\nu} [\lambda_j^2 + \lambda_k^2] - \frac{1}{\lambda_i^2} \right\} \quad (2.116)$$

where i, j and k permute over 1, 2 and 3 and Φ is given by

$$\Phi = \exp \left\{ \beta \left[\frac{1-3\nu}{1-\nu} (J_1 - 3) + \frac{\nu}{1-\nu} (J_2 - 3) - \ln(J_3) \right] \right\} \quad (2.117)$$

H_{A0} is the aggregate modulus, ν is a non dimensional coefficient, which reduces to the solid phase Poisson's ratio under infinitesimal strains; the compressive-stiffening coefficient β is a non-dimensional constant which measures the sensitivity of $\boldsymbol{\sigma}^m$ to large strains (Holmes and Mow, 1990). The quantities J_1 , J_2 and J_3 are the invariants of the left Cauchy-Green strain tensor \mathbf{B}_{CG} of the solid phase. Along principal directions of stretch, the components of \mathbf{B}_{CG} are all zero except for the three diagonal entries λ_1^2 , λ_2^2 and λ_3^2 . In these directions, the invariants $J_1 = \text{tr} \mathbf{B}_{CG}$, $J_2 = \frac{1}{2} [(\text{tr} \mathbf{B}_{CG})^2 - \text{tr} \mathbf{B}_{CG}^2]$ and $J_3 = \det \mathbf{B}_{CG}$ can be easily determined.

In this theory, the solid and fluid fractions and the permeability are related to the tissue dilatation by the following relationships:

$$\begin{aligned} \varphi^s &= \frac{\varphi_0^s}{\sqrt{J_3}}, \quad \varphi^f = 1 - \frac{\varphi_0^s}{\sqrt{J_3}}, \\ K^P &= K_0 \left[\frac{\varphi_0^s \varphi^f}{(1 - \varphi_0^s) \varphi^s} \right]^2 \exp\{m(J_3 - 1)/2\} \end{aligned} \quad (2.118)$$

φ_0^s and K_0 are, respectively, the solid content and the permeability of the tissue in the absence of strain, and m is the non-dimensional permeability coefficient weighting the exponential functional dependence on strain. Thus, the material behavior of an isotropic hyperelastic biphasic tissue is completely determined by the five material coefficients H_{A0} , β , ν , K_0 and m . The finite deformation theory proposed by Holmes and Mow (Holmes and Mow, 1990) has been used to model also the behavior of the human annulus fibrosus in confined compression (Iatridis et al. 1998). A biphasic hyperelastic element model has been proposed for the description of the mechanical behavior of brain tissue (Garcia and Smith, 2008). The model takes into account finite deformations through an Ogden-type hyperelastic compressible function and an hydraulic conductivity dependent on deformation. The solid phase is represented by an hyperelastic isotropic energy function W as

$$W = \sum_{i=1}^N \frac{\mu_i}{a_i} \left(\lambda_r^{\alpha_i} + 2\lambda_\theta^{\alpha_i} - 3 - a_i \ln(J_0) \right) + \frac{\mu'}{2} (J_0 - 1)^2 \quad (2.119)$$

where λ_r and λ_θ are, respectively, the radial and circumferential stretch ratios, μ_i , a_i and μ' are material parameters and J_0 is the determinant of the deformation gradient tensor.

The material parameters can be arranged to obtain the Young's modulus E and the Poisson's coefficient, ν , at zero strain as follows

$$E = (1 + \nu) \sum_{i=1}^N a_i \mu_i$$

$$\nu = \frac{\mu'}{2\mu' + \sum_{i=1}^N a_i \mu_i} \quad (2.120)$$

The incompressible form of this energy function allows reproducing the non linear behavior of brain tissue under finite deformations. Moreover, the permeability is modeled as a function of the tissue dilatation,

$$K_P = K_0 \exp(me) \quad (2.121)$$

where the volume dilatation e is expressed as $e = \lambda_r + 2\lambda_\theta - 3$.

CHAPTER III

UNIFIED MIXTURE THEORY

3.1 Mixture Theory

3.1.1 Introduction

Poroelasticity theory and mixture theory are both employed to describe the behavior of porous media. As highlighted before, porous media can be characterized by compressible or incompressible constituents, with significant differences in the interaction between the interstitial fluid and the solid matrix. As Leonardo da Vinci noted in his *Codex Leicester*, the porous medium behavior of hard tissues is similar to the behavior of saturated porous rocks, such as marble and granite, while the porous medium behavior of soft tissues is similar to the behavior of saturated porous soils. In both cases, saturated porous media are considered, but their behavior is significantly different. Hard tissues and, so, saturated porous rocks, are characterized, in fact, by three peculiar features:

- They do not exhibit swelling
- Only a fraction of the hydrostatic pressure is transferred to the pore fluid
- The strain levels are, usually, small

On the contrary, the peculiar features of soft tissues and, thus, saturated porous soils, are

- They exhibit swelling
- The strains can be large
- The bulk stiffness of the matrix material is about the same as the bulk stiffness of water and, then, almost all the hydrostatic stress in the solid matrix is transferred to the pore fluid (for these materials, in fact, the Skempton coefficient approaches 1)

The response to volumetric deformation of the fluid and the solid matrix in soft tissues is much stiffer than the deviatoric response; as a consequence, the fluid and the solid matrix are considered incompressible. Soft tissues result, thus, hard respect to the hydrostatic deformations and soft respect to shear or deviatoric deformations. The hypothesis of

incompressibility is, thus, valuable for soft tissues, but not for hard ones. Soft tissues are modeled employing the mixture theory, a more general approach respect to Biot's poroelasticity theory because it furnishes the possibility to follow the behavior of many components of the porous medium. Poroelasticity theory and mixture theory, thus, can be both employed to model the behavior of porous media but they differ for the averaging technique applied (Cowin, 2001). Poroelasticity theory originates in the solid mechanics tradition and the effective material properties are evaluated from a representative volume element (RVE). Biot first introduced the effective medium approach, defining a small cubic element of soil, with sides parallel to the coordinate axes, large enough respect to the pore sizes, to be considered homogeneous and, in the same time, small enough compared to the scale of the macroscopic phenomena of interest, to be considered as infinitesimal in the mathematical treatment. Mixture theory, instead, is based on diffusion models. This theory originates in the fluid mechanics and thermodynamics tradition and it describes a material as a continuum mixture of n phases, such that each spatial point in the mixture is occupied simultaneously by all the phases. Each phase has a density, a displacement field, a body force density, a partial stress, a partial internal energy density, a partial heat flux and a partial heat supply density and, thus, continuity, momentum, and energy equations can be derived for each constituent. Employing an Eulerian approach, the flux of the various species toward and away from a fixed spatial point is analyzed. Truesdell introduced three basic principles for the theory of mixtures as follows:

- 1) every property of the mean motion of the mixture is a mathematical consequence of the properties of the motion of the constituents,
- 2) the balance laws for the mixture as a whole have the same form as the equations for a single phase mixture,
- 3) Considering n phases, if the volume fraction of one of them is equal to zero, then the equations should reduce to those for a material composed of $n - 1$ phases.

The mixture theory results advantageous when different fluid species are considered, in relative motion. As underlined before, the key difference between the effective medium approach and the mixture approach to poroelastic models is the averaging process employed. The effective parameter approach illustrated in Figure 3.1a is a schematic version of the averaging technique described by Biot, who first introduced the concept of a small but finite volume of the porous medium to develop the constitutive equations for the fluid-infiltrated solid, valid in a point in the continuum. This approach enables to better understand the effective solid mechanical parameters like effective solid moduli than the

mixture theory approach. The averaging process for the mixture approach is illustrated, instead, in Figure 3.1b, where the vectors represent the velocities of various species passing through the fixed spatial point. It has to be noticed that, for mixture theory, the averaging is density-weighted on the basis of the density of each species in the mixture, instead of being averaged over a finite volume of the porous solid as in the effective medium approach. Moreover, different authors emphasize the possibility to recover the Biot constitutive equations from the mixture theory approach.

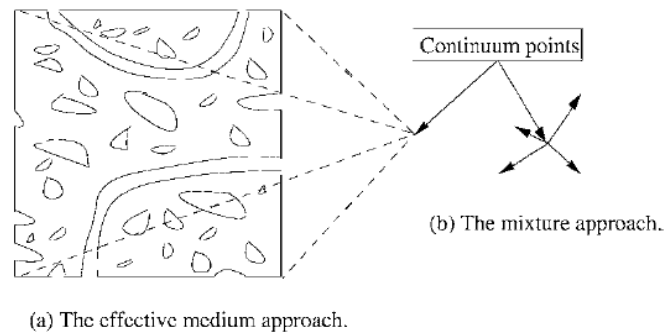


Figure 3.1

(a) The effective medium approach, (b) The mixture approach

The mixture theory proposed in the following (Cowin, 2007) is based on the assumptions that the constituents are incompressible, immiscible, non reacting and all at the same temperature, θ . The approach proposed by Cowin to deal about the mixture theory results very interesting because it allows to derive the poroelasticity theory from mixture theory.

3.1.2 Kinematics of mixtures

In the mixture theory, each place \mathbf{x} is supposed to be occupied by several different particles, one for each constituent, $\mathbf{X}^{(a)}$, $a = 1, 2, \dots, N$ of the mixture.

It is possible a material description of motion, including all the constituents

$$\mathbf{x} = \chi(\mathbf{X}^{(a)}, t) \quad \text{for all } \mathbf{X}^{(a)} \in O_{(a)}(0) \quad (3.1)$$

where $O_{(a)}(0)$ indicates the configuration at $t = 0$. The expression material description is used because the material particles $\mathbf{X}^{(a)}$ are the independent variables. Once the motion is known, all the kinematics variables can be determined, such as velocities, accelerations, displacements, strains, etc.

The inverse of motion is

$$\mathbf{X}^{(a)} = (\chi^{(a)})^{-1}(\mathbf{x}, t) \quad \text{for all } \mathbf{X}^{(a)} \in O_{(a)}(0) \quad (3.2)$$

The deformation gradient for the a th constituent is defined as

$$\mathbf{F}^{(a)} = \left[\nabla^{(a)} \otimes \chi(\mathbf{X}^{(a)}, t) \right]^T \quad \text{for all } \mathbf{X}^{(a)} \in O_{(a)}(0) \quad (3.3)$$

where the symbol $\nabla^{(a)}$ indicates the gradient with respect to the material coordinate system, \mathbf{x} . The inverse of the deformation gradient, from equation (3.3) is given by

$$\left(\mathbf{F}^{(a)} \right)^{-1} = \left[\nabla \otimes (\chi^{(a)})^{-1}(\mathbf{x}, t) \right]^T \quad \text{for all } \mathbf{x} \in O_{(a)}(0) \quad (3.4)$$

where the symbol ∇ indicates the gradient with respect to the spatial coordinate system.

The determinant of the tensor of the deformation gradient for the a th constituent, is the Jacobian of the transformation from \mathbf{x} to \mathbf{X} and, thus,

$$J_{(a)} \equiv \text{Det} \mathbf{F}^{(a)} = \frac{1}{\text{Det} \left(\mathbf{F}^{(a)} \right)^{-1}} \quad (3.5)$$

with the constraints $0 < \mathbf{J}^{(a)} < \infty$, ensuring that finite continuum volumes always remain finite. The velocity $\mathbf{v}^{(a)}$ and the acceleration $\frac{D^{(a)} \mathbf{v}^{(a)}}{Dt}$ of a particle of the a th constituents are defined as

$$\begin{aligned} \mathbf{v}^{(a)} &= \frac{D^a \mathbf{x}^{(a)}}{Dt} = \left. \frac{\partial \chi^{(a)}(\mathbf{X}^{(a)}, t)}{\partial t} \right|_{\mathbf{X}^{(a)} \text{ fixed}} \\ \frac{D^a \mathbf{v}^{(a)}}{Dt} &= \left. \frac{\partial^2 \chi^{(a)}(\mathbf{X}^{(a)}, t)}{\partial t^2} \right|_{\mathbf{X}^{(a)} \text{ fixed}} \end{aligned} \quad (3.6)$$

In the equations (3.6), $\mathbf{X}^{(a)}$ represents the velocity or the acceleration of particle $\mathbf{X}^{(a)}$ that is being determined and, so, it is kept constant. The spatial description of motion of particle $\mathbf{X}^{(a)}$ (the material description is represented, instead by the equation (3.1)) can be obtained by replacing equation (3.2) in the equation (3.6) for the velocity, thus

$$\mathbf{v}^{(a)} = \frac{D^a \chi^{(a)} \left(\left(\chi^{(a)} \right)^{-1}(\mathbf{x}, t), t \right)}{Dt} = \mathbf{v}^{(a)}(\mathbf{x}, t) \quad (3.7)$$

The derivative $\frac{D^{(a)}}{Dt}$ is the material time derivative of the a th constituent, i.e. the time derivative evaluated by following the material particle $\mathbf{X}^{(a)}$ and, thus, it is the time derivative determined keeping constant $\mathbf{X}^{(a)}$.

If $\Gamma(\mathbf{x}, t)$ is an arbitrary function, the material time derivative of the a th constituent is

$$\left. \frac{D^a \Gamma}{Dt} = \frac{\partial \Gamma(\chi^{(a)}(\mathbf{X}^{(a)}, t))}{\partial t} \right|_{\mathbf{X}^{(a)} \text{ fixed}} \quad (3.8)$$

This derivative can be written as

$$\frac{D^a \Gamma}{Dt} = \frac{\partial \Gamma(\mathbf{x}, t)}{\partial t} + \mathbf{v}^{(a)} \cdot \nabla [\Gamma(\mathbf{x}, t)] \quad (3.9)$$

The tensor of velocity gradients for the a th constituent is determined evaluating the spatial gradient of the velocity field for the a th constituent

$$\mathbf{L}^{(a)} = \nabla \otimes \mathbf{v}^{(a)} \quad (3.10)$$

The tensor of velocity gradients has also another representation

$$\mathbf{L}^{(a)} = \frac{D^a \mathbf{F}^{(a)}}{Dt} (\mathbf{F}^{(a)})^{-1} \quad (3.11)$$

In the mixture theory, two different densities are defined. The bulk or apparent density represents the mass of the a th constituent per unit volume of the mixture,

$$\rho(\mathbf{x}, t) = \sum_{a=1}^N \rho^{(a)}(\mathbf{x}, t) \quad (3.12)$$

The true density, instead, $\rho_T^{(a)}$ represents the mass of the a th constituent per unit volume of the a th constituent.

The volume fraction of the a th constituent is the volume of the a th constituent per unit volume of mixture,

$$\varphi^{(a)}(\mathbf{x}, t) = \frac{\rho^{(a)}(\mathbf{x}, t)}{\rho_T^{(a)}(\mathbf{x}, t)} \quad (3.13)$$

The volume fractions are subjected to the constraint

$$\sum_{a=1}^N \varphi^{(a)}(\mathbf{x}, t) = 1 \quad (3.14)$$

If the a th constituent is incompressible, its volumetric fraction results constant. The mixture is incompressible when all its constituents are incompressible.

3.1.3 The conservation laws for mixture

The classical balance laws are written for each component of the mixture. The mass conservation law, thus, becomes

$$\frac{\partial \rho^{(a)}}{\partial t} + \nabla \cdot (\rho^{(a)} \mathbf{v}^{(a)}) = 0 \quad (3.15)$$

This equation, summed over all constituents, gives the continuum statement of the mass conservation equation

$$\frac{\partial \rho}{\partial t} + \nabla \cdot (\rho \mathbf{v}) = 0 \quad (3.16)$$

if definitions (3.12) for the density of the continuum mixture and mean mixture velocity \mathbf{v}

$$\mathbf{v} = \frac{1}{\rho} \sum_{a=1}^N \rho^{(a)} \mathbf{v}^{(a)} \quad (3.17)$$

are employed. It is interesting to note that in equation (3.17), the mean velocity is not evaluated as the sum of the velocities of all components but, rather, employing an homogenization approach. Each velocity, in fact, is weighted through the density of the a th component considered.

The conservation of momentum is written as

$$\rho^{(a)} \frac{D^{(a)} \mathbf{v}^{(a)}}{Dt} = \nabla \cdot \boldsymbol{\sigma}^{(a)} + \rho^{(a)} \mathbf{b}^{(a)} + \check{\mathbf{p}}^{(a)} \quad (3.18)$$

where $\boldsymbol{\sigma}^{(a)}$ is the partial stress, $\mathbf{b}^{(a)}$ the action at a distance force density and $\check{\mathbf{p}}^{(a)}$ the momentum supply, representing the transfer of momentum from the other constituents to constituent a . The term $\check{\mathbf{p}}^{(a)}$ does not have a directly associated term in the momentum balance equation written for only one constituent, i.e. $\rho \ddot{\mathbf{u}} = \nabla \cdot \boldsymbol{\sigma} + \rho \mathbf{b}$, where \mathbf{u} is the displacement field. The conservation of energy equation for the mixture becomes

$$\rho^{(a)} \frac{D^{(a)} \hat{\varepsilon}^{(a)}}{Dt} = \boldsymbol{\sigma}^{(a)} : \mathbf{D}^{(a)} - \nabla \cdot \mathbf{q}_h^{(a)} + \rho^{(a)} r^{(a)} + \check{\varepsilon}^{(a)} \quad (3.19)$$

where $\hat{\varepsilon}^{(a)}$ is the partial internal energy density, $\mathbf{q}_h^{(a)}$ is the partial heat flux vector, $r^{(a)}$ is the heat supply density, $\check{\varepsilon}^{(a)}$ is the energy supply and $\mathbf{D}^{(a)} = \frac{1}{2} \left[\mathbf{L}^{(a)} + (\mathbf{L}^{(a)})^T \right]$ is the rate of deformation tensor for the a th constituent. The term $\check{\varepsilon}^{(a)}$ does not have a directly associated term in the energy conservation equation written for only one constituent, i.e. $\rho \dot{\varepsilon} = \mathbf{T} : \mathbf{D} - \nabla \cdot \mathbf{q}_h + \rho r$, and it represents the transfer of energy from the other constituents to constituent a . The summation of equations (3.15), (3.18) and (3.19) over all constituents produce again the single continuum form of these equations. Moreover, a relationship

between the time derivative of the selected component and the sum of the density-weighted time derivatives has been developed, to better interpret the results obtained in the sum operation, such as in the right side of equation (3.19):

$$\bar{\omega} = \frac{1}{\rho} \sum_{a=1}^N \rho^{(a)} \bar{\omega}^{(a)} \quad (3.20)$$

The formula relating the sum of the density-weighted, constituent-specific time derivatives to the time derivative following the selected component is written as

$$\sum_{a=1}^N \rho^{(a)} \frac{D^a \bar{\omega}^{(a)}}{Dt} = \rho \frac{D^s \bar{\omega}}{Dt} - \bar{\omega} \nabla \cdot [\rho (\mathbf{v} - \mathbf{v}_s)] + \sum_{a=1}^N \left(\nabla \cdot [\bar{\omega}^{(a)} \rho^{(a)} \mathbf{v}^{(a)}] \right) \quad (3.21)$$

where $\mathbf{v}^{(a)}$ is the diffusion velocity relative to the selected component:

$$\mathbf{v}^{(a)} = \mathbf{v}^{(a)} - \mathbf{v}^{(s)} \quad (3.22)$$

In equation (3.22), the choice to introduce the diffusion velocity $\mathbf{v}^{(a)}$, defined as the difference between the velocity of the a th component and the velocity of a selected component, is not casual. If the solid matrix of a porous material is considered as the selected component, in fact, the diffusion velocity, $\mathbf{v}^{(a)}$, becomes the driving force of fluid flow in Darcy's law.

From equations (3.22), (3.17) and (3.12), the following equation is evaluated

$$\rho (\mathbf{v} - \mathbf{v}^{(s)}) = \sum_{a=1}^N \rho^{(a)} \mathbf{v}^{(a)} = \sum_{b=1}^{N-s} \rho^{(b)} \mathbf{v}^{(b)} \quad (3.23)$$

because, for the equation (3.22), $\mathbf{v}^{(s)}$ is zero.

Replacing equation (3.23) into equation (3.21), the following relationship is obtained

$$\sum_{a=1}^N \rho^{(a)} \frac{D^a \bar{\omega}^{(a)}}{Dt} = \rho \frac{D^s \bar{\omega}}{Dt} + \sum_{b=1}^{N-s} \left(\nabla \cdot \left[\bar{\omega}_{(b)} \rho^{(b)} \mathbf{v}^{(b)} \right] - \bar{\omega} \nabla \cdot \left[\rho^{(b)} \mathbf{v}^{(b)} \right] \right) \quad (3.24)$$

When $\mathbf{v}^{(s)} = \mathbf{v}$, equation (3.23) reduces to

$$\sum_{a=1}^N \rho^{(a)} \frac{D^a \bar{\omega}^{(a)}}{Dt} = \rho \frac{D \bar{\omega}}{Dt} + \sum_{a=1}^N \left(\nabla \cdot \left[\bar{\omega}^{(a)} \rho^{(a)} \mathbf{v}^{(a)} \right] \right) \quad (3.25)$$

while when $\bar{\omega}^{(a)}$ does not depend on index a

$$\sum_{a=1}^N \rho^{(a)} \frac{D^a \bar{\omega}^{(a)}}{Dt} = \rho \frac{D^s \bar{\omega}}{Dt} + \rho \left(\mathbf{v} - \mathbf{v}^{(s)} \right) \cdot \nabla \bar{\omega} = \rho \frac{D \bar{\omega}}{Dt} \quad (3.26)$$

Employing equation (3.24), it is possible to write the following expression for the velocity $\mathbf{v}^{(a)}$, neglecting the terms of order of diffusion velocity $\mathbf{v}^{(b)}$ squared

$$\sum_{a=1}^N \rho^{(a)} \frac{D^a \mathbf{v}^{(a)}}{Dt} = \rho \frac{D^s \mathbf{v}^{(s)}}{Dt} + \rho \frac{D^s \left(\mathbf{v} - \mathbf{v}^{(s)} \right)}{Dt} + \nabla \cdot \left[\rho \left(\mathbf{v} - \mathbf{v}^{(s)} \right) \otimes \mathbf{v}^{(s)} \right] \quad (3.27)$$

Moreover, it has to be noticed that, from (3.23), the term $\left(\mathbf{v} - \mathbf{v}^{(s)} \right)$ is equal to

$$\frac{1}{\rho} \sum_{b=1}^{N-s} \rho^{(b)} \mathbf{v}^{(b)} \quad (3.28)$$

When the velocity of a component is equal to the mean velocity of the mixture, $\mathbf{v}^{(s)} = \mathbf{v}$, then

$$\sum_{a=1}^N \rho^{(a)} \frac{D^a \mathbf{v}^{(a)}}{Dt} = \rho \frac{D\mathbf{v}}{Dt} \quad (3.29)$$

With equations (3.24) and (3.27), the summation of the balance equations of the mixture can be evaluated to compare them to the single continuum balance equations.

Summation of the component specific form of conservation of linear momentum, (3.18), employing equation (3.27), yields an equation similar to the continuum one

$$\begin{aligned} \frac{D^s \mathbf{v}^{(s)}}{Dt} + \rho \frac{\partial (\mathbf{v} - \mathbf{v}^{(s)})}{Dt} - (\mathbf{v} - \mathbf{v}^{(s)}) \nabla \cdot \left\{ \rho (\mathbf{v} - \mathbf{v}^{(s)}) \right\} + \\ + \rho \nabla \cdot \left[\mathbf{v}^{(s)} \otimes (\mathbf{v} - \mathbf{v}^{(s)}) \right] = \nabla \cdot \boldsymbol{\sigma} + \rho \mathbf{b} \end{aligned} \quad (3.30)$$

or, if $\mathbf{v}^{(s)} = \mathbf{v}$,

$$\rho \frac{D\mathbf{v}}{Dt} = \nabla \cdot \boldsymbol{\sigma} + \rho \mathbf{b} \quad (3.31)$$

If $\mathbf{v}^{(s)} = \mathbf{v}$, or $\mathbf{v}^{(s)} \neq \mathbf{v}$, the total stress $\boldsymbol{\sigma}$ is defined, neglecting the terms of order of diffusion velocity $\mathbf{v}^{(b)}$ squared, as

$$\boldsymbol{\sigma} = \sum_{a=1}^N \boldsymbol{\sigma}^{(a)} \quad (3.32)$$

while the sum of the action at a distance forces is

$$\mathbf{b} = \frac{1}{\rho} \sum_{a=1}^N \left(\rho^{(a)} \mathbf{b}^{(a)} \right) \quad (3.33)$$

The constituent momentum supply $\check{\mathbf{p}}^{(a)}$ is subjected to the following constraint

$$\sum_{a=1}^N \check{\mathbf{p}}^{(a)} = 0 \quad (3.34)$$

The summation of balance of energy equation for each constituent, (3.19), employing the relationship (3.21) with $\bar{\omega}^{(a)}$ replaced with $\varepsilon^{(a)}$, is

$$\rho \frac{D^s \hat{\varepsilon}}{Dt} = \rho r + \sum_{a=1}^N \left\{ \boldsymbol{\sigma}^{(a)} : \mathbf{D}^{(a)} - \mathbf{v}^{(a)} \check{\mathbf{p}}^{(a)} - \nabla \cdot \left[\mathbf{q}_h^{(a)} + \check{\varepsilon}^{(a)} \rho^{(a)} \mathbf{v}^{(a)} \right] \right\} \quad (3.35)$$

where the specific internal energy density, $\hat{\varepsilon}$, and the heat supply density, r , are defined as

$$\hat{\varepsilon} = \frac{1}{\rho} \sum_{a=1}^N \rho^{(a)} \hat{\varepsilon}^{(a)}, \quad r = \frac{1}{\rho} \sum_{a=1}^N \rho^{(a)} r^{(a)} \quad (3.36)$$

and the energy supply, $\check{\varepsilon}^{(a)}$, is subjected to the following constraint

$$\sum_{a=1}^N \left\{ \check{\varepsilon}^{(a)} + \mathbf{v}^{(a)} \check{\mathbf{p}}^{(a)} + \hat{\varepsilon} \nabla \cdot \left[\rho^{(a)} \mathbf{v}^{(a)} \right] \right\} = 0 \quad (3.37)$$

3.2 Biphasic Theory

3.2.1 Introduction

Biphasic theory is a simplification of mixture theory, characterized by the presence of only two phases, the solid and the fluid. The solid can shrink only by expelling the fluid into its surroundings, or swell only by attracting the fluid from its surroundings. In the biphasic theory, conservation and balance equations are written separately for the two phases and, then, combined to describe the whole mixture, introducing a new term which takes into account the interaction, or exchange of mass or momentum, between the particular constituent and all other mixture constituents. The biphasic theory is a very important instrument to describe soft, hydrated biological tissues, such as articular cartilage, fibrocartilages (the meniscus, temporomandibular joint disc and intervertebral disc), and even cells. In the biphasic theory, the material is modeled as a porous solid, indicated with the apex s , saturated with a fluid, denoted by f . The material behavior is described by a set of coupled equations: balance equations and constitutive equations. Biphasic theory needs, first of all, some definitions. If an infinitesimal volume dV is considered, constituted by a fluid volume dV^f with mass dm^f and a solid volume dV^s with mass dm^s , two densities can be defined. The true density of each component is

$$\rho_T^f = \frac{dm^f}{dV^f} \quad \rho_T^s = \frac{dm^s}{dV^s} \quad (3.38)$$

while the apparent density is defined as

$$\rho^f = \frac{dm^f}{dV} \quad \rho^s = \frac{dm^s}{dV} \quad (3.39)$$

Employing the equations (3.38) and (3.39), the volumetric fractions are introduced

$$\varphi^f = \frac{dV^f}{dV} = \frac{\rho^f}{\rho_T^f} \quad \varphi^s = \frac{dV^s}{dV} = \frac{\rho^s}{\rho_T^s} \quad (3.40)$$

φ^f is also indicated as the porosity of the material.

The following constraint subsists for the volumetric fractions

$$\varphi^f + \varphi^s = 1 \quad (3.41)$$

3.2.2 Balance equations

The balance equations, as highlighted before, are written separately for the solid and fluid phases. In general, the continuity equation, neglecting generation terms, for the fluid is

$$\rho^f (\nabla \cdot \mathbf{v}^f) + \frac{D\rho^f}{Dt} = 0 \quad (3.42)$$

while, for the solid phase

$$\rho^s (\nabla \cdot \mathbf{v}^s) + \frac{D\rho^s}{Dt} = 0 \quad (3.43)$$

If the fluid and solid phases are both intrinsically incompressible, the true densities result constant and, so, by replacing equation (3.40) in the equations (3.42) and (3.43), the continuity equations become

$$\begin{aligned} \frac{\partial \varphi^f}{\partial t} + \nabla \cdot (\varphi^f \mathbf{v}^f) &= 0 \\ \frac{\partial \varphi^s}{\partial t} + \nabla \cdot (\varphi^s \mathbf{v}^s) &= 0 \end{aligned} \quad (3.44)$$

The continuity equation for the whole biphasic system is obtained summing the continuity equations for the two phases, (3.44), and remembering that $\varphi^f + \varphi^s = 1$:

$$\nabla \cdot (\varphi^f \mathbf{v}^f + \varphi^s \mathbf{v}^s) = 0 \quad (3.45)$$

Analogously, the momentum equations for the fluid and solid phases are

$$\begin{aligned}\nabla \cdot \boldsymbol{\sigma}^f + (\rho^f \mathbf{b}^f + \mathbf{m}^f) &= \rho^f \ddot{\mathbf{u}}^f \\ \nabla \cdot \boldsymbol{\sigma}^s + (\rho^s \mathbf{b}^s + \mathbf{m}^s) &= \rho^s \ddot{\mathbf{u}}^s\end{aligned}\quad (3.46)$$

where $\boldsymbol{\sigma}^f$ and $\boldsymbol{\sigma}^s$ are the stress tensor for the fluid and the solid, respectively, \mathbf{b}^f and \mathbf{b}^s are the sum of the external body forces for the two phases, \mathbf{m}^f and \mathbf{m}^s describe the internal body forces reflecting the interactions between the fluid and the solid and $\ddot{\mathbf{u}}^f$ and $\ddot{\mathbf{u}}^s$ are accelerations. Summing the equations (3.46), the following relationship is obtained

$$\nabla \cdot (\boldsymbol{\sigma}^f + \boldsymbol{\sigma}^s) + (\rho^f \mathbf{b}^f + \rho^s \mathbf{b}^s) + (\mathbf{m}^f + \mathbf{m}^s) = (\rho^f \ddot{\mathbf{u}}^f + \rho^s \ddot{\mathbf{u}}^s) \quad (3.47)$$

Employing Truesdell's second principle, the following relations subsists

$$\begin{aligned}\rho \mathbf{b} &= (\rho^f \mathbf{b}^f + \rho^s \mathbf{b}^s) + (\mathbf{m}^f + \mathbf{m}^s) \\ \rho \ddot{\mathbf{u}} &= (\rho^f \ddot{\mathbf{u}}^f + \rho^s \ddot{\mathbf{u}}^s)\end{aligned}\quad (3.48)$$

Equations (3.48) underline that the total body force acting on the biphasic system is the weighted sum of the external forces acting on each phase plus the contribution of the interaction terms. Moreover, also the overall acceleration is the weighted sum of the acceleration of the two phases. In the hypothesis of quasi-static equilibrium, for the biphasic system, the following constraint subsists

$$\mathbf{m}^f + \mathbf{m}^s = 0 \quad (3.49)$$

Neglecting external body forces and employing the equation (3.49), equations (3.46) become

$$\begin{aligned}\nabla \cdot \boldsymbol{\sigma}^f + \mathbf{m}^f &= 0 \\ \nabla \cdot \boldsymbol{\sigma}^s + \mathbf{m}^s &= 0\end{aligned}\quad (3.50)$$

Equations (3.50) assume different forms according to the constitutive equations chosen to model the fluid and the solid phase and the kind of interaction between them. For biological soft tissues, Mow et al. (Mow et al., 1980) considered as interaction force a viscous drag force directly proportional to the relative velocity between the two phases. In these hypotheses \mathbf{m}^f and \mathbf{m}^s become

$$\begin{aligned}\mathbf{m}^f &= \eta(\mathbf{v}^s - \mathbf{v}^f) \\ \mathbf{m}^s &= -\mathbf{m}^f = \eta(\mathbf{v}^f - \mathbf{v}^s)\end{aligned}\quad (3.51)$$

where η is the coefficient of diffusive resistance $[Ns/m^4]$ and it is related to the permeability by the following relationship

$$\eta = \frac{(\phi^f)^2}{k}, \quad k = \frac{\kappa}{\mu_{fluid}}\quad (3.52)$$

Replacing equations (3.51) in the equations (3.50), the momentum equations become

$$\begin{aligned}\nabla \cdot \boldsymbol{\sigma}^f + \eta(\mathbf{v}^s - \mathbf{v}^f) &= 0 \\ \nabla \cdot \boldsymbol{\sigma}^s + \eta(\mathbf{v}^f - \mathbf{v}^s) &= 0\end{aligned}\quad (3.53)$$

3.2.3 Constitutive equations

The constitutive equations obviously change according to the different kinds of material which constitute the biphasic system. If the fluid is inviscid and the solid matrix is supposed to be isotropic, then the constitutive equations for the two phases are

$$\begin{aligned}\boldsymbol{\sigma}^f &= -\varphi^f p \mathbf{I} \\ \boldsymbol{\sigma}^s &= -\varphi^s p \mathbf{I} + \lambda_{solid} e \mathbf{I} + 2\mu_{solid} \boldsymbol{\varepsilon}\end{aligned}\quad (3.54)$$

where p is the hydrostatic pressure, e is the trace of the strain tensor and λ_{solid} and μ_{solid} are the Lamé's constant of the solid matrix.

Replacing equations (3.54) in the equations (3.53), the equations of motion for the biphasic system is obtained, in the hypothesis of inviscid fluid and isotropic solid matrix

$$\begin{aligned}-\nabla(\varphi^f p) + \eta(\mathbf{v}^s - \mathbf{v}^f) &= 0 \\ -\nabla(\varphi^s p) + \lambda_{solid} \nabla e + 2\mu_{solid} \nabla \cdot \boldsymbol{\varepsilon} + \eta(\mathbf{v}^f - \mathbf{v}^s) &= 0\end{aligned}\quad (3.55)$$

3.2.4 Confined Compression

Confined compression is an idealized deformation configuration in which a tissue specimen is placed into a chamber that confines the specimen at the bottom and on the sides. A porous platen, which allows fluid to exit through the specimen's surface, is used to compress the sample. The purpose of this section is to illustrate the solution of the differential equation which governs the cartilage behavior under a confined compression test (Soltz and Athesian, 1998). The confined compression chamber is schematized in Figure 3.2.

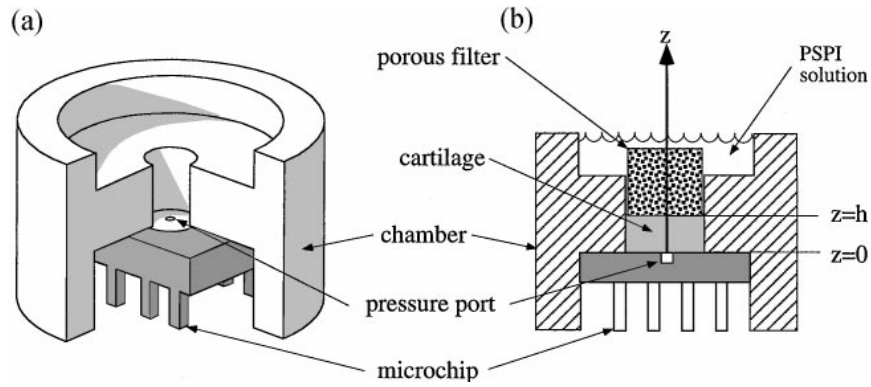


Figure 3.2

- (a) Schematic of confined compression chamber with microchip transducer shown bonded to the chamber.
- (b) Cross-section of chamber, indicating the direction of the z -coordinate axis. The articular surface of the cartilage specimen faces the pressure port.

The displacement at the top surface is ramped at the rate V_0 until the time t_0 (corresponding to the attainment of an engineering strain of 10%) and then held constant. If z is the direction of loading, the displacement of the solid matrix depends, exclusively, on z and t . Under these conditions,

$$\begin{aligned} u_x = u_y &= 0 \\ u_z &= u_z(z, t) \end{aligned} \quad (3.56)$$

and, so, the strain tensor becomes

$$\boldsymbol{\varepsilon} = \begin{bmatrix} 0 & 0 & 0 \\ 0 & 0 & 0 \\ 0 & 0 & \frac{\partial u_z}{\partial z} \end{bmatrix} \quad (3.57)$$

The governing equation for confined compression, derived from the general equations of the linear biphasic theory for isotropic homogeneous materials, is (Mow et al., 1980)

$$\frac{\partial^2 u_z}{\partial z^2} = \frac{1}{H_a k} \frac{\partial u_z}{\partial t} \quad (3.58)$$

where $H_a = (\lambda_{solid} + 2\mu_{solid})$ is the aggregate modulus [Pa] and k is the hydraulic conductivity. The initial condition is

$$u_z(z, 0) = 0 \quad (3.59)$$

The boundary condition at the bottom, impermeable surface is

$$u_z(0, t) = 0 \quad (3.60)$$

while, for the stress relaxation, the boundary condition at the top surface is

$$u_z(h, t) = \begin{cases} -V_0 t, & 0 \leq t \leq t_0 \\ -V_0 t_0, & t \geq t_0 \end{cases} \quad (3.61)$$

The solution, obtained using standard methods for partial differential equations, is

$$u_z(z, t) = \begin{cases} -\frac{V_0 t z}{h} - \frac{2V_0 h^2}{\pi^3 H_a k} \sum_{n=1}^{\infty} \frac{(-1)^n}{n^3} \left(1 - e^{-n^2 \cdot \pi^2 \cdot H_a \cdot kt/h^2}\right) \cdot \text{sen}\left(\frac{n\pi z}{h}\right) \\ \text{for } 0 \leq t \leq t_0 \\ -\frac{V_0 t_0 z}{h} - \frac{2V_0 h^2}{\pi^3 H_a k} \sum_{n=1}^{\infty} \frac{(-1)^n}{n^3} e^{-n^2 \cdot \pi^2 \cdot H_a \cdot kt/h^2} \left(e^{n^2 \cdot \pi^2 \cdot H_a \cdot kt_0/h^2} - 1\right) \cdot \text{sen}\left(\frac{n\pi z}{h}\right) \\ \text{for } t \geq t_0 \end{cases} \quad (3.62)$$

CHAPTER IV

POROELASTICITY – THERMOELASTICITY DUALITY

(PTD)

4.1 Introduction

The equations of poroelasticity and thermoelasticity are very similar to one another (Zimmerman, 2000) and this correspondence could be a powerful tool to solve poroelastic problems. The basilar concept of the coupling between poroelasticity and thermoelasticity is that the temperature and the pore pressure play similar roles. In both theories, in fact, the basic constitutive equations relating the stresses and strains are the same of those of standard elasticity, in which some multiple of the pore pressure (or temperature) is subtracted from the normal stresses. Moreover, considering the typical values of these multiple coefficients arising in most rock mechanics applications, both theories are at least partially coupled, that is to say that variations in the pore pressure (or temperature) will appreciably influence the stresses and strains. The pore pressure and temperature are described through diffusion equations, which contain a source-sink type term depending on the time derivative of the bulk strain or mean normal stress. The analogy between the two theories, then, arises from the identical formal structure of the equations governing the two problems, which allows to find a direct relationship between each parameter appearing in the two theories. The strength of the coupling between the mechanical variables, stress and strain, and the pore pressure (or temperature), can be estimated in terms of dimensionless coupling parameters, as shown in the following. However, an analysis of the typical values for these coupling coefficients shows that the poroelastic coupling effect is usually strong (for a liquid-saturated rock), while the thermoelastic coupling effect is usually negligible. This result means that the temperature distribution is not affected by the stresses and strains, whereas this is not usually the case for the pore pressure equation. Finally, Zimmerman (Zimmerman, 2000) emphasized also the existence of other types of thermoelastic couplings, such as the dependence of the constitutive coefficients from stress. The permeability of many fractured rocks, for example, is highly stress-dependent

and so, the permeability will be influenced by stress, causing an alteration of the flow field, and, thereby, changes in the pore pressure distribution. Moreover, Zimmerman (Zimmerman, 2000) underlined also the importance of modeling non-isothermal poroelasticity, characterized by the influence of temperature on stresses, through the following mechanism. An increase in temperature may lead to a large increase in fluid pressure (because this particular coupling is typically large in liquids), which, in turn, will determine mechanical stresses and strains. In this situation, indeed, there will be a coupling between the temperature and the stress and strain fields. Within the framework of the analogy between poroelasticity and thermoelasticity, a possible strategy to implement a poroelastic problem with a FE code, thus, consists in exploiting this analogy. Since the equations describing the two problems are identical in formal structure, they can be rewritten to draw a direct relationship between each parameter appearing in the two theories.

4.2 Coupled non - linear poroelastic problem

The fundamental equations for a poroelastic problem \mathbf{P} can be summarized as follows

$$\begin{aligned} P_1 : \rho \ddot{\mathbf{u}} - \nabla \cdot [\mathbb{C} : \boldsymbol{\varepsilon} - p \mathbf{I}] &= \rho \mathbf{f} \\ P_2 : \mathbf{I} : \mathbf{I} \dot{\boldsymbol{\varepsilon}} + M^{-1} \dot{p} - \nabla \cdot [(\rho_{f0} \mathbf{g})^{-1} \mathbf{K} \cdot \nabla p] &= 0 \end{aligned} \quad (4.1)$$

The field variables involved are the displacement, $\mathbf{u} = \mathbf{u}(\mathbf{x}, t)$, the bulk strain, $\boldsymbol{\varepsilon} = \text{sym} \nabla \otimes \mathbf{u}$, and the pore fluid pressure, $p = p(\mathbf{x}, t)$. In the first equation (4.1), $\rho = \rho_s (1 - \phi) + \rho_f \phi$ is the density, \mathbb{C} is the stiffness fourth-order tensor, \mathbf{I} is the second order unit tensor (The Biot tensor is \mathbf{I} for saturated porous media) and \mathbf{f} is the mass force vector. In the second equation, instead, the term $\mathbf{I} : \mathbf{I} \dot{\boldsymbol{\varepsilon}}$ can be expressed as $\dot{e} := \nabla \cdot \dot{\mathbf{u}}$ and $(\rho_{f0} \mathbf{g})^{-1} \mathbf{K} \cdot \nabla p$ is the filtration velocity vector (Darcy quasi-static approximation law). This vector depends on the second rank tensor of the filtration coefficients \mathbf{K} , which is linked, in turn, to the second rank permeability tensor, \mathbf{K}_p , the initial fluid density, ρ_{f0} ,

the gravitation acceleration, \mathbf{g} , and the fluid viscosity, μ , as shown in the following equation:

$$\mathbf{K} = \frac{\mathbf{K}_p \rho_f \mathbf{g}}{\mu} \quad (4.2)$$

The coefficient M is expressed as $M^{-1} = N^{-1} + K_f^{-1} \phi$, where N^{-1} is the reverse Biot's modulus, K_f is the fluid tangent bulk modulus and ϕ is the porosity. The change in porosity is directly related to the change in pression by the following relationship:

$$(\phi - \phi_0) = \mathbf{I} : \boldsymbol{\varepsilon} + N^{-1} (p - p_0) \quad (4.3)$$

The equations (4.1) are determined starting from the Constitutive Equations:

$$\begin{aligned} \boldsymbol{\sigma} &= \mathbb{C} : \boldsymbol{\varepsilon} - p \mathbf{I} \\ \phi &= \mathbf{I} : \boldsymbol{\varepsilon} + N^{-1} p \quad [\mathbf{I} \leftarrow \mathbf{b}] \end{aligned} \quad (4.4)$$

and the Darcy's Law (quasi-static filtration)

$$\mathbf{v}_f = \frac{\mathbf{K}_p}{\mu} \nabla p \quad (4.5)$$

where \mathbf{v}_f , the difference between the fluid velocity and the solid matrix one, is responsible of the coupling.

The first equation (4.1) is obtained from the equilibrium equation

$$\rho \ddot{\mathbf{u}} - \nabla \cdot \boldsymbol{\sigma} = \rho \mathbf{f} \quad (4.6)$$

while the second one from the continuity equation

$$\frac{\partial \rho_f \phi}{\partial t} + \nabla \cdot (\rho_f \mathbf{v}_f) = 0 \quad (4.7)$$

4.3 Coupled non - linear thermoelastic problem

The fundamental equations for a thermoelastic problem T can be summarized as follows

$$\begin{aligned} T_1 : \rho \ddot{\mathbf{u}} - \nabla \cdot [\mathbb{C} : \boldsymbol{\varepsilon} - \boldsymbol{\beta} \theta] &= \rho \mathbf{f} \\ T_2 : T_0 \boldsymbol{\beta} : \dot{\boldsymbol{\varepsilon}} + \rho c_\varepsilon \dot{\theta} - \nabla \cdot [\mathbf{K}_T \cdot \nabla \theta] &= W \end{aligned} \quad (4.8)$$

The field variables involved are the displacement, $\mathbf{u} = \mathbf{u}(\mathbf{x}, t)$, the bulk strain, $\boldsymbol{\varepsilon} = \text{sym} \nabla \otimes \mathbf{u}$, and the temperature, $\theta = \theta(\mathbf{x}, t)$. In the first equation (4.8), ρ is the density, \mathbb{C} is the fourth order stiffness tensor, $\boldsymbol{\beta} = \mathbb{C} : \boldsymbol{\alpha}$ is the second order “thermal stresses” tensor, $\boldsymbol{\alpha}$ is the second order tensor of thermal expansion and \mathbf{f} is the mass force vector. In the second equation, instead, T_0 is the reference temperature ($T_0 = 1K$) from which θ is measured and c_ε is the specific heat under constant strain and it can be expressed as

$$c_\varepsilon = c_\sigma - \frac{T_0}{\rho} \boldsymbol{\alpha} : \boldsymbol{\beta} \quad (4.9)$$

where c_σ is the heat capacity at constant pressure.

$\mathbf{K}_T \cdot \nabla \theta$ represents the heat flow vector and \mathbf{K}_T is the second rank tensor of thermal conductivity coefficients. Finally, W is the heat source intensity.

The equations (4.8) are determined starting from the Constitutive Equations:

$$\begin{aligned}\mathbf{T} &= \mathbb{C} : \boldsymbol{\varepsilon} - \boldsymbol{\beta}\theta \\ \mathbf{S} &= \boldsymbol{\beta} : \boldsymbol{\varepsilon} + \frac{\rho c_{\varepsilon}}{T_0} \theta\end{aligned}\quad (4.10)$$

The first equation (4.8) is obtained from the equilibrium equation

$$\rho \ddot{\mathbf{u}} - \nabla \cdot \boldsymbol{\sigma} = \rho \mathbf{f} \quad (4.11)$$

while the second one from the heat flow equation

$$T_0 \cdot \dot{S}_{ent} + \nabla \cdot \mathbf{h} = W \quad (4.12)$$

where S_{ent} is the entropy density and \mathbf{h} is the heat flow vector, expressed as

$$\mathbf{h} = -\mathbf{K}_T \cdot \nabla \theta \quad (4.13)$$

\mathbf{h} is responsible of the coupling.

The heat flow equation represents the energy balance from the second thermodynamical principle.

4.4 Coupling between poroelasticity and thermoelasticity

As shown in Table 4.1, the fundamental equations for coupled non linear poroelasticity and thermoelasticity are formally very similar.

P	T
$\rho \ddot{\mathbf{u}} - \nabla \cdot [\mathbf{C} : \boldsymbol{\varepsilon} - p \mathbf{I}] = \rho \mathbf{f}$	$\rho \ddot{\mathbf{u}} - \nabla \cdot [\mathbf{C} : \boldsymbol{\varepsilon} - \boldsymbol{\beta} \theta] = \rho \mathbf{f}$
$\mathbf{I} : \dot{\boldsymbol{\varepsilon}} + M^{-1} \dot{p} - \nabla \cdot \left[(\rho_{f0} \mathbf{g})^{-1} \mathbf{K} \cdot \nabla p \right] = 0$	$T_0 \boldsymbol{\beta} : \dot{\boldsymbol{\varepsilon}} + \rho c_\varepsilon \dot{\theta} - \nabla \cdot [\mathbf{K}_T \cdot \nabla \theta] = 0$

Table 4.1

Fundamental equations for coupled non linear poroelasticity and thermoelasticity

The objective of this work is to solve poroelastic problems performing thermal analysis. For that purpose, it is necessary to find the connection between the parameters of both theories. The conversion factors introduced to write a poroelastic problem as a thermal one are:

$$\begin{aligned}
 p &\leftrightarrow \theta; \\
 \mathbf{I} &\leftrightarrow \boldsymbol{\beta}; \\
 \frac{T_0}{\rho M} &\leftrightarrow c_\varepsilon; \\
 \frac{T_0}{\mu} \mathbf{K}_p &\leftrightarrow \mathbf{K}_T
 \end{aligned} \tag{4.14}$$

Nevertheless, the parameters of the two theories involved in the duality relationships (4.14) have very different order of magnitude, which could cause some problems during the solution of the numerical simulations. For these reasons, the following step consists in the introduction of dimensionless parameters in the fundamental equations written before. Table 4.2 shows the fundamental equations for coupled non linear poroelasticity and thermoelasticity rewritten in terms of the dimensionless parameters. The symbol \sim in the equations indicates the dimensionless parameters.

P^*	T^*
$\tilde{\rho} \frac{\partial^2 \tilde{\mathbf{u}}}{\partial \tilde{t}^2} - \tilde{\nabla} \cdot [\tilde{\mathbf{C}} : \boldsymbol{\varepsilon} - \mathbf{I} \tilde{p}] = \tilde{\rho} \tilde{\mathbf{f}}$	$\tilde{\rho} \frac{\partial^2 \tilde{\mathbf{u}}}{\partial \tilde{t}^2} - \tilde{\nabla} \cdot [\tilde{\mathbf{C}} : \boldsymbol{\varepsilon} - \tilde{\boldsymbol{\beta}} \tilde{\theta}] = \tilde{\rho} \tilde{\mathbf{f}}$
$T_0 \mathbf{I} : \frac{\partial \tilde{\boldsymbol{\varepsilon}}}{\partial \tilde{t}} + \tilde{\rho} \tilde{c}_p \frac{\partial \tilde{p}}{\partial \tilde{t}} - \tilde{\nabla} \cdot [\tilde{\mathbf{K}} \cdot \nabla \tilde{p}] = 0$	$T_0 \tilde{\boldsymbol{\beta}} : \frac{\partial \tilde{\boldsymbol{\varepsilon}}}{\partial \tilde{t}} + \tilde{\rho} \tilde{c}_\varepsilon \frac{\partial \tilde{\theta}}{\partial \tilde{t}} - \tilde{\nabla} \cdot [\tilde{\mathbf{K}}_T \cdot \tilde{\nabla} \tilde{\theta}] = 0$

Table 4.2

Fundamental equations for coupled non linear poroelasticity and thermoelasticity rewritten in terms of the dimensionless parameters

These equation are written employing the following positions:

$$\begin{aligned}
 \tilde{\mathbf{x}} &= \mathbf{x} L^{-1}; & \tilde{\mathbf{u}} &= \mathbf{u} L^{-1}; & \tilde{\nabla} &= L \nabla; & \tilde{t} &= T^{-1} t; & \tilde{\mathbf{C}} &= P^{-1} \mathbf{C}; \\
 \tilde{\boldsymbol{\sigma}} &= \boldsymbol{\sigma} P^{-1}; & \tilde{\theta} &= \theta; & \tilde{p} &= p P^{-1}; & \tilde{\rho} &= L^2 T^{-2} P^{-1} \rho; \\
 \tilde{\mathbf{f}} &= T^2 L^{-1} \mathbf{f}; & \tilde{c}_p &= T_0 P M^{-1} \tilde{\rho}^{-1}; & \tilde{\mathbf{K}} &= T_0 P T L^{-2} \mathbf{K}_p \mu^{-1}; \\
 \tilde{\mathbf{h}} &= -\mathbf{K}_T \cdot \tilde{\nabla} \tilde{\theta} \leftrightarrow \tilde{\mathbf{v}}_f = -\tilde{\mathbf{K}} \cdot \tilde{\nabla} \tilde{p} = -\frac{\mathbf{K}_p}{\mu} \nabla p T_0 T L^{-1} = T_0 T L^{-1} \mathbf{v}_f
 \end{aligned} \tag{4.15}$$

The dimensionless conversion factors are:

$$\begin{aligned}
 \tilde{p} &\leftrightarrow \tilde{\theta}; & \mathbf{I} &\leftrightarrow \tilde{\boldsymbol{\beta}} = \tilde{\mathbf{C}} : \boldsymbol{\alpha} = P^{-1} \mathbf{C} : \boldsymbol{\alpha}; \\
 \tilde{c}_p &\leftrightarrow \tilde{c}_\varepsilon = c_\varepsilon T^2 L^{-2}; & \tilde{\mathbf{K}} &\leftrightarrow \tilde{\mathbf{K}}_T = \frac{T}{L^2 P} \mathbf{K}_T
 \end{aligned} \tag{4.16}$$

where $\alpha = \frac{1-2\nu}{E}$, L is an enveloping parameter, that is to say the characteristic length of the domain and

$$\begin{aligned}
 P &:= p_{MAX} = \max_{\underline{x}, t} \{p\}; \\
 T &:= t_{MAX} = \max_{\mathbb{R}^+} \{t\};
 \end{aligned} \tag{4.17}$$

The dimensionless conversion factors are evaluated referring to the maximum values of length, pressure and time to ensure reasonable values of the parameters involved in the numerical simulations. Employing the coupling theory presented before, it is possible to solve a transient non linear poroelastic problem as a corresponding thermoelastic problem, interpreting the temperature as a pressure and the temperature gradient as a velocity.

4.5 On the influence of coupling terms in poroelasticity and thermoelasticity

The pore pressure always has an appreciable influence on the deformation field and, so, the equations of linear poroelasticity are always partially coupled (Zimmerman, 2000). The solution of a coupled poroelastic or thermoelastic problem is of considerable mathematical difficulty, as it combines the theories of elasticity and of heat conduction or fluid flow under transient conditions. Fortunately, in most of the usual engineering applications it is possible to introduce certain simplifying assumptions without error. The principal such simplifications are the omission of the mechanical coupling term in the energy equation (*uncoupled theory*) and of the inertia terms in the equations of motion (*uncoupled quasi-static theory*). To this purpose, Boley and Weiner (Boley and Weiner, 1997) investigated the conditions ensuring that a linear thermoelastic problem can be considered uncoupled or uncoupled quasi-static. In the following, this reasoning is presented and, then, it will be extended to the poroelasticity theory, employing the PTD theory presented before. In the thermoelastic problem, if an external mechanical agency produces variations of strain within a body, the heat conduction equation shows that these variations of strain are, in general, accompanied by variations in temperature and consequently by a heat flow; the whole process, thus, gives rise to an increase of entropy and, therefore, to an increase in the energy stored in a mechanically irrecoverable manner. This phenomenon, known as thermoelastic dissipation, requires for its analysis the use of the coupled heat equation. The mechanical term in the heat equation clearly plays a crucial role in the description of this dissipative process, and its omission would here be meaningless. However, the deformations due to the external loads are accompanied only by small changes in temperature, and it would, therefore, appear reasonable to calculate these deformation

without taking account of the thermal expansion. Similarly, if strain are produced in a body by a non-uniform temperature distribution, it would seem intuitively clear that the influence of these strains on the temperature itself should not be too large. One may therefore anticipate the conclusion that the coupling term appearing in the heat equation can be disregarded for all problem except those in which the thermoelastic dissipation is of primary interest. This matter may be made plausible by the following reasoning. The coupled heat equation may be rewritten as

$$K_T \Delta T = \rho c_v \dot{T} \left[1 + \delta \left(\frac{\lambda + 2\mu}{3\lambda + 2\mu} \right) \left(\frac{\dot{\epsilon}}{\alpha \dot{T}} \right) \right] \quad (4.18)$$

where c_v , the specific heat at constant volume, and c_ϵ , the specific heat at constant deformation, may be employed interchangeably in the linear theory. The non-dimensional parameter δ is defined by

$$\delta = \frac{(3\lambda + 2\mu)^2 \alpha^2 T_0}{\rho^2 c_v v_e^2} \quad (4.19)$$

v_e is the velocity of propagation of dilatational waves in an elastic medium, defined as

$$v_e = \sqrt{(\lambda + 2\mu)/\rho} \quad (4.20)$$

The term proportional to δ is the coupling term, and it is negligible compared to unity if

$$\frac{\dot{\epsilon}}{3\alpha \dot{T}} \ll \left(\frac{\lambda + 2\mu/3}{\lambda + 2\mu} \right) \frac{1}{\delta} \quad (4.21)$$

Equation (4.21) furnishes a comparison between an external factor, $\frac{\dot{\epsilon}}{3\alpha \dot{T}}$, directly linked to the thermal-mechanical input, and the intrinsic thermo-mechanical properties of the

material, $\left(\frac{\lambda+2\mu/3}{\lambda+2\mu}\right)\frac{1}{\delta}$. To estimate a priori if the problem is uncoupled, both terms of equation (4.21) need to be evaluated. As already said, the term $\left(\frac{\lambda+2\mu/3}{\lambda+2\mu}\right)\frac{1}{\delta}$ depends on thermal, physical and mechanical parameters and, so, it can be determined a priori for the analyzed problem. For what concerns, instead, the other term, $\frac{\dot{\epsilon}}{3\alpha\dot{T}}$, even if it is associated to the thermo-mechanical output, it can be estimated from the thermal-mechanical input. This term, in fact, represents the ratio between two deformation rates. In the hypothesis of linear thermoelastic theory, $\dot{\epsilon}$ can be decomposed in the sum of two contributions, i.e., $\dot{\epsilon} = \dot{\epsilon}^{el} + \dot{\epsilon}^t$, where $\dot{\epsilon}^{el}$ is the elastic deformation rate, depending on the constitutive behavior of the material, and $\dot{\epsilon}^t$ is, instead, the thermal deformation rate, expressed as $3\alpha\dot{T}$. Equation (4.21) can be, thus, rewritten as

$$\frac{\dot{\epsilon}^{el} + \dot{\epsilon}^t}{\dot{\epsilon}^t} \ll \left(\frac{\lambda+2\mu/3}{\lambda+2\mu}\right)\frac{1}{\delta} \quad (4.22)$$

The order of magnitude of the elastic deformation rate, $\dot{\epsilon}^{el}$, can be estimated starting from the loading conditions, while, for the thermal deformation rate, $\dot{\epsilon}^t$, an estimate can be made considering the boundary conditions on temperature or on its flux. For temperature distributions with no sharp variation or discontinuities in their time histories, it is intuitively expected that the time rate of change of the dilatation is of the same order of magnitude as that of the temperature; thus, the disregarded of coupling as described previously appears to be reasonable. The preceding discussion makes it clear that the possibility of omitting the coupling terms depends not only on the fact that the inequality $\delta \ll 1$ must hold (as it does for most metals), but also on the fact that strain rates must be of the same order of magnitude as the temperature rate. The latter condition implies that the time history of the displacement closely follows that of the temperature; in other words, no pronounced lag or vibrations in the motion of the body must arise. It is, therefore, to be expected that the magnitude of inertia effects will also enter this question, so that a close relationship can be anticipated to exist between the two previously mentioned simplifications of the general theory. Starting from equation (4.21), it is possible to extend

the same considerations to the poroelasticity theory. The second equation (4.1) can be written as

$$\frac{K_p}{\mu} \Delta p - \frac{1}{M} \dot{p} - \dot{\epsilon} = 0 \quad (4.23)$$

and, then, rearranged in the following form:

$$\frac{K_p}{\mu} \Delta p - \frac{1}{M} \dot{p} \left[1 + \frac{\dot{\epsilon}}{\dot{p}} M \right] = 0 \quad (4.24)$$

Following the approach proposed by Boley and Weiner (Boley and Weiner, 1997), a poroelastic problem results, thus, uncoupled if the following inequality holds

$$\frac{\dot{\epsilon}}{\dot{p}} \ll \frac{1}{M} \quad (4.25)$$

However, the simple form of equation (4.25) hides some interesting aspects. To ensure that a poroelastic problem is uncoupled, it is not sufficient that $\frac{1}{M}$ is very small, but, paradoxically, it should also happen that $\frac{\dot{\epsilon}}{\dot{p}} \ll \frac{1}{M}$. Also in this case, an evaluation a priori of the two terms appearing in the equation (4.25) is necessary. The term $\frac{1}{M}$ is strictly connected to the physical poroelastic properties of the material and, thus, it can be easily evaluated a priori. Iterating the previous reasoning for the linear thermoelastic problem, the term associated to the poroelastic-mechanical output, $\frac{\dot{\epsilon}}{\dot{p}}$, can be estimated starting from the order of magnitude of the loading and boundary conditions. Nevertheless, even if $\frac{\dot{\epsilon}}{\dot{p}} M \cong 1$, the problem could result uncoupled. The term $\left[1 + \frac{\dot{\epsilon}}{\dot{p}} M \right]$ becomes, in fact, equal to 2; if $\frac{1}{M} \dot{p} \ll \frac{K_p}{\mu} \Delta p$, the poroelastic problem becomes not only uncoupled but also steady-state.

Moreover, Boley and Weiner (Boley and Weiner, 1997) extended their reasoning considering also the conditions under which a thermoelastic problem can be considered uncoupled and quasi static. They demonstrated, in fact, that when inertial effects are small, also the coupling effects are negligible. The condition on the inertial effects rises from a comparison between the thermal input characteristic time (TICT), t_0^T , and the mechanical (MCT), t_M , and thermal characteristic times (TCT), t_T , defined as

$$t_M = \frac{L}{v_e}; \quad t_T = \frac{L^2 \rho c_\varepsilon}{K_p} \quad (4.26)$$

where L is the characteristic length of the problem and the term $\frac{K_T}{\rho c_\varepsilon}$ is the thermal diffusivity and it has dimensions $\left[\frac{m^2}{s} \right]$. The TICT can be evaluated starting from the boundary condition on temperature. If a temperature profile is assigned in a prescribed point of the boundary, $\mathbf{x} = x_0$, then, the TICT, t_0^T , can be determined as

$$t_0^T = \left(\frac{\frac{\partial T(x_0, t)}{\partial t}}{T_{MAX}} \right)^{-1} \quad (4.27)$$

These three times arise in all coupled problems, although their mode of definition is different; their relative orders of magnitude are dictated by physical consideration. Boley and Weiner (Boley and Weiner, 1997) reported that if the following inequalities subsist

$$t_T \gg t_M, \quad t_0^T \gg t_M \quad (4.28)$$

both coupling effects and inertial effects are small.

To this purpose, in thermoelasticity theory, the following parameter is introduced

$$h^T = \sqrt{\frac{t_M}{t_T}} \sqrt{\frac{t_M}{t_0^T}} \quad (4.29)$$

and, then, the thermoelastic problem results uncoupled and quasi static if

$$h^T \ll 1 \quad (4.30)$$

Replacing the relationships (4.26) in the equations (4.29), the condition (4.30) becomes:

$$\sqrt{\frac{K_T}{(\lambda + 2\mu)t_0^T c_\varepsilon}} \ll 1 \quad (4.31)$$

Employing the coupling between poroelasticity and thermoelasticity, the poroelastic input characteristic time (PICT) can be determined starting from the definition of the thermal one, (4.27), as

$$t_0^P = \left(\frac{\frac{\partial p(x_0, t)}{\partial t}}{P_{MAX}} \right)^{-1} \quad (4.32)$$

Moreover, starting from the definition of the TCT, equation (4.26), and employing the relationships

$$\begin{aligned} K_T &\leftrightarrow \frac{T_0 K_P}{\mu} \\ \rho c_\varepsilon &\leftrightarrow \frac{T_0}{M} \end{aligned} \quad (4.33)$$

the characteristic time of a poroelastic problem (PCT), t_p , can be, thus, written as

$$t_p = \frac{L^2 \mu}{K_p M} \quad (4.34)$$

and, from equation (4.29), a poroelastic problem results, indeed, uncoupled and quasi static if

$$h^P = \sqrt{\frac{t_M}{t_p}} \sqrt{\frac{t_M}{t_0^P}} \ll 1 \quad (4.35)$$

Replacing the relationships (4.26) and (4.34) in the equations (4.35), the uncoupled quasi-static condition becomes:

$$\sqrt{\frac{\rho K_p M}{(\lambda + 2\mu) t_0^P \mu}} \ll 1 \quad (4.36)$$

Table 4.3 is a résumé of the conditions presented in this paragraph. It represents, thus, a very important instrument because it allows to estimate a priori if the examined problem is coupled, uncoupled or quasi-static, avoiding, indeed, excessive computational costs in the analyses performed. The first step of this analysis consists, thus, in the evaluation of the input time, t_0^T or t_0^P , starting from the boundary conditions. Then, the parameters h^T , for the thermoelastic problem, and h^P , for the poroelastic one, are evaluated to determine if the problem is uncoupled quasi static. If the conditions (4.31) or (4.36) do not hold, the conditions (4.21) and (4.25) are investigated, to verify if the problem is uncoupled. Finally, if also these two last conditions do not subsist, the problem results coupled.

	<i>P</i>	<i>T</i>
t_0	$t_0^P = \left(\frac{\frac{\partial p(x_0, t)}{\partial t}}{P_{MAX}} \right)^{-1}$	$t_0^T = \left(\frac{\frac{\partial T(x_0, t)}{\partial t}}{T_{MAX}} \right)^{-1}$
Uncoupled Quasi static	$\sqrt{\frac{\rho K_p M}{(\lambda + 2\mu)t_0^P \mu}} \ll 1$	$\sqrt{\frac{K_T}{(\lambda + 2\mu)t_0^T c_\varepsilon}} \ll 1$
Uncoupled	$\frac{\dot{\varepsilon}}{\dot{p}} \ll \frac{1}{M}$	$\frac{\dot{\varepsilon}}{3\alpha \dot{T}} \ll \left(\frac{\lambda + 2\mu/3}{\lambda + 2\mu} \right) \frac{1}{\delta}$

Table 4.3

Résumé of the uncoupled / quasi static conditions for thermoelastic and poroelastic problems

CHAPTER V

REMARKS ON THE FINITE ELEMENT METHOD

5.1 The Finite Element Method (FEM)

The finite element method (FEM) is a numerical analysis technique for obtaining approximate solutions to a wide variety of engineering problems. Although originally developed to study stresses in complex airframe structures, it has since been extended and applied to the broad field of continuum mechanics. Because of its diversity and flexibility as an analysis tool, it is receiving much attention in engineering schools and in industry. In more and more engineering situations today, it is necessary to obtain approximate numerical solutions to problems rather than exact closed-form solutions. Without too much effort, the governing equations and boundary conditions for these problems can be written, but no simple analytical solution can be found.

The FEM envisions the solution region as built up of many small, interconnected subregions or elements. A finite element model of a problem gives a *piecewise* approximation to the governing equations. The basic premise of the FEM is that a solution region can be analytically modeled or approximated by replacing it with an assemblage of discrete elements. Since these elements can be put together in a variety of ways, they can be used to represent exceedingly complex shapes. In a continuum problem of any dimension, the field variable (whether it is pressure, temperature, displacement, stress, or some other quantity) possesses infinitely many values because it is a function of each generic point in the body or solution region. Consequently, the problem is one with an infinite number of unknowns. The finite element discretization procedures reduce the problem to one of a finite number of unknowns by dividing the solution region into elements and by expressing the unknown field variable in terms of assumed approximating functions within each element. The approximating functions (sometimes called *interpolation functions*) are defined in terms of the values of the field variables at specified points called *nodes* or *nodal points*. Nodes usually lie on the element boundaries where adjacent elements are connected. In addition to boundary nodes, an element may also have

a few interior nodes. The nodal values of the field variable and the interpolation functions for the elements completely define the behavior of the field variable within the elements. For the finite element representation of a problem, the nodal values of the field variable become the unknowns. Once these unknowns are found, the interpolation functions define the field variable throughout the assemblage of elements.

Clearly, the nature of the solution and the degree of approximation depend not only on the size and number of the elements used but also on the interpolation functions selected. As one would expect, these functions cannot be chosen arbitrarily, because certain compatibility conditions should be satisfied. The interpolation functions are often chosen so that the field variable or its derivatives are continuous across adjoining element boundaries. This feature is the ability to formulate solutions for individual elements before putting them together to represent the entire problem. This means, for example, that in the case of a problem in stress analysis, the force–displacement or stiffness characteristics of each individual element are first determined and, then, the elements are assembled to find the stiffness of the whole structure. In essence, a complex problem reduces to considering a series of greatly simplified problems. Another advantage of the finite element method is the variety of ways in which one can formulate the properties of individual elements. There are basically three different approaches. The first approach to obtain element properties is called the *direct approach* because its origin is traceable to the direct stiffness method of structural analysis. Element properties obtained by the direct approach can also be determined by the *variational approach*. The variational approach relies on the calculus of variations and involves the extremization of a *functional*. For problems in solid mechanics, the functional turns out to be the potential energy, the complementary energy, or some variant of them. A third and even more versatile approach for deriving element properties has its basis in mathematics and is known as the *weighted residuals approach*. The weighted residuals approach begins with the governing equations of the problem and proceeds without relying on a variational statement. This approach is advantageous because it thereby becomes possible to extend the finite element method to problems where no functional is available. The method of weighted residuals is widely used to derive element properties for nonstructural applications such as heat transfer and fluid mechanics.

Regardless of the approach used to find the element properties, the solution of a continuum problem by the finite element method always follows an orderly step-by-step process:

1) *Discretize the Continuum*

The first step consists in the division of the continuum or solution region into elements. A variety of element shapes may be used and different element shapes may be employed in the same solution region. Indeed, when analyzing an elastic structure that has different types of components such as plates and beams, it is not only desirable but also necessary to use different elements in the same solution.

2) *Select Interpolation Functions*

The second step, instead, consists in the assignation of nodes to each element and, then, in the choice of the interpolation function to represent the variation of the field variable over the element. The field variable may be a scalar, a vector, or a higher-order tensor. Polynomials are often selected as interpolation functions for the field variable because they are easy to integrate and differentiate. The degree of the polynomial chosen depends on the number of nodes assigned to the element, the nature and number of unknowns at each node and certain continuity requirements imposed at the nodes and along the element boundaries. The magnitude of the field variable as well as the magnitude of its derivatives may be the unknowns at the nodes.

3) *Find the Element Properties*

Once the finite element model has been established (that is, once the elements and their interpolation functions have been selected), the matrix equations expressing the properties of the individual elements can be evaluated. For this task, one of the three approaches just mentioned can be used: the direct approach, the variational approach or the weighted residuals approach.

4) *Assemble the Element Properties to Obtain the System Equations*

To find the properties of the overall system modeled by the network of elements all the element properties must be “assembled”. In other words, the matrix equations expressing the behavior of the elements are combined to form the matrix equations expressing the behavior of the entire system. The matrix equations for the

system have the same form as the equations for an individual element except that they contain many more terms because they include all nodes. The basis for the assembly procedure stems from the fact that at a node, where elements are interconnected, the value of the field variable is the same for each element sharing that node. A unique feature of the finite element method is that the system equations are generated by the assembly of the individual *element* equations. In contrast, in the finite difference method the system equations are generated by writing nodal equations.

5) *Impose the Boundary Conditions*

Before the system equations are ready for solution they must be modified to account for the boundary conditions of the problem. At this stage, nodal values of the dependent variables or nodal loads are imposed.

6) *Solve the System Equations*

The assembly process gives a set of simultaneous equations to be solved to obtain the unknown nodal values of the problem. If the problem describes steady or equilibrium behavior, a set of linear or nonlinear algebraic equations is solved. On the contrary, if the problem is unsteady, the nodal unknowns are time depending and, so, a set of linear or nonlinear ordinary differential equations must be solved.

7) *Make Additional Computations If Desired*

Many times the solution of the system equations are employed to calculate other important parameters. For example, in a structural problem the nodal unknowns are displacement components. From these displacements, element strains and stresses can be evaluated. Similarly, in a heat-conduction problem the nodal unknowns are temperatures, and from these element heat fluxes are calculated.

5.2 The Finite Element Modeling Package ANSYS®

To solve the differential coupled poroelastic equations with the FEM, the software ANSYS® 11 has been employed. ANSYS® is a general purpose finite element modeling package for the numerically solving of a wide variety of problems. The choice of this

software has been dictated first of all by the possibility to use a *batch approach*, creating custom-made macros for the specific problem to solve. This approach, in fact, allows to write in a text file a sequence of command lines. This strategy results very advantageous for complex problems because it gives the possibility to easily modify the command lines but, above all, to realize parametric models. Moreover, another important aspect is the possibility to perform multiphysics simulations. In an expanding range of applications, engineers and designers must be able to accurately predict how complex products will behave in real-world environments where multiple types of coupled physics interact. Multiphysics simulation software from ANSYS allows to create virtual prototypes of specific designs operating under real-world multiphysics conditions. This industry leading software enables to simulate the interaction between structural mechanics, heat transfer, fluid flow and electromagnetics all within a single, unified engineering simulation environment. By incorporating multiphysics simulation into the design process, engineers reduce error margins, increase product reliability, and ultimately create more innovative product designs. Multiphysics simulation from ANSYS provides a portfolio of high-fidelity engineering analysis tools that enable engineers to accurately predict real-world behavior. ANSYS multiphysics solutions combine the most comprehensive set of solver technology for all physics disciplines — structural mechanics, heat transfer, fluid flow and electromagnetics — with an open and adaptive ANSYS® Workbench™ environment, flexible simulation methods, and parallel scalability. Together these cutting edge technologies form the foundation for comprehensive multiphysics simulation capable of solving the most complex engineering challenges.

The ANSYS Workbench platform is a powerful multi-domain simulation environment that harnesses the core physics from ANSYS, enables their interoperability, and provides common tools for interfacing with CAD, repairing geometry, creating meshes and post-processing results. An innovative project schematic ties together the entire simulation process, guiding the user through complex multiphysics analyses with drag-and drop simplicity.

Moreover, ANSYS multiphysics solutions deliver proven methods to solve multiphysics problems, including solutions for both direct and sequentially coupled problems. Direct coupled-field elements allow users to solve multiphysics problems by employing a single finite element model with the appropriate coupled-physics options set within the element itself. A direct coupled field solution simplifies the modeling of multiphysics problems by allowing the engineer to create, solve and post-process a single analysis model for a wide

variety of multiphysics applications. Sequential coupling, instead, allows engineers to solve multiphysics problems with the automated multiphysics coupling available in ANSYS Workbench, which couples multiple single-physics models into one unified simulation. The platform supports both one-way and two-way sequential solutions for multiphysics problems such as thermal-stress analysis, microwave heating and fluid structure interaction.

The software ANSYS[®] is organized into three modules.

1) ***Preprocessing module***

This module allows to characterize the specific problem to solve in terms of geometry, element type, definition of the material properties of the element and mesh.

2) ***Solution processor module***

In this module, instead, load and constraint conditions are assigned and the specific kind of solution is conveniently selected.

3) ***Post processing module***

The last module furnishes the results of the problem in three different form of visualization: in terms of numerical data lists, with vectorial graphics or through chromatic bands.

5.3 Element SOLID70

As underlined in Chapter IV, the PTD theory allows to solve transient poroelastic problems as corresponding thermoelastic ones, interpreting the temperature as a pressure and thermal gradients as velocities. To perform coupled thermoelastic analyses, the element SOLID70 is employed. SOLID70 has a three-dimensional thermal conduction capability. The element has eight nodes with a single degree of freedom, temperature, at each node. The element is applicable to a three dimensional, steady-state or transient thermal analysis.

It has to be noticed that the characteristic transient time is evaluated coherently with the element size, as

$$t_{trans} = \frac{\delta^2}{4 \frac{K_T}{\rho c_\varepsilon}} \quad (5.1)$$

where, as underlined in the previous chapter, the term $\frac{K_T}{\rho c_\varepsilon}$ is the thermal conductivity and it has dimensions $\left[\frac{m^2}{s} \right]$.

The element also can compensate for mass transport heat flow from a constant velocity field. If the model containing the conducting solid element is also to be analyzed structurally, the element should be replaced by an equivalent structural element (such as SOLID45). An option exists that allows the element to model nonlinear steady-state fluid flow through a porous medium. With this option, the thermal parameters are interpreted as analogous fluid flow parameters. For example, the temperature degree of freedom becomes equivalent to a pressure degree of freedom.

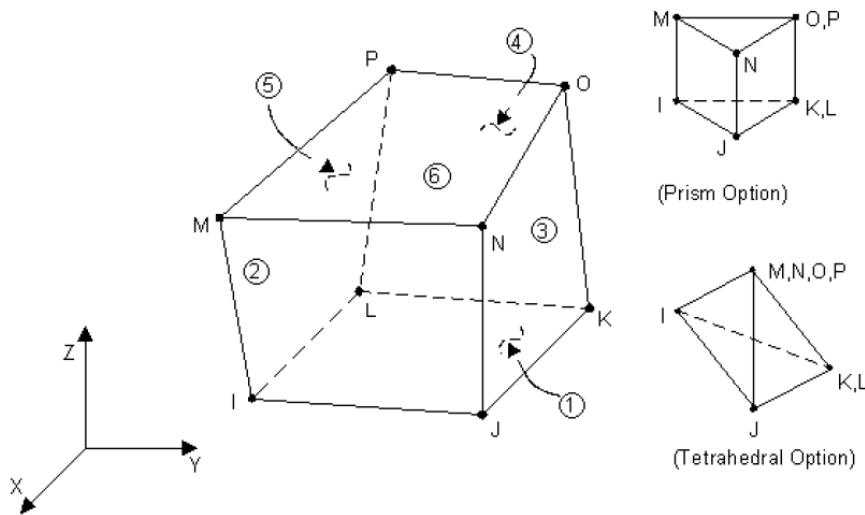


Figure 5.1
Solid70 Geometry

5.3.1 Input Data

The element is defined by eight nodes and the orthotropic material properties. Orthotropic material directions correspond to the element coordinate directions. Convections or heat

fluxes (but not both) may be input as surface loads at the element faces as shown by the circled numbers on SOLID70. Heat generation rates may be input as element body loads at the nodes. If the node I heat generation rate $HG(I)$ is input, and all others are unspecified, they default to $HG(I)$. The nonlinear porous flow option is selected with $KEYOPT(7) = 1$. For this option, temperature is interpreted as pressure and the absolute permeabilities of the medium are input as material properties KXX , KYY , and KZZ . Properties $DENS$ and $VISC$ are used for the mass density and viscosity of the fluid. Properties C and MU are used in calculating the coefficients of permeability. Temperature boundary conditions input with the **D** command are interpreted as pressure boundary conditions, and heat flow boundary conditions input with the **F** command are interpreted as mass flow rate (mass/time). A mass transport option is available with $KEYOPT(8)$. With this option the velocities VX , VY , and VZ must be input as real constants (in the element coordinate system). Also, temperatures should be specified along the entire inlet boundary to assure a stable solution. With mass transport, you should use specific heat (C) and density ($DENS$) material properties instead of enthalpy ($ENTH$). The following list is a summary of the SOLID70 possible input.

Element Name

SOLID70

Nodes

I, J, K, L, M, N, O, P

Degrees of Freedom

TEMP

Real Constants VX, VY, VZ IF $KEYOPT(8) > 0$ *Material Properties* $KXX, KYY, KZZ, DENS, C, ENTH,$ $VISC, MU$ ($VISC$ and MU used only if $KEYOPT(7) = 1$.)Do not use $ENTH$ with $KEYOPT(8) = 1$).*Surface loads*

face 1 (J-I-L-K), face 2 (I-J-N-M), face 3 (J-K-O-N),

face 4 (K -L-P-O), face 5 (L -I-M-P), face 6 (M-N-O-P)

Heat Fluxes

face 1 (J-I-L-K), face 2 (I-J-N-M), face 3 (J-K-O-N),

face 4 (K -L-P-O), face 5 (L -I-M-P), face 6 (M-N-O-P)

Body Loads

Heat Generations

HG(I), HG(J), HG(K), HG(L), HG(M), HG(N), HG(O), HG(P)

Special Features

Birth and death.

KEYOPT(2)

0 → Evaluate film coefficient (if any) at average film temperature, $(TS + TB)/2$

1 → Evaluate at element surface temperature, TS

2 → Evaluate at fluid bulk temperature, TB

3 → Evaluate at differential temperature $|TS-TB|$

KEYOPT(4)

0 → Element coordinate system is parallel to the global coordinate system

1 → Element coordinate system is based on the element I-J side

KEYOPT(7)

0 → Standard heat transfer element

1 → Nonlinear steady-state fluid flow analogy element

Note

Temperature degree of freedom interpreted as pressure.

KEYOPT(8)

0 → No mass transport effects

1 → Mass transport with VX, VY, VZ

5.3.2 Output Data

The solution output associated with the element is in two forms:

- ✓ nodal temperatures included in the overall nodal solution
- ✓ additional element output as shown in Element Output Definitions

Convection heat flux is positive out of the element; applied heat flux is positive into the element. If KEYOPT(7) = 1, the standard thermal output should be interpreted as the analogous fluid flow output. The element output directions are parallel to the element coordinate system.

CHAPTER VI

FEM APPLICATIONS

6.1 Introduction

Many analytical and numerical approaches have been proposed in order to solve poroelastic problems describing the behavior of biological tissues. The main difficulty associated to numerical strategies concerns the solution of the *coupled* poroelastic equations for determining the solid response in terms of deformation and filtration. The proposal of this work is to find a strategy to numerically solve poroelastic problems employing the Finite Element Method (FEM). In particular, the strategy presented is based on the well known similarity between thermoelasticity and poroelasticity theories. This analogy allows to solve transient poroelastic problems as corresponding thermoelastic ones, interpreting the temperature as a pressure and thermal gradients as velocities. With this aim, the relationship between thermoelasticity and poroelasticity is formulated in terms of dimensionless parameters to ensure numerical stability, because the elasticity moduli, filtration coefficients and porosity have essentially different orders of magnitude. Thus, the dimensionless equations obtained are implemented in numerical FEM-based computations. Such transferring to equivalent thermoelastic problems enables to apply the FEM package ANSYS[®] 11, which provides opportunities to solve coupled thermoelastic problems in transient non linear settings. Two numerical examples are presented. The first one is concerning a very important problem of drug delivery in solid tumors. The second example is, instead, related to the investigation of the role played by trigonal-like microstructure in osteons in bone adaptive, growth and remodeling processes.

6.2 Drug delivery to solid tumors

6.2.1 Introduction

The first FEM application proposed concerns the analysis of the Convection-Enhanced Delivery (CED) technique for the delivery of drugs to brain tissue. Primary central nervous system tumors are the second cause of cancer death in younger population ([Allard et al,](#)

2009). The difficulties in cancer treatment are associated to its characteristic features, such as the uncontrolled cell growth, not regulated by external signals, and the capacity to invade tissues, metastasize and colonize at distant sites. There are several modes of therapy for brain tumors. The first treatment is, usually, the tumor resection, associated to radiotherapy and chemotherapy. The major difficulties in the treatment of brain tumors is the effectiveness of the delivery of therapeutic agents. Drug delivery in vivo results difficult because of the presence of physiological barriers, drug resistance of tumor cells, tissue tolerance and so on (Yuan, 1998). In brain, the two major obstacles for drug delivery are represented by the blood-brain barrier (BBB), almost impermeable to drugs (Baxter and Jain, 1989), and the interstitial fluid pressure (IFP), which is elevated in the solid tumor and decreases abruptly in the tumor periphery (Jain and Baxter, 1988), caused by the disorganized vascular network and the absence of functional lymphatics. Many efforts have been made to model the phenomena involved in the delivery of drugs to solid tumors and to understand how to ride out physiological obstacles. Walker et al. (Walker et al., 1996), for example, proposed an analytical model to investigate the effect of the protocols to overcome the blood brain barrier on the different drug transport processes, focusing on the role of convection and the influence of the changing parameters. Netti et al. (Netti et al., 1995) proposed a poroelastic model of a solid tumor to investigate the mechanisms which regulate the interstitial fluid pressure, looking for a possible strategy to overcome this physiological barrier. Supporting the analytical approach with experimental data, they found that the periodic administration of vasoactive agents improve the effectiveness of the macromolecular delivery. Moreover, also tumor blood flow plays a crucial role in tumor therapy and it is characterized by temporal and spatial heterogeneities (Netti et al., 1996), probably due to the coupling between interstitial fluid pressure and tumor microvascular pressure (Mollica et al., 2003). Infusion-based techniques seem to be promising approaches for the delivery of therapeutic agents to brain tissue because convection enhances drug transport, ensuring the drug release in larger regions respect to pure diffusion. Based on these considerations, the Convection-Enhanced Delivery (CED) technique has been recently proposed. It is defined as the continuous delivery of a therapeutic fluid agent simply guided by pressure gradients (Allard et al., 2009).

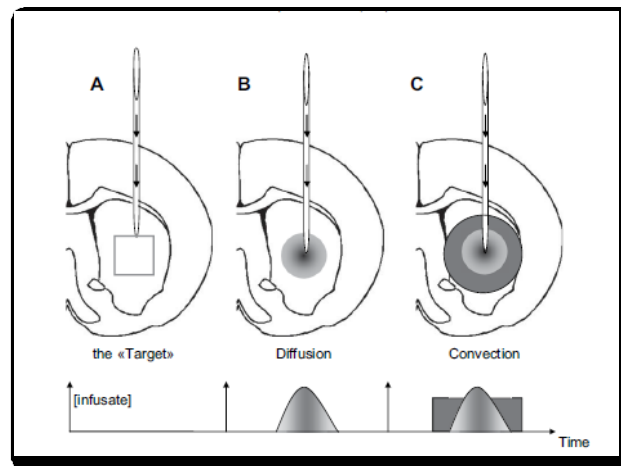


Figure 6.1

Schematic representation of CED mechanism (Allard et al., 2009).

- A: identification of the target site with correct placement of the catheter according to specific coordinates.
- B: Diffusion occurs all the time but is rigorously dependent of the infusate nature.
- C: Convection (or bulk flow) is strictly dependent on the pressure gradient and occurs during all the establishment of the pressure gradient.

CED enables the drugs to cross the BBB and supplements diffusion in the delivery of large drugs over required distances, determining greater in situ drug concentrations and reducing systemic toxicity. A wide range of substances can be locally delivered with this technique, such as monoclonal antibodies, conventional chemotherapeutic agents, proteins, nanocarriers, targeted toxins and viruses. The effectiveness of CED is strictly connected to the different parameters proper of this technique. For this reason, CED protocols need to take into account the infusate concentration, the volume of the infusate, the infusion rate and site, the backflow mechanism. To improve CED protocols and to predict drug distribution profiles, analytical and numerical models have been developed. To this purpose, the poroelasticity theory is a very useful instrument to describe soft tissue mechanics (Biot, 1955) and it can also be used to model the coupling between fluid flow and solid deformation in tumors. Bassar (Bassar, 1992) presented an analytical model of infusion-induced swelling in brain, treating white and gray matter as linear poroelastic isotropic media. He found an analytical steady-state solution to estimate interstitial fluid pressure and fluid velocity profiles during infusion into brain. Smith and Humphrey (Smith and Humphrey, 2007) proposed a model for the CED in brain tissue, deriving the interstitial fluid pressure and fluid velocity induced by infusion into brain tissue and in a tissue-isolated tumor. They determined steady-state and transient solutions for the proposed model. Also Netti et al. (Netti et al., 1997) employed the poroelasticity theory to

describe fluid movement in soft tissues at macroscopic and microscopic scales, specializing the model to a local analysis of blood flow around a single blood vessel. Moreover, they applied the model to determine an analytical solution for a spherical solid tumor, obtaining the interstitial fluid pressure and fluid velocity profiles. Roose et al. (Roose et al., 2003), instead, employing a poroelastic model, investigated solid stress associated to a spheroid tumor growth in order to better understand the effects of the growth on the surrounding environment. The model, validated by experimental results, suggests that the range of stresses created by tumor growth are considerable and could collapse blood and lymphatics vessels, contributing to the lack of vessels in the middle of the tumor. Moreover, to take into account transient evolution of the phenomena associated to the drug delivery to solid tumors, Netti et al. (Netti et al., 2003) proposed a poroviscoelastic model for a spherical geometry to analyze how mechanical stresses and deformations influence macromolecular distribution in a gel, in order to simulate an intratumoral infusion. Also biphasic theory have been used to develop an analytical model to describe drug delivery to solid tumors. Garcia and Smith (Garcia and Smith, 2008), in fact, employed a biphasic hyperelastic model to describe infusion into brain, attributing the differences between linear solution and nonlinear analyses to geometric nonlinearities. However, the interest of the scientific community is increasingly addressed to numerical approaches. FE models, in fact, allow to describe more realistic infusion protocols and geometries and to perform parametric analysis. Linninger et al. (Linninger et al., 2008) proposed a computational technique to rigorously predict the distribution of drugs in brain tissue, based on the three-dimensional reconstruction from patient-specific images. This approach allows to take into account brain heterogeneity and anisotropy. Chen and Sarntinoranont (Chen and Sarntinoranont, 2007) employed the software package ADINA to study the effects of pressure-induced swelling on the macromolecular transport, modeling brain tissue as a biphasic isotropic medium. They validated their results comparing them to the analytical solution of Bassar (Bassar, 1992) and developed a sensitivity analysis to quantify the effect of the changes in the material parameters on the pressure-controlled infusion. As highlighted in this introduction, the CED technique has been investigated by many authors because it represents a challenging approach to overcome the physiological barriers in brain tumors treatment. In this chapter, a FE computational model of CED protocols, based on the PTD theory, is presented. However, this approach presents some limits. The model employed, in fact, is linear and isotropic, for both the constitutive behavior and the permeability. These assumptions are the same used

by Basser (Basser, 1992). The other limit is that the therapeutic fluid agent is simply guided by pressure gradients, modeled employing the Darcy's law, and not by a diffusion process, described by Fick's law. On the contrary, an advantage of the approach proposed is the possibility to perform FEM analyses, by starting from mechanical, geometrical and infusion data reported in the scientific literature. Following this way, a parametrical custom-made ANSYS® environment macro is used to perform steady state and transient poroelastic analyses employing the PTD theory. Another important advantage of this model consists in the possibility of simulating in silico sensitivity analyses to determine the effects of different parameters on the effectiveness of the infusion protocols.

6.2.2 FE model of drug delivery to solid tumors

The first FEM analysis has been performed to compare the analytical steady state solution presented by Basser (Basser, 1992) for a step brain infusion from a pressure source into a spherical cavity of radius a , with the solutions obtained with the software ANSYS®. As just said before, brain tissue is modeled as an isotropic poroelastic medium. Starting from Biot's poroelasticity theory, the solution is found imposing that the pressure in the cavity suddenly jumps from zero to P_0 , i.e. $P(a,t) = P_0 H(t)$, as illustrated in Figure 6.2.

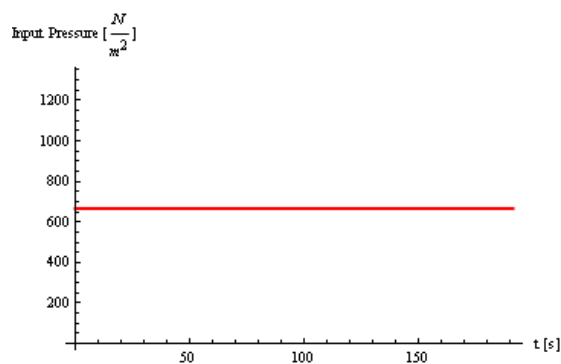


Figure 6.2

Input Pressure in the cavity

The resulting pressure distribution for $r \gg a$ is

$$P(r,t) = P_0 \frac{a}{r} \left(1 - \operatorname{erf} \left(\frac{r-a}{2\sqrt{ct}} \right) \right) \quad (6.1)$$

where $c = \frac{K_P}{\mu} (\lambda + 2\mu_{solid})$ is the consolidation coefficient. Figure 6.3 shows the spherical pore of radius a within an infinite poroelastic tissue sample.

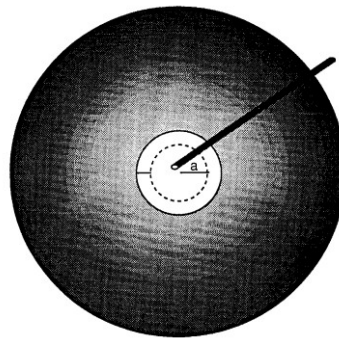


Figure 6.3

The spherical pore of radius a within an infinite poroelastic tissue sample (Basser, 1992)

Moreover, because the solution found by Basser (Basser, 1992) refers to an infinite medium, the numerical solution is evaluated imposing on the external surface the pressure profile obtained from equation (6.1) when $r = 5a$, as shown in Figure 6.4.

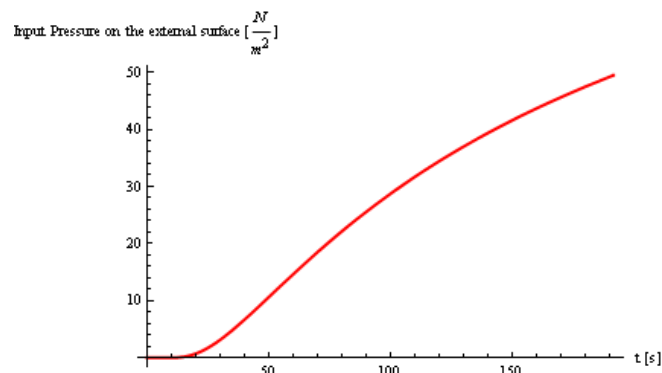


Figure 6.4

Input Pressure on the external surface

The infusion parameters employed by Basser (Basser, 1992) are reported in Table 6.1.

INFUSION PARAMETERS		
Infusion pressure	$P_0 = 6664$	<i>dynes / cm²</i>
Infusion flow rate	$Q_0 = 10^{-5}$	<i>cm³ / s</i>
Radius of spherical cavity	$a = 0.03$	<i>cm</i>
Radius of tissue sample	$R_0 = 2$	<i>cm</i>
Solute diffusivity	$D = 10^{-7}$	<i>cm² / s</i>
Gray Matter		
Shear modulus	$G = 2 \cdot 10^4$	<i>dynes / cm²</i>
Lamé constant	$\lambda = 9 \cdot 10^5$	<i>dynes / cm²</i>
Permeability	$\kappa = 5 \cdot 10^{-9}$	<i>cm⁴ / dynes s</i>
Pore fraction	$f = 0.2$	<i>dimensionless</i>
White Matter		
Shear modulus	$G = 9 \cdot 10^3$	<i>dynes / cm²</i>
Lamé constant	$\lambda = 4 \cdot 10^5$	<i>dynes / cm²</i>
Permeability	$\kappa = 7.5 \cdot 10^{-9}$	<i>cm⁴ / dynes s</i>
Pore fraction	$f = 0.2$	<i>dimensionless</i>

Table 6.1

Infusion parameters employed by Basser (Basser, 1992)

To compare analytical and numerical results, brain tissue is modeled as a sphere with an infusion cavity of radius a . Referring to the step-by-step procedure illustrated in Chapter V, after the definition of the problem geometry, the following passage concerns the domain discretization. The Finite Elements Method based model is constructed by means of hexahedral 8 nodes elements with linear shape functions generating a 16875 elements and 18746 nodes mesh. The element chosen for the mesh, i.e. SOLID70, requires that opposites

sides of the discretized domain have the same number of divisions. Moreover, to optimize the mesh, the element size increases with the sphere radius. Figure 6.5 illustrates the number of divisions along the radius, m , and along the circular arches, n .

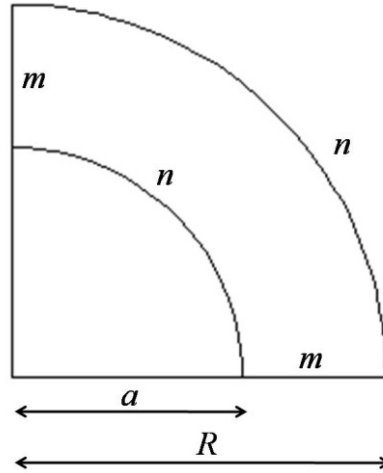


Figure 6.5

Division numbers along the radius, m , and along the circular arches, n

To this purpose, if $\alpha = \frac{a}{R}$, the number of divisions m along the radius is evaluated as the geometrical average, i.e.,

$$m = \frac{2n}{\pi} \frac{1-\alpha}{\sqrt{\alpha}} \quad (6.2)$$

The relationship (6.2) allows to determine, starting from n , the number of divisions m , as function of the ratio between the cavity radius and the sphere one. The Finite Element Mesh of the model proposed is shown in Figure 6.6. Because the problem is axial-symmetrical, only $\frac{1}{4}$ of the whole geometry is represented.

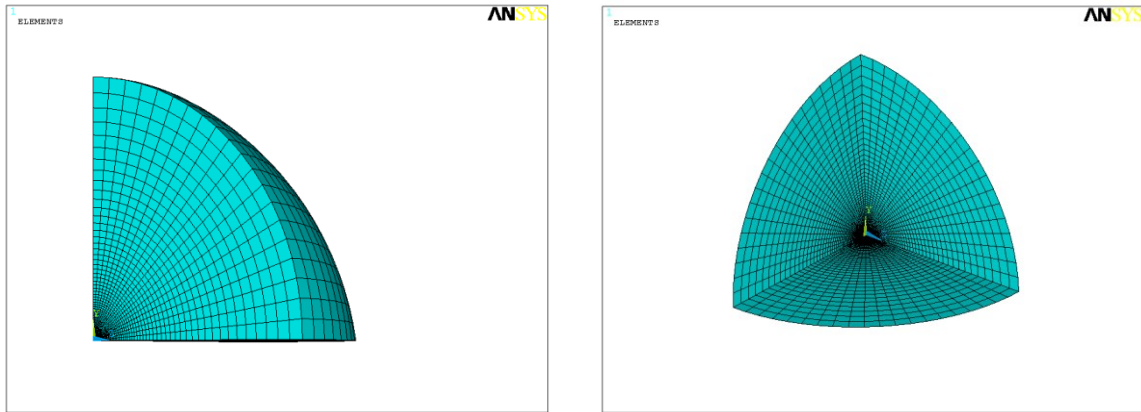


Figure 6.6

Finite Element Mesh of the model proposed

The steady state solutions for the analytical and numerical analyses overlap, as shown in Figure 6.7.

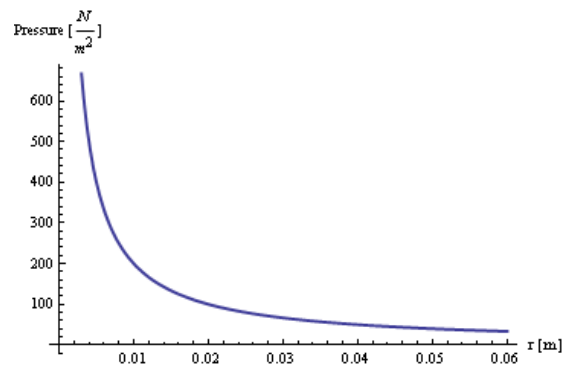


Figure 6.7

Steady state solution for the problem of consolidation in an infinite, isotropic medium

Moreover, adopting the same geometry and mesh as well as the same input conditions, a transient analysis has also been performed, making reference to the parameters reported in Table 6.2. The transient analysis has been conducted in 40 substeps, each lasting 2 s.

INPUT PARAMETER	Value	Reference
Tissue sample radius R [m]	$2 \cdot 10^{-2}$	(Basser, 1992)
Hydraulic conductivity, $\frac{\kappa}{\mu} \left[\frac{m^2}{Pa \cdot s} \right]$	$5 \cdot 10^{-12}$	(Basser, 1992)
Elastic shear modulus G [Pa]	$2 \cdot 10^3$	(Basser, 1992)
Lamé constant λ [Pa]	$9 \cdot 10^4$	(Basser, 1992)
Storage Modulus $\frac{1}{M}$ [Pa]	$1.8356 \cdot 10^{-8}$	(Li et al., 2009)
Density $\rho \left[\frac{Kg}{m^3} \right]$	1000	
Reference Temperature T_0 [K]	1	

Table 6.2

Parameter values used in the model

Figure 6.8 illustrates pressure variations with the radius for different time substeps.

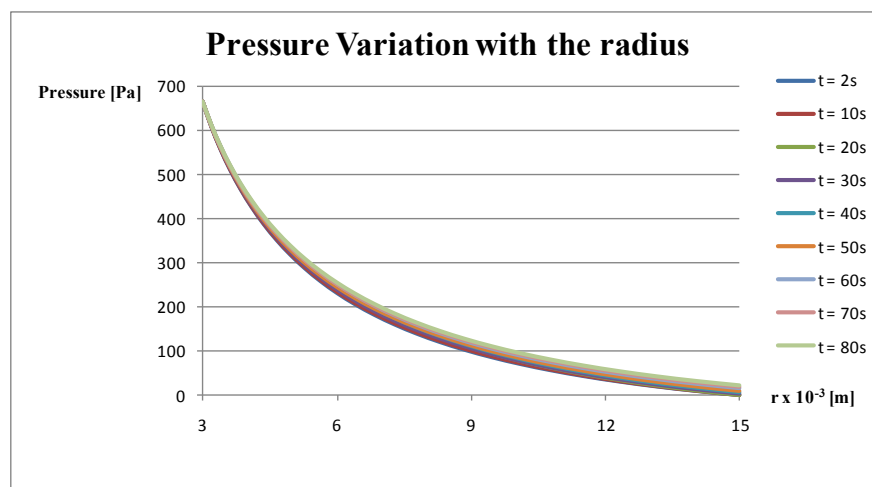


Figure 6.8

Pressure variations with the radius for different time substeps

It has to be noticed that these profiles show an oscillatory effect, as illustrated in Figure 6.9, because pressure values increase or decrease in an alternative way, passing from a time value to the following one.

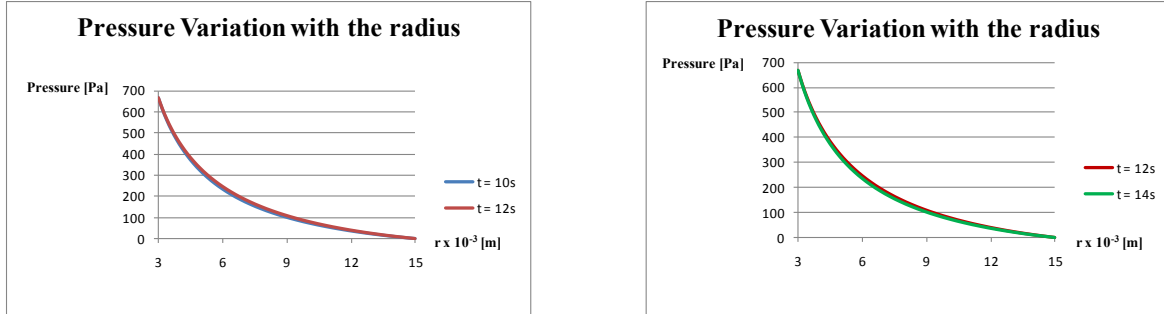


Figure 6.9

Pump-like effect of pressure profiles

Besides, it is very interesting to investigate also pressure variation with time for different radius values. The graphics in Figure 6.10 illustrates, in fact, the decreasing weight of the transitory waves when the radius increases. Pressure profiles, in fact, are more affected by the oscillatory behavior induced by the transitory presence for radius values next to the infusion cavity then for radius values far from it.

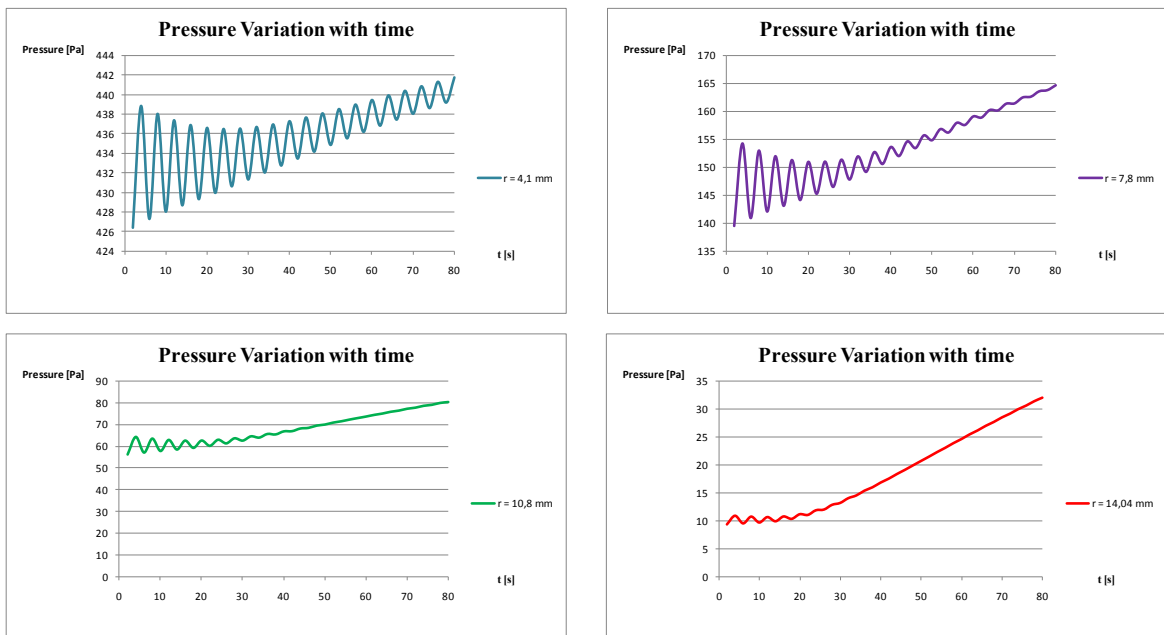


Figure 6.10

Decreasing weight of the transitory waves when the radius increases

The following figure, instead, concerns the pressure map for a selected time substep. Extending the analysis to the whole temporal range, also in this case the oscillatory behavior outcrops. Moreover, it has to be noticed that Figure 6.11 – 6.14 are associated to the output of the thermo-mechanical analysis and, so, all the values need to be multiplied for the appropriate coefficients to transform them into poroelastic output.

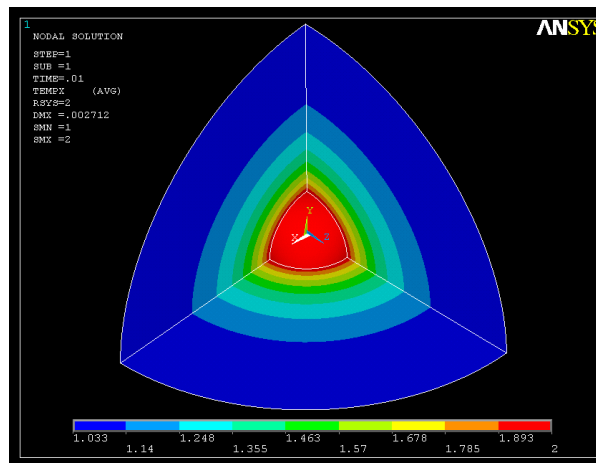


Figure 6.11
Pressure Map

Figures 6.12a-b are, instead, the deformation maps in the spherical coordinates.

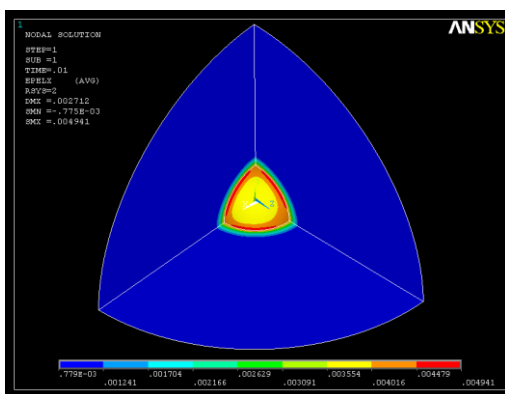


Figure 6.12a

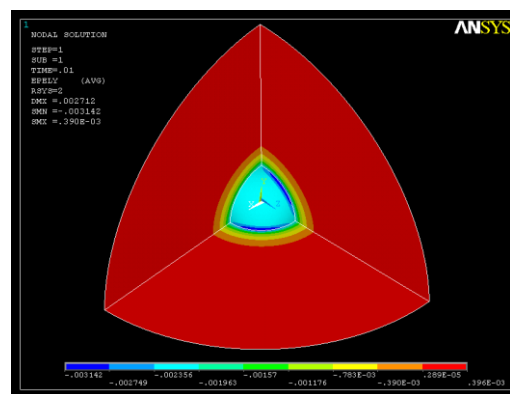


Figure 6.12b

Deformation Maps

Figure 6.13 reports the radial displacement map.

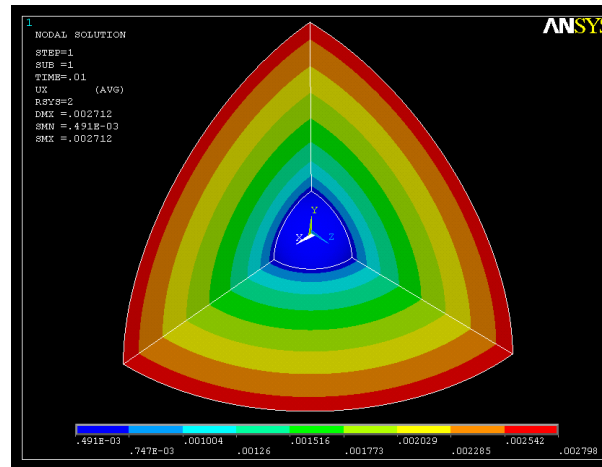


Figure 6.13
Radial Displacement Map

Finally, Figure 6.14 reports the Von Mises stress map. Von Mises stresses are very important parameters in order to ensure that the infusion input applied to brain do not cause the tissue failure. These stresses could, in fact, be used to introduce a stretch ratio, defined as the ratio between the stresses experienced by the tissue and the brain yield stress, referring, for example, to the work of Velardi et al. (Velardi et al., 2006). Values of the stretch ratio less than one ensure that the infusion procedure adopted preserves tissue integrity.

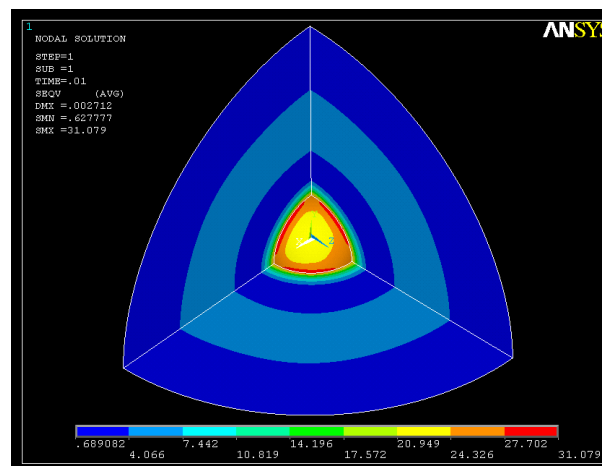


Figure 6.14
Von Mises stress Map

It is worth to note that replacing the values reported in Table 6.2 in the expression (4.36) and considering t_0^p as 80 s, the inequality $h^p \ll 1$ subsists and, thus, the problem results uncoupled and quasi static.

As highlighted before, the purpose of these analyses concerns the improvement of CED protocols. The back-flow mechanism occurring in CED will be objet of further investigations. By CED, in fact, the drug delivery is driven by the pressure gradient, due to the difference between the skull pressure and the infusion one and, so, the injection flow is a crucial parameter for the effectiveness of the infusion. Moreover, the infusion rate is limited by the back-flow mechanism. Back-flow can cause the release of the drug in not targeted brain regions and it can also induce a drug lack where necessary. Back-flow depends, above all, on three parameters: the catheter placement, the injection rate and the catheter diameter. Moreover, for the constancy of the fluid discharge, the injection rate and the catheter diameter are strictly connected and, thus, only the diameter can be considered as a crucial parameter in the induction of the back-flow. Two different kinds of backflow can be envisaged. First of all, backflow can occur because the catheter placement can cause the mechanical disruption of the tissue and the formation of voids, determining the reflux of the therapeutic infused agent through that gap. However, backflow can be also intrinsic, associated to the tissue separation from the catheter induced by the pressure guiding the infusion process. This phenomenon stops only when this pressure is balanced by the shear forces in the tissue (Raghavan et al., 2006). The FE software ANSYS could be employed to investigate the transient profiles of pressure and velocity and the influence of different parameters on the back-flow mechanism occurring in CED. This aspect is very important because, even if CED technique ensures larger volumes of drug distribution, its clinical application is not widespread for some obstacles, such as backflow itself, responsible of the uncontrolled drug release (Ivanchenko et al., 2010).

6.3 The role of osteon micro-structure in bone growth and remodeling

6.3.1 Introduction

The second FEM application concerns, instead, the analysis of the role of bone microstructure in bone mechanotransduction process. Bone is a living tissue, hierarchically organized, constituted by liquid and solid components, strictly interacting to optimize the

structure for its functions (Knothe Tate, 2003). Bone cells actively recognize and respond to mechanical and chemical stimuli in the process known as mechano-chemical transduction. Human bone is continuously renewed by basic multicellular units (BMUs), working in a coordinate fashion to reabsorb old bone and, then, filling the gap with new bone tissue organized in osteons in cortical bone. The mechanical properties of these secondary osteons are crucial for the stability of the entire bone. The cells involved in the remodeling process are the osteoblasts, actively engaged in the production of extracellular matrix (Cowin et al., 1991) and the osteoclasts, bone reabsorbing cells, coordinated by the osteocytes, considered the underestimated conductors of bone orchestra (Bonucci, 2009). Osteocytes are thought to be the mechanosensory cells in bone because they detect physical stresses, translating them into autocrine and paracrine signals. Mechanical stimuli can be transmitted through the solid matrix of the tissue or indirectly via fluid pressure and shear stresses caused by fluid moving through the lacunocanalicular system due to load-induced fluid flow. Moreover, also chemical signals, associated to diffusive, convective and active transport mechanisms, arrive intracellularly or through the extracellular fluid in which the cells live. A central role in the mechanotransduction process is carried out by the lacunocanalicular system, which serves as fluid reservoir and, thus, is determinant for the signals transmission. Pericellular fluid in this network is the coupling medium for the translation of mechanical forces into biochemical, mechanochemical, mechanobiological and electromechanical effects in cells, the “machine tools” for bone remodeling. Different biophysical and electrochemical mechanisms can cause bone fluid motion. Apart from endogenous mechanisms, such as active transport in osteocytes, pressure gradients associated to osmotic or pulsatile pressures and exogenous mechanisms induced by mechanical loading can determine fluid motion. Bone tissue behaves like a hierarchically organized stiff, dense, fluid-filled sponge and, as a consequence, Biot’s theory of poroelasticity enables to describe the interactions between the solid matrix and the fluid phase (Cowin et al., 2009). Mechanical loading in bone is associated to a tissue stress state comprising cyclic dilatational and deviatoric components. The dilatational component kindles the fluid pressure, inducing the fluid flow through deformation of the fluid-filled lacunocanalicular and intermatrix porosities within bone tissue. According to Biot’s theory, compression deforms the solid matrix of a porous material, raising instantaneously a pressure increase in the fluid within the pores. The differences in pressure between the interior and exterior of a porous solid cause a net flow of fluid. Removal of load results, instead, in a pressure gradient which guides the fluid inward, until it reduces to zero. Bone

formation induced by mechanical loading is site-specific and, so, it depends on the stimuli perceived by the skeleton. Different possible remodeling stimuli have been considered, such as strain magnitude, strain rate, strain frequency and the strain tensor. Recently, Gross et al. (Gross et al., 1997) indicated that peak magnitude strain gradients, deducible from bone load environment and geometry, are strictly correlated with the sites of bone formation. Moreover, strain gradients are associated to fluid flow in the canalicular network. Ruimerman et al. (Ruimerman et al., 2005) considered both the effects of the volumetric strain, representing the actual load on the osteocytes, and of its gradient, related to the mechanical effects on fluid flow. As illustrated, osteon microstructure plays a fundamental role in guiding fluid flow and is optimized for the functions it has to fulfill. Bone is an intelligent material and its architecture is a consequence of the loads acting on it. The cylindrical osteons design can be seen as the response to the load history. Their distribution in compact bone, in fact, corresponds to the distribution of principal stresses acting on bone. Osteons structure ensures maximum load-bearing capacity and resistance to weakness induced by fatigue and microdamage (Weiner et al., 1999). Băca et al. (Băca et al., 2007) analyzed the course of osteons of the human proximal femur, underlying that osteons are present above all in the regions subjected to high stress and absent in all regions where loading of the bone is not significant. Osteons enable bone to respond optimally to the stress applied thanks to their peculiar mechanical properties, determined by the specific pattern of collagen fibers. Tests of macroscopic samples have demonstrated that collagen fibers orientation is correlated to the mechanical properties of long bones, independently of the type of species. Ramasamy et al. (Ramasamy et al., 2006) argued that collagen fibers orientation is a potential result of a microarchitectural adaptation process to the load environment and that the specific orientation is determined by the mineralization that freezes the collagen fibers in the directions dictated by physiological strains. Collagen fibers orientation is considered an important predictor of the tensile strength of cortical bone and a measure of toughness. Skedros et al. (Skedros et al., 2009) noted that longitudinal oriented collagen fibers determine greater strength in tension and also a greater elastic modulus, while transverse collagen fibers are optimized for compressive stresses. Fibers orientation obviously changes within the bone segments. Beraudi et al. (Beraudi et al., 2009) analyzed the collagen orientation in human femur, tibia and fibula shaft by circularly polarized light. They found, indeed, that transverse fibers become predominant moving versus epiphyses where the compressive physiological forces are more aligned with the shaft cross section, confirming that the collagen pattern is strictly dependent on

the loads to bear. Besides, collagen orientation is a fundamental factor also in fracture initiation and arrest (Weiner et al., 1999). Microdamage in bone occurs in the form of microcracks as a result of everyday cyclical loading activities (Mohsin et al., 2006) and it represents a stimulus for remodeling. Porosity, mineralization, collagen fibers orientation are all factors which promote cracks initiation, but hinder their growth. Gupta et al. (Gupta et al., 2006) considered osteons as mechanically modulated laminates of mineralized collagen fibril layers, characterized by the alternance of a wide band of stiffer mineralized matrix with thin bands of softer material. This mechanical modulation provides an example of a natural crack stopping mechanism. Moreover, also the stiffness variation of single lamellae may serve as a crack trapping mechanism inside osteons, preventing cracks running in the interstitial bone from propagating toward the inner Haversian canal. However, lamellar interface in bone is weak and, so, it is the principal site of shear damage formation, but it is also highly effective in keeping cracks isolated from each others. Some authors also proposed that the cement lines, surrounding osteons, can be seen as barriers to crack growth (O'Brien et al., 2007), because they can reduce the shear strength of osteonal bone. O'Brien et al. explained the osteons crack-stopping mechanism comparing them to composite materials. Also osteons, in fact, provide numerous sites for crack initiation, but the fibers act as barriers and prevent further growth. Another important aspect of osteons microstructure needs to be considered. Wagermaier et al. (Wagermaier et al., 2006) hypothesized a three-dimensional spiraling of collagen fibrils in osteonal bone. They argued that the helicoidal structure provides more resistance to mechanical loads and enables a higher extensibility in tension and compression. They proposed that one of the advantages of such a helicoidal plywood structure could be the protection of the blood vessels against failure of the surrounding matrix. Nevertheless, at the best author knowledge, no works have been presented in literature where the helical microstructure of lamellae in osteons has been interpreted as a significant factor for driving nutrients.

6.3.2 FE simulation of a typical osteon unit

A poroelastic steady-state analysis has been conducted on a FEM model of osteons to demonstrate that osteons microstructure itself is a key element to understand bone adaptive, growth and remodeling processes, employing the PTD theory. Numerical simulations have been carried out considering that the osteon length and its internal radius

are respectively 300 μm and 30 μm . In this model, the osteon is constituted by 10 lamellae with a thickness of about 5 μm . For the wrapping angle, nine different values are considered to simulate T-type osteons ($\theta = 0$), L-type osteons ($\theta = \frac{\pi}{2}$) and oblique-type osteons ($\theta = i \cdot \frac{\pi}{12}$, $i \in \{1, 2, 3, 4, 5\}$). A parametrical custom-made ANSYS[®] environment macro was developed to assign different anisotropic properties to the lamellae. The FEM based model was constructed by means of hexahedral 8 nodes elements with linear shape functions generating a 364.800 elements and 380.182 nodes mesh with 4 elements in each lamella thickness as shown in Figure 6.15.

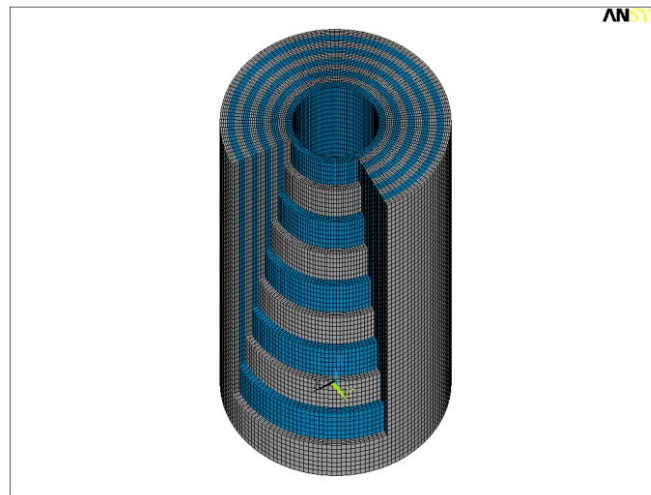


Figure 6.15

Finite Element Mesh of the osteons model proposed

The boundary conditions and the constraints imposed in the model reflect osteons physiological conditions. The osteon is constrained on the basis, simulating bone typical “packaging” at the microstructural level. A pressure is applied on the internal surface, simulating the interstitial pressure in the Haversian channel, while the pressure on the external surface is zero. Due to the trigonal microstructure, the applied pressure may induce the osteon rotation, but the presence of other osteons in the environment thwarts the osteon to move. This aspect is simulated by imposing zero tractions on the internal surface and a prescribed traction acting on the external one as boundary conditions.

The elastic constants of the osteon are evaluated employing the approach proposed in the Appendix. Table 6.3 reports the estimated bone matrix elastic constants of a single lamella for type L osteon (Yoon and Cowin 2008), used as starting point to evaluate the lamellar elastic constants for osteons with different values of the wrapping fibers angle.

E_1^m	16.4 GPa	ν_{12}^m	0.334
E_2^m	18.7 GPa	ν_{13}^m	0.237
E_3^m	22.8 GPa	ν_{21}^m	0.381
G_{12}^m	7.2 GPa	ν_{23}^m	0.247
G_{13}^m	7.1 GPa	ν_{31}^m	0.330
G_{23}^m	8.4 GPa	ν_{32}^m	0.301

Table 6.3

Estimated bone matrix elastic constants of a single lamella for type L osteon (Yoon and Cowin 2008)

The material parameters employed in the analysis are reported in Table 6.4 (Rémond et al., 2008).

K^P [m^2]	μ [Pas]	M [GPa]
10^{-18}	10^{-3}	40

Table 6.4

Material parameters employed in the FEM osteon analysis (Rémond et al., 2008)

Nature always optimizes structures to the specific functions to fulfill. The helicoidal pattern of the collagen fibers results, thus, a key element for understanding osteonal behavior. It will be shown that, together with the qualitative results, the apparently negligible difference in trigonal elastic constants with respect to the orthotropic ones produces significant differences in terms of poroelastic behavior and, then, in terms of biomechanical consequences. The resulting trigonal microstructure, in fact, is crucial for many aspect associated to osteons functions, such as fluid velocity magnitude. Figure 6.16 shows the different velocity profiles for the trigonal (blue line) and orthotropic model (red line).

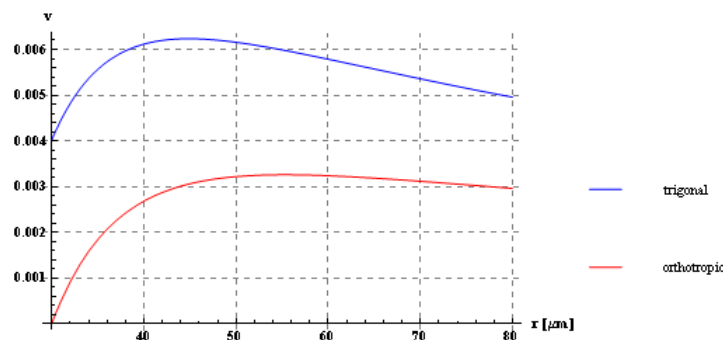


Figure 6.16

Comparison between velocity profiles for the trigonal (blue line) and the orthotropic model (red line)

The analyses of the velocity profiles reveals that the trigonal model appears to generate significant increases of velocity and, then, fluid shear stresses can be envisaged to activate mechanosensory in osteocytes and BMU activities as a cell response. Fluid shear stresses, in fact, play a crucial role in bone remodeling process. Fluid flow induces shear stress on cell membranes, a well-known stimulus for bone remodeling (Smit et al., 2002). Bone cells are particularly sensitive to fluid shear stress, which cause the release of different kinds of substances, ensuring the transmission of biochemical signals. Strain induced fluid flow results, thus, a powerful regulator of cells behavior and, so, a determinant factor in bone mechanotransduction. The bone mechanosensor cells, i.e. the osteocytes, are, in fact, actively stimulated by fluid shear stresses. Moreover, according to Darcy's Law, velocity is directly linked to pressure gradients. As a consequence, trigonal microstructure

determines also a significant increase in pressure gradients, responsible of fluid motion. However, trigonal model appears to generate also significant increases in volumetric strain gradients respect to the values obtained employing an orthotropic osteon model. This result has very important implications because strain gradients have been proposed as a possible remodeling stimulus (Gross et al. 1997).

Moreover, also volumetric strain is influenced by trigonal microstructure, as shown in Figure 6.17.

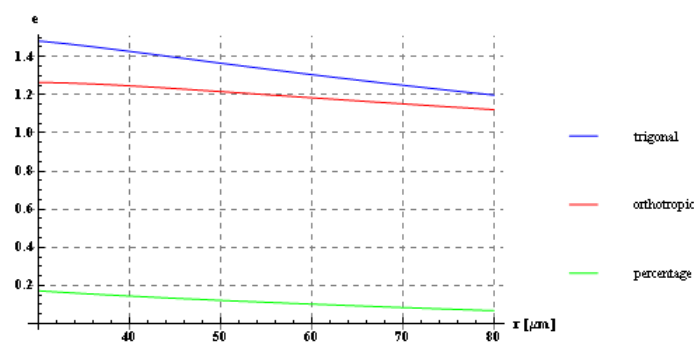


Figure 6.17

Comparison between volumetric strain profiles for the trigonal (blue line) and the orthotropic model (red line). Green line represents the percentage difference between the two models

In the volumetric strain profiles, in fact, a 20% increase can be highlighted by taking into account trigonal symmetry of the osteon. This can be a factor that participates to the well-known mechanism of strain amplification, here induced by the helicoidal arrangement of lamellae. In bone physiology, in fact, an important paradox exists, associated to the strain levels perceived in bone at the cellular level. Strains applied to the macroscopic bone are, in fact, smaller than the strains necessary to activate mechanotransduction processes and, thus, an amplification phenomenon should exist to ensure sufficient magnitude stimuli to bone cells (Cowin, 2002). An answer to this interesting paradox has not been found yet, even if different possible models have been proposed. Han et al. (Han et al., 2004) suggested, for example, a possible strain amplification mechanism associated to the fluid flow through the pericellular matrix at the lacunar-canalicular porosity level. However, our

results envisage that trigonal microstructure aids the strain amplification phenomenon, ensuring the strain levels needed to activate signaling in bone.

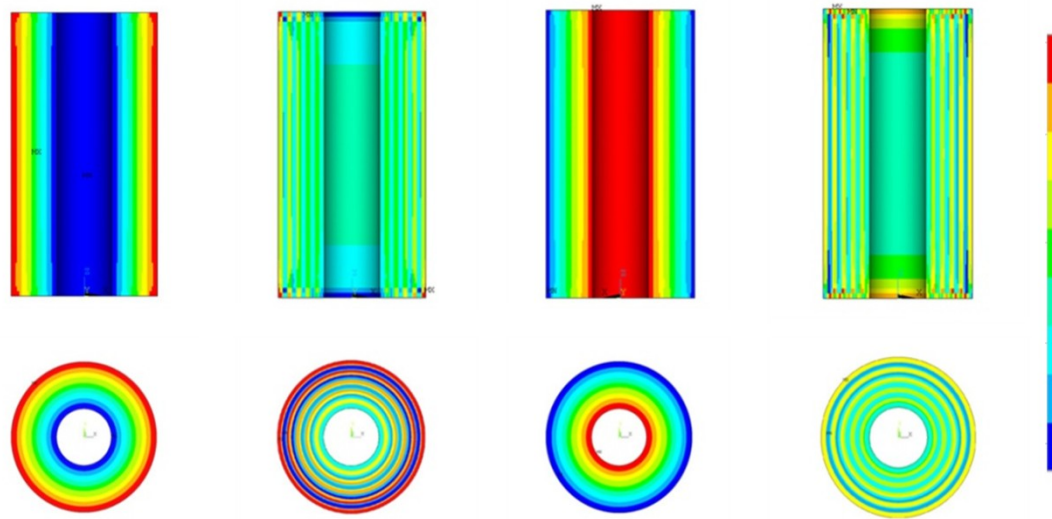


Figure 6.18

Variation of the volumetric strain in frontal and transverse osteon sections at one half

of the overall length for $\theta = \frac{\pi}{4}$

Figure 6.18 is, instead, a sketch of the variation of the volumetric strain in a frontal section, highlighting what happens in the longitudinal direction, and in a transverse section, emphasizing the behavior in the radial direction. These sections are obtained at one half of the overall osteon length for $\theta = \frac{\pi}{4}$.

Another important consequence of trigonal microstructure is associated to the change in sign and jumping at the interface of the in-plane shears, reported in Figure 6.19.

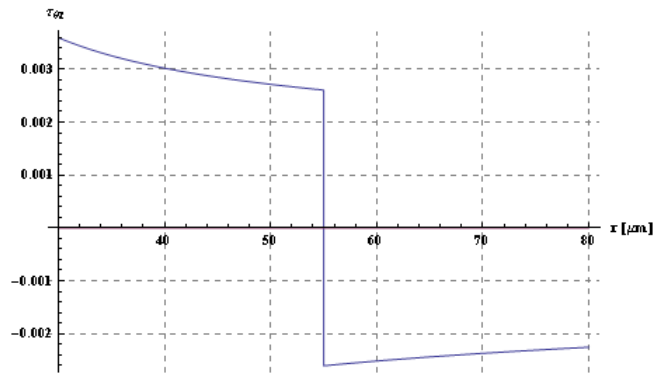


Figure 6.19

In plane-shears for the trigonal model

This phenomenon has important effects for what concerns osteocytes stimulation. Osteocytes are placed within niches of calcified matrix, the osteocyte lacunae, at the lamellae interfaces. As well known, different stimuli induce different pathways of biological signals. Moreover, mechanical loading induce also a rapid osteocytes production of nitric oxide and prostaglandin. It has been demonstrated that these substances are released as a consequence of the wall shear stresses (Bonucci, 2009). Finally, trigonal microstructure could also explain how osteons can act as microcracks barriers. Microdamage in bone occurs in the form of microcracks as a result of everyday cyclical loading activities (Mohsin et al. 2006) and it represents a stimulus for remodeling and repair. However, bone microstructure is also optimized to prevent microcracks propagation, slowing or altering their propagation direction and velocity. Microcracks, in fact, usually initiate in interstitial bone and stop when encountering cement lines, acting as weak interfaces, or somewhere within the osteon (Huang et al., 2006). Some authors proposed that the cement lines, surrounding osteons, can be seen as barriers to crack growth (O'Brien et al. 2007), because they can reduce the shear strength of osteonal bone. Moreover, also osteons themselves act as microcracks barriers. To this purpose, O'Brien et al. explained the osteons crack-stopping mechanism comparing them to composite materials. Also osteons, in fact, provide numerous sites for crack initiation, but the fibers act as barriers and prevent further growth. Osteons crack stoppers function can be material induced, i.e. associated to their intrinsic material properties, or stress induced, i.e. associated to the stress levels experienced. For what concerns the material properties, Gupta et al. (Gupta et al. 2006) considered osteons as mechanically modulated laminates of

mineralized collagen fibril layers, characterized by the alternance of a wide band of stiffer mineralized matrix with thin bands of softer material. This mechanical modulation provides an example of a natural crack stopping mechanism. Moreover, also the stiffness variation of single lamellae may serve as a crack trapping mechanism inside osteons, preventing cracks running in the interstitial bone from propagating toward the inner Haversian canal. Obviously, this kind of behavior is highlighted also when an orthotropic osteon model is employed. However, as just said before, the crack stopping behavior do not depend exclusively on the material properties, but also on stress intensity. Stresses profiles for trigonal and orthotropic osteons models have been investigated, with the purpose to show the consequences of the different trends on the crack stopping mechanism. For a mode I crack, propagating in the radial direction, the comparison between the hoop stresses profiles for the two models emphasizes that trigonal microstructure ensures a crack stopping behavior .

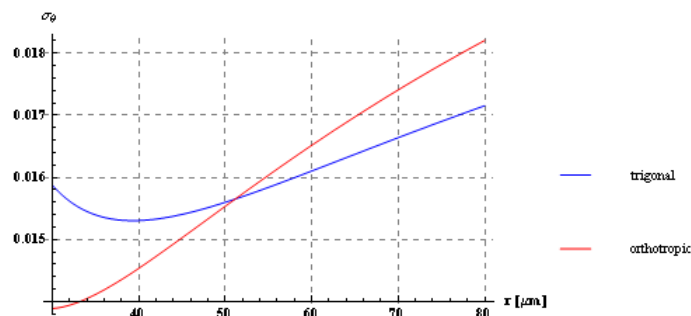


Figure 6.20

Comparison between the hoop stresses profiles for the trigonal (blue line) and the orthotropic model (red line)

As shown in Figure 6.20, the hoop stress gradients, in fact, decrease respect to the orthotropic case and, so, also the crack propagation velocity decreases. For a mode III crack, instead, referring to Figure 6.19, the analysis of shear stresses shows that an in-plane torque-induced shear stress kindles within the lamellar structure of trigonal osteons only, as a consequence of the kinematical constraint on the twisting angle, while this stress is zero for an orthotropic model. Moreover, in-plane shears change sign and jump passing from a lamella to the following one, revealing a stress induced crack stopping mechanism.

All these considerations support the idea that osteons trigonal microstructure is fundamental for bone adaptive and survival functions. Moreover, the trigonal microstructure ensures also the signaling far away the site of emission, creating a pathway for the fluid which can flow interlamellar and also in the osteon network. Figure 6.21 represents the organization of osteons in a cross section of a human femur. The different kinds of osteons showed in this image suggest that they are not only the bone answer to mechanical stimuli but also a system to optimize fluid flow and, thus, signaling in bone.

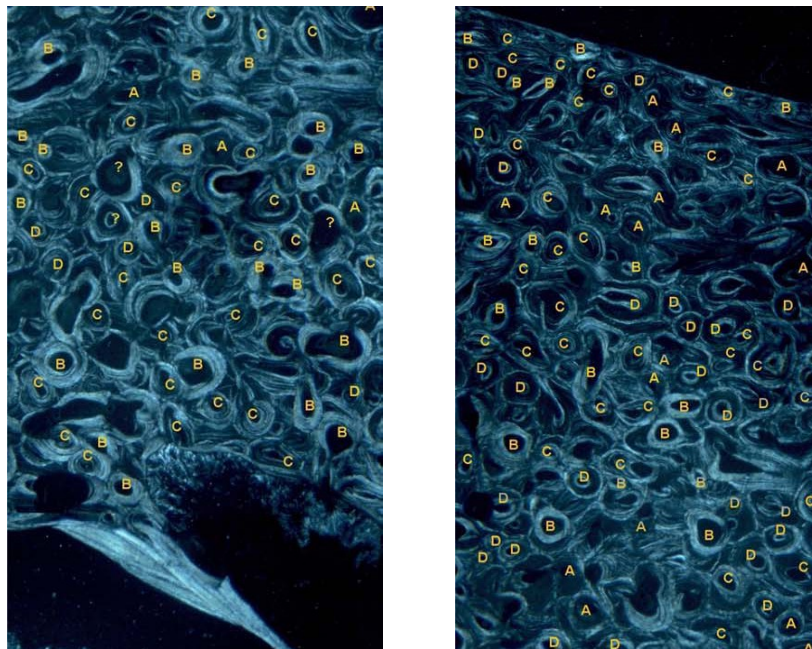


Figure 6.21

Osteons pattern in a human femur cross section. The inner region is reported on the left, while the outer one on the right. Dark osteons are indicated with A, Bright osteons with B, Alternating ones with C and hooped osteons, containing a thick portion of the peripheral boundary with a bright appearance under polarized light, with D

APPENDIX

A.1 Geometry and morphological features of osteons

Osteon is the chief structural unit of compact (cortical) bone, consisting of concentric bone layers called lamellae, which surround a long hollow passageway, the Haversian canal (Figure A.1a). Each lamella is constituted of arrays of collagen fibrils, more or less parallel to each other, embedded with mineral crystals (Figure A.1b).

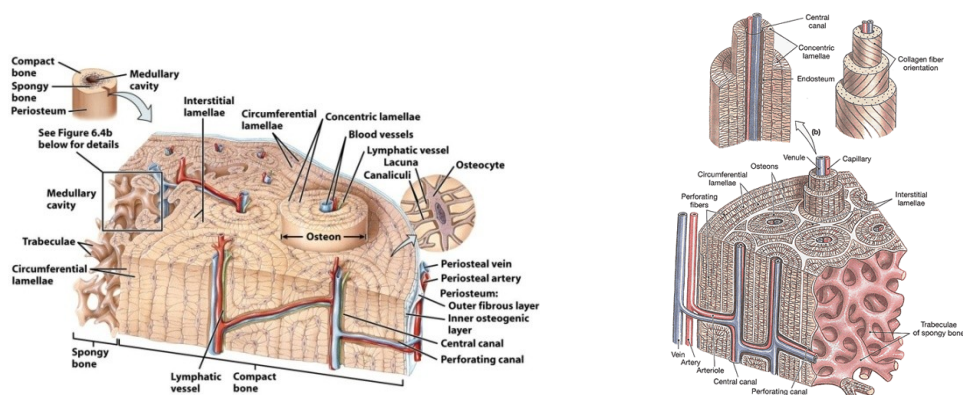


Figure A.1

- a) Osteons (Haversian System) in compact bone,
- b) Collagen fibers orientation in osteons (Figure from David Moyer)

The osteon looks like a cylinder with a diameter of about 200-250 μm , which runs roughly parallel to the long bone axis (Rho et al. 1998). The Haversian canal contains a nerve and small blood vessels responsible for the blood supply to osteocytes (individual bone cells). Osteoblasts form the lamellae sequentially, from the most external inward toward the Haversian canal. Some of the osteoblasts develop into osteocytes, each living within its own small space, or lacuna. Canaliculi are small tunnels connecting different lacunae which provide a pathway through which osteocytes can communicate information about

deformation states and, thus, coordinate bone adaptation. The composite structure of osteonal lamellae has interested researchers for the last 300 years and different theories have been proposed to discriminate them. One of the earliest theory arises from the work of Ascenzi and Bonucci ([Ascenzi and Bonucci 1968](#)) and it is based on the hypothesis that the collagen fibers in each lamella are almost parallel to each other and characterized by a preferential orientation within the lamella, which can change up to $\frac{\pi}{2}$ in the adjacent one.

This theory has inspired the osteons classification proposed by Martin et al. ([Martin et al. 1993](#)). Type T osteons present a marked transversal spiral course of fiber bundles in successive lamellae, type L osteons have, instead, a marked longitudinal spiral course of fiber bundles while type A osteons are characterized by fibers directions alternating by an angle of nearly $\frac{\pi}{2}$ between successive layers. Moreover, alternate osteons (osteons A) are

further divided in osteons characterized by the alternance of longitudinal lamellae with lamellae in which the fibers have a circular (or transverse with respect to the osteon axis) or an elliptical (or oblique with respect to the osteon axis) courses. Another osteons classification is linked to the different kind of images obtained with polarized light. Bright osteons are those in which the fibers are predominantly transversely or circumferentially oriented (osteons T), dark osteons are characterized by fibers oriented mostly longitudinally (osteons L). The third category is one in which the fiber orientation changes from lamella to lamella, producing a pattern of alternating light and dark layers within the osteon (osteons A) ([Martin et al. 1996](#)). Giraud-Guille ([Giraud-Guille 1988](#)) introduced the twisted plywood model, characterized by collagen fibrils running parallel to each other in a lamella, rotating continuously by a constant angle from plane to plane in an helicoidal structure, and the orthogonal plywood model, consisting, instead, of parallel collagen fibrils in a given plane, which can assume only one of the two directions out of phase of $\frac{\pi}{2}$

with each other. Giraud-Guille also underlined that the orthogonal plywood model closely remembers the type L and type T osteons from Ascenzi's model while the twisted plywood model can explain the type A osteons. Whereas both Ascenzi et al. and Giraud-Guille proposed models of collagen orientation assuming parallel fibers, Marotti and Muglia ([Marotti and Muglia 1988](#)) hypothesized that the structural differences in osteons are not associated to the collagen fibers orientation, but rather to different packing densities of collagen fibrils. They defined dense and loose packed lamella and so the light bands in

polarized light microscopy are associated to the loosely packed lamellae while the dark bands could be attributed to the densely packed lamellae. Recently, Ascenzi et al. (Ascenzi et al. 2006) have emphasized a dominant oblique orientation of the collagen fibers in osteonal lamellae respect to the osteonal axis by confocal microscopy. All these findings underline that osteonal microstructure complexity is due to the manifold and crucial functions it has to perform for bone survival and adaptation.

A.2 Derivation of the overall mechanical behavior of osteons from their microstructure

A.2.1 Local material properties at the lamella level

Osteonal lamellae are hierarchical composites of collagen fibers and mineral crystals, 3-7 μm thick (Rho et al. 1998). As already said, the lamellae can differ for the orientation of the collagen fibers and they represent the crucial determinant of the mechanical properties of the osteons. For this reason, many efforts have been made to determine experimentally and analytically the lamellae elastic constants. The osteonal lamellar structure seems to be the effect of the dynamic processes characterizing osteons formation, culminating with the collagen denseness increase from the cement line inward (Ardizzoni 2001). The nanoindentation method is very useful to study bone mechanical properties at macrostructural and microstructural level. Rho et al. (Rho et al. 1999) used this technique to examine variations in the lamellar properties as function of the distance from the centre of the osteon. They found that the elastic modulus and the hardness of the individual examined lamella decrease as function of the increasing distance from the centre of the osteon, confirming that the mechanical strength of osteonal lamellae increases from the cement line to the Haversian canal, as a consequence of their structure. Jasiuk and Ostoja-Starzewski (Jasiuk and Ostoja-Starzewski 2004) used a finite element model to compute anisotropic effective stiffness tensors and deformations of a single lamella as a function of the fibril volume fractions (or porosities), prescribed microgeometries, and fibril geometric and elastic properties. Yoon and Cowin (Yoon and Cowin 2008) estimated rather the elastic constants at a single lamella level, employing a micromechanical analytical approach. They determined the effective elastic constants for a single bone lamella,

assimilating it to a laminate, organized in three different hierarchical levels. They evaluated first the elastic constants for a mineralized collagen fibril, then for a collagen fiber and, finally, for a single lamella L , assuming an orthotropic behavior.

A.2.2 Overall material properties at the osteonal level

Osteons arouse the interest of the scientific community because they seem to be the key elements to understand bone mechanical, adaptive and fractures properties. As highlighted before, osteons play these crucial roles thanks to their intrinsic mechanical properties, built, above all, into the lamellar structure (Weiner et al. 1999). The nanoindentation method has been widely used to estimate also the osteons mechanical properties. (Gupta et al. 2006) combined the scanning nanoindentation and the scanning quantitative backscattered electron imaging to analyze the mechanical and chemical variations in osteons, finding a periodical variation of the indentation modulus within a single lamella, positively correlated to a lamellar modulation of the local mineral content. Hoc et al. (Hoc et al. 2006) noted the heterogeneity in the local bone elastic behavior employing nanoindentation tests. However, the identification of the anisotropic elastic constants of osteons based on nanoindentation is still an unresolved problem. Franzoso and Zysset (Franzoso and Zysset 2009) used a fabric-based approach to interpret the experimental data and to identify the elastic constants of the osteons, supposed orthotropic. The overall mechanical properties of osteons have been estimated also employing analytical and numerical models. From a mechanical point of view, cortical bone tissue can be seen as a multiscale deformable porous material, and an osteon as its basic structural unit (Cowin and Doty 2007). Poroelasticity theory, first developed by Biot, enables to analyze fluid–solid interaction and to model macroscopic averaged fluid flow through bone matrix and, so, it represents an important instrument in osteons modeling (Biot 1955). Many efforts were made to characterize osteons in terms of elasticity properties. Lenz et al. (Lenz et al. 2004) analyzed the mechanical behavior of a single osteon through a detailed finite element model, assuming an orthotropic behavior for the lamellae. Yoon and Cowin (Yoon and Cowin 2008) determined the anisotropic poroelastic constants of an osteon by micromechanical analysis. The drained and undrained elastic constants at the lacunar and canalicular porosity tissue levels have been estimated by using an effective moduli model

consisting of the periodic distribution of ellipsoidal cavities. A major conclusion of this study is that the estimated undrained and drained elastic constants exhibit only a slight difference and so the interstitial fluid presence can be neglected in the evaluation of the material properties. Moreover, elastic constants are mainly determined by the orientation of the collagen fibers in the lamellae. Motivated by this conclusions, the aim of this work is a mechanical characterization of osteons behavior, based on an homogenization technique. FGMs theory is applied to determine the lamellae elastic constants. The osteon is represented by a hollow cylinder, composed by concentric lamellae, positioned in an alternating way. In the previous works, an orthotropic symmetry is considered for the elasticity tensor. In this study, instead, the trigonal osteon behavior is highlighted to show the important biomechanical role played by off-diagonal elasticity tensor components, especially in governing the driving of interlamellar fluid flows and in regulating remodeling processes.

A.3 Sensitivity analysis of the out-of-diagonal block coefficients

Osteon is a roughly cylindrical structure, composed by concentric layers of collagen fibers, running parallel to each other to form an helicoidal pattern. This cylindrical structure, characterized by a central core, surrounded by various concentric arranged lamellae, constituted of water, hydroxiapatite and collagen fibers, remembers the FGMs structure and, thus, in the following, this theory will be applied to osteons to obtain the effective material properties for the lamellae. In literature, Functionally Graded Materials (FGMs) are treated as non-homogeneous materials with elastic moduli that vary continuously or in a piece-wise continuous manner along one spatial direction. These materials are characterized by variations in composition and structure gradually over volume, resulting in corresponding changes in the properties of the material. FGMs can be designed for specific functions and applications, but they can also be used to describe the behavior of biological structures exhibiting hierarchical helicoidal microstructures, as muscles, arterial walls and bone osteonal units. In this work, an homogenization is carried out on a FGMCs (Cylindrical Functionally Graded Materials) structure to determine the relationships between the elastic constants in an helicoidal reference system and in a cylindrical one. By

homogenizing over a single hollow phase with embedded helicoidal fibres, one obtains a cylindrically monoclinic anisotropy with plane of symmetry $\varphi-x_3$, where the modulus of the elastic coefficients in the cylindrical reference system $\{r, \varphi, x_3\}$, c_{ij}^{cyl} , explicitly depends upon the wrapping fibre angle θ , while the sign of some elastic moduli, such as c_{14}^{cyl} , c_{24}^{cyl} , c_{34}^{cyl} , c_{56}^{cyl} , depends on the sign of the wrapping fibre angle θ . Let us consider an helicoidal coordinate system (r, t, c) characterized by the unit vectors $(\mathbf{e}_r, \mathbf{e}_t, \mathbf{e}_c)$: the unit vector \mathbf{e}_t is tangent to the helix, the unit vector \mathbf{e}_r is perpendicular to \mathbf{e}_t and the unit vector \mathbf{e}_c is perpendicular to the plane individuated by the axis r and t . Let us consider a new coordinate cylindrical system (r, φ, x_3) , whose unit vectors are denoted by $(\mathbf{e}_r, \mathbf{e}_\varphi, \mathbf{e}_3)$. If the cylindrical system has the same origin of the helicoidal one, then, the unit vector \mathbf{e}_r is coincident for the two coordinate systems. The angle between the two unit vectors \mathbf{e}_t and \mathbf{e}_φ is identified by θ , equal to the angle between the two unit vectors \mathbf{e}_c and \mathbf{e}_3 . Employing Voigt notation, in the helicoidal coordinate system the elastic constant matrix is

$$\mathbf{c}^{hel} = \begin{bmatrix} c_{11}^{hel} & c_{12}^{hel} & c_{13}^{hel} & 0 & 0 & 0 \\ c_{12}^{hel} & c_{22}^{hel} & c_{23}^{hel} & 0 & 0 & 0 \\ c_{13}^{hel} & c_{23}^{hel} & c_{33}^{hel} & 0 & 0 & 0 \\ 0 & 0 & 0 & c_{44}^{hel} & 0 & 0 \\ 0 & 0 & 0 & 0 & c_{55}^{hel} & 0 \\ 0 & 0 & 0 & 0 & 0 & c_{66}^{hel} \end{bmatrix} \quad (3)$$

and, so, the material symmetry is, at most, orthotropic. With reference to (Mehrabadi et al. 1995), the elastic constant matrix in the cylindrical coordinate system can be written as:

$$\mathbf{c}^{cyl} = \begin{bmatrix} c_{11}^{cyl} & c_{12}^{cyl} & c_{13}^{cyl} & c_{14}^{cyl} & 0 & 0 \\ c_{12}^{cyl} & c_{22}^{cyl} & c_{23}^{cyl} & c_{24}^{cyl} & 0 & 0 \\ c_{13}^{cyl} & c_{23}^{cyl} & c_{33}^{cyl} & c_{34}^{cyl} & 0 & 0 \\ c_{14}^{cyl} & c_{24}^{cyl} & c_{34}^{cyl} & c_{44}^{cyl} & 0 & 0 \\ 0 & 0 & 0 & 0 & c_{55}^{cyl} & c_{56}^{cyl} \\ 0 & 0 & 0 & 0 & c_{56}^{cyl} & c_{66}^{cyl} \end{bmatrix} \quad (4)$$

and, so, the material symmetry is, at most, pseudo trigonal. By invoking the algebraic manipulation technique proposed in (Mehrabadi et al. 1995), the relationships between the

elastic constants in the cylindrical coordinate system, c_{jk}^{cyl} , and the elastic constants in the helicoidal coordinate system, c_{jk}^{hel} , are

$$\begin{aligned}
c_{11}^{cyl} &= c_{11}^{hel}, & c_{12}^{cyl} &= c_{12}^{hel} \cos^2 \theta + c_{13}^{hel} \sin^2 \theta, & c_{13}^{cyl} &= c_{13}^{hel} \cos^2 \theta + c_{12}^{hel} \sin^2 \theta, \\
c_{14}^{cyl} &= (c_{12}^{hel} - c_{13}^{hel}) \frac{\sin 2\theta}{2}, \\
c_{22}^{cyl} &= c_{22}^{hel} \cos^4 \theta + (c_{23}^{hel} + 2c_{44}^{hel}) \frac{\sin^2 2\theta}{2} + c_{33}^{hel} \sin^4 \theta, \\
c_{23}^{cyl} &= c_{23}^{hel} \cos^2 2\theta + \frac{1}{4} (c_{22}^{hel} + 2c_{23}^{hel} + c_{33}^{hel} - 4c_{44}^{hel}) \sin^2 2\theta, \\
c_{24}^{cyl} &= \frac{1}{4} [c_{22}^{hel} - c_{33}^{hel} + (c_{22}^{hel} - 2c_{23}^{hel} + c_{33}^{hel} - 4c_{44}^{hel}) \cos 2\theta] \sin 2\theta, \\
c_{33}^{cyl} &= c_{33}^{hel} \cos^4 \theta + (c_{23}^{hel} + 2c_{44}^{hel}) \frac{\sin^2 2\theta}{2} + c_{22}^{hel} \sin^4 \theta, \\
c_{34}^{cyl} &= \frac{1}{4} [c_{22}^{hel} - c_{33}^{hel} + (4c_{44}^{hel} - c_{33}^{hel} + 2c_{23}^{hel} - c_{22}^{hel}) \cos 2\theta] \sin 2\theta, \\
c_{44}^{cyl} &= c_{44}^{hel} \cos^2 2\theta + \frac{1}{4} (c_{22}^{hel} - 2c_{23}^{hel} + c_{33}^{hel}) \sin^2 2\theta, \\
c_{55}^{cyl} &= c_{55}^{hel} \cos^2 \theta + c_{66}^{hel} \sin^2 \theta, & c_{56}^{cyl} &= (c_{66}^{hel} - c_{55}^{hel}) \frac{\sin 2\theta}{2}, \\
c_{66}^{cyl} &= c_{55}^{hel} \sin^2 \theta + c_{66}^{hel} \cos^2 \theta
\end{aligned} \tag{5}$$

Synoptic Table A.1 highlights the results for the remarkable cases, say

$$\left\{ \theta \rightarrow 0, \theta \rightarrow \frac{\pi}{2}, \theta \rightarrow -\theta \right\}.$$

	c_{11}^{cyl}	c_{12}^{cyl}	c_{13}^{cyl}	c_{22}^{cyl}	c_{23}^{cyl}	c_{33}^{cyl}	c_{14}^{cyl}	c_{24}^{cyl}	c_{34}^{cyl}	c_{44}^{cyl}	c_{55}^{cyl}	c_{56}^{cyl}	c_{66}^{cyl}
$\theta \rightarrow 0$	c_{11}^{hel}	c_{12}^{hel}	c_{13}^{hel}	c_{22}^{hel}	c_{23}^{hel}	c_{33}^{hel}	0	0	0	c_{44}^{hel}	c_{55}^{hel}	0	c_{66}^{hel}
$\theta \rightarrow \frac{\pi}{2}$	c_{11}^{hel}	c_{13}^{hel}	c_{12}^{hel}	c_{33}^{hel}	c_{23}^{hel}	c_{22}^{hel}	0	0	0	c_{44}^{hel}	c_{66}^{hel}	0	c_{55}^{hel}
$\theta \rightarrow -\theta$	c_{11}^{cyl}	c_{12}^{cyl}	c_{13}^{cyl}	c_{22}^{cyl}	c_{23}^{cyl}	c_{33}^{cyl}	$-c_{14}^{cyl}$	$-c_{24}^{cyl}$	$-c_{34}^{cyl}$	c_{44}^{cyl}	c_{55}^{cyl}	$-c_{56}^{cyl}$	c_{66}^{cyl}

Table A.1

Remarkable cases for the values of the elastic constants

As highlighted in (Yoon and Cowin 2008), the elastic constants are mainly determined by the orientation of lamellae: the porosity does not significantly influence the elastic constants because the lacunar–canalicular porosity is only 5% of the total volume. The shape of lacunae may affect the elastic constants at the lacunar–canalicular porosity, but 2.6% porosity in total volume does not significantly modify them. Moreover, also the distribution of lacunae is not a crucial factor because the orientation of lacunae in the dilute distribution assumption is almost coincident with those in the periodic one. The goal of this section is, for these reasons, the mechanical characterization of the lamellae which constitute the osteon. The total number of lamellae is indicated with $2n$, while each lamella is indicated with m . The elastic constants tensor has the structure shown in (4), i.e.

$$\mathbf{C}_m = \begin{bmatrix} c_{11}^{cyl} & c_{12}^{cyl} & c_{13}^{cyl} & c_{14}^{cyl} & 0 & 0 \\ c_{12}^{cyl} & c_{22}^{cyl} & c_{23}^{cyl} & c_{24}^{cyl} & 0 & 0 \\ c_{13}^{cyl} & c_{23}^{cyl} & c_{33}^{cyl} & c_{34}^{cyl} & 0 & 0 \\ c_{14}^{cyl} & c_{24}^{cyl} & c_{34}^{cyl} & c_{44}^{cyl} & 0 & 0 \\ 0 & 0 & 0 & 0 & c_{55}^{cyl} & c_{56}^{cyl} \\ 0 & 0 & 0 & 0 & c_{56}^{cyl} & c_{66}^{cyl} \end{bmatrix} \quad (6)$$

The osteonal lamellae are wrapped around a central canal and sequential concentric lamellae have fiber orientations alternating with each other, spiraling around the central canal. The orientations envisaged in this kind of modeling are transverse (T-type osteon), longitudinal (L-type osteons) or oblique (Rho et al. 1998). Yoon and Cowin (Yoon and Cowin 2008) estimated the bone matrix elastic constants of a single lamella for L-type osteons, assuming an orthotropic osteons behavior. These values have been used as starting point to evaluate the lamellar elastic constants employing the relationships (5). To estimate the elastic constants in the cylindrical reference system, c_{jk}^{cyl} , it is necessary to know, before, the elastic constants in the helicoidal one, c_{jk}^{hel} . Collagen fibers in L-type osteons are parallel to the osteonal axes and, so, they are characterized by a right wrapping fibers angle.

First of all, the relationships between the elastic constants in the cylindrical and helicoidal reference systems are obtained by imposing $\theta = \frac{\pi}{2}$ in the (5):

$$\begin{aligned} c_{11}^{cyl} &= c_{11}^{hel}, c_{12}^{cyl} = c_{13}^{hel}, c_{13}^{cyl} = c_{12}^{hel}, c_{14}^{cyl} = 0, c_{22}^{cyl} = c_{33}^{hel}, c_{23}^{cyl} = c_{23}^{hel}, \\ c_{24}^{cyl} &= 0, c_{34}^{cyl} = 0, c_{33}^{cyl} = c_{22}^{hel}, c_{44}^{cyl} = c_{44}^{hel}, c_{55}^{cyl} = c_{66}^{hel}, c_{56}^{cyl} = 0, c_{66}^{cyl} = c_{55}^{hel} \end{aligned} \quad (7)$$

To evaluate the elastic constants in the helicoidal reference system, c_{jk}^{hel} , the values estimated in (Yoon and Cowin 2008) are replaced to the elastic constants in the cylindrical reference system, c_{jk}^{cyl} , in equations (7). The compounded helicoidal elastic constants are, finally, introduced in the equations (5) to determine the lamellar elasticity tensor for different values of the wrapping fibers angle. With the exception of T and L-types osteons, osteonal lamellae exhibit a pseudo-trigonal mechanical behavior because the off-diagonal components of the elasticity tensor cannot be neglected. To support this result, the components of the compliance tensor are estimated from the equations (5) and the pseudo trigonal compliance moduli, i.e. $s_{14}^{cyl}, s_{24}^{cyl}, s_{34}^{cyl}$, are compared with the off-diagonal coefficients within diagonal block. The moduli are plotted as function of the wrapping fibers angle, $\theta \in \left\{ -\frac{\pi}{2}, \frac{\pi}{2} \right\}$, as shown in Figure A.2.

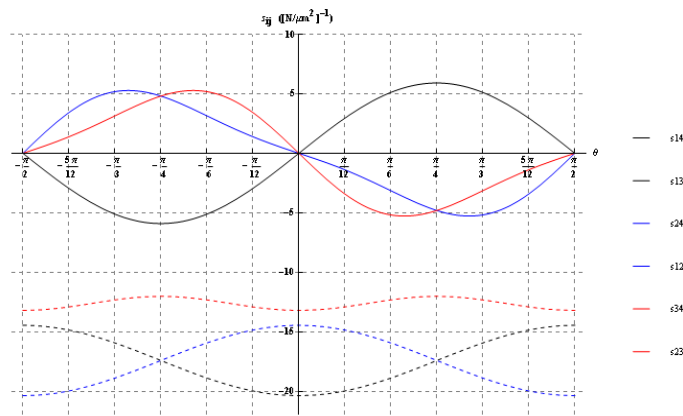


Figure A.2

Comparison between off-diagonal coefficients within diagonal block and pseudo-trigonal compliance moduli

All the values are expressed in $[N/\mu m^2]$. Continuous lines refer to pseudo trigonal compliance moduli, while dashed lines are associated to the minimum off-diagonal coefficients within diagonal block on the same row. To estimate the weight of the pseudo trigonal compliance moduli, also the percentage of the pseudo trigonal compliance moduli respect to the off-diagonal coefficients within diagonal block on the same row, has been evaluated, revealing that this ratio is of about 35% where the moduli reach their maximum value. s_{14}^{cyl} is maximum for $\theta = \frac{\pi}{4}$, while s_{24}^{cyl} and s_{34}^{cyl} for about $\frac{7\pi}{24}$ and $\frac{5\pi}{24}$, respectively.

A.4 The role in mechanoregulation of osteonal spiral twisting

Once the elastic constants of the lamellae have been estimated, the overall mechanical properties of the osteons can be determined through an homogenization technique. The homogenized elasticity tensor can be evaluated as follows:

$$\bar{\mathbf{C}} = \sum_{i=1}^{2n} \gamma^{(i)} \mathbf{C}^{(i)} \quad (8)$$

where $\gamma^{(i)}$ is the volumetric fraction of the i -th lamella, defined as:

$$\gamma^{(i)} = \frac{(R_i^2 - R_{(i-1)}^2)}{(R_{out}^2 - R_{int}^2)} \quad (9)$$

where R_{out} is the outer osteon radius, while R_{int} is the inner one (i.e. the radius of the Haversian canal).

The volumetric fractions defined in the equations (9) are subjected to the constraint

$$\sum_{i=1}^{2n} \gamma^{(i)} = 1 \quad (10)$$

where $2n$ is the total number of lamellae. Moreover, the peculiar feature of the FGM osteon model proposed is that two adjacent lamellae are characterized by the same wrapping fibers angle θ , but opposite in sign. The FGM osteons model proposed shows that the collagen fibers organization, arranged in an alternative way, is the key element to carry on the mechanical functions at the osteons scale. According to (6), in fact, each lamella has a trigonal behavior and, so, also the off-diagonal components have to be considered. By invoking the equation (8) and (5), the overall elasticity tensor is evaluated as

$$\bar{c}_{jk}^{cyl} = \sum_{i=1}^{2n} \gamma^{(i)} c_{jk}^{cyl(i)} \quad (11)$$

where \bar{c}_{jk}^{cyl} are the homogenized elastic constants in the cylindrical coordinate system. As shown in Table A.1, two adjacent lamellae, characterized by alternative angle values, have the off-diagonal elastic constants all equal but opposite in sign. Their contribution in (8) will be, however, different because their weights, i.e. the volumetric fractions defined in (9), are different. As highlighted, in fact, by Gupta et al. (Gupta et al. 2006), the lamellae thickness is almost the same for each lamella and, so, the volumetric fractions will be all different. The volumetric fractions of each lamella can be determined employing the relationship (9). If the lamella thickness is represented by t , and the difference $R_{out}^2 - R_{int}^2$ by A , then the volumetric fractions $\gamma^{(i)}$ can be expressed as

$$\gamma^{(i)} = \frac{(R_{int} + i \cdot t)^2 - (R_{int} + (i-1)t)^2}{A} = \frac{t[2R_{int} + t(2i-1)]}{A} \quad \forall i \in \{1, 2, \dots, 2n\} \quad (12)$$

where the volumetric fraction of the first inner lamella can be written as $\gamma^{(1)} = \frac{t}{A}(2R_{int} + t)$.

The volumetric fraction of the lamellae (i+1)-th is greater than that of the lamellae i-th.

The difference between the volumetric fractions is given by:

$$\gamma^{(i+1)} - \gamma^{(i)} = \frac{2t}{A} > 0 \quad (13)$$

The equation (11) can be rearranged as

$$\bar{c}_{jk}^{cyl} = f_{jk}(n) c_{jk}^{cyl}(c_{jk}^{hel}, \theta) \quad (14)$$

By applying the previous assumption, the following property for the elastic constant $c_{jk}^{cyl}(c_{jk}^{hel}, \theta)$ of the lamellae is determined:

$$\begin{cases} c_{jk}^{cyl(i)}(\theta > 0) = c_{jk}^{cyl(i+1)}(\theta < 0) & \forall j, k \in \{1, 2, 3\}, \\ c_{jj}^{cyl(i)}(\theta > 0) = c_{jj}^{cyl(i+1)}(\theta < 0) & \forall j \in \{4, 5, 6\}, \\ c_{j4}^{cyl(i)}(\theta > 0) = -c_{j4}^{cyl(i+1)}(\theta < 0) & \forall j \in \{1, 2, 3\}, \\ c_{56}^{cyl(i)}(\theta > 0) = -c_{56}^{cyl(i+1)}(\theta < 0) \end{cases} \quad \forall i \in \{1, 2, \dots, (2n-1)\} \quad (15)$$

The function $f_{jk}(n)$ assume the follows form:

$$\begin{aligned} f_{jk}(n) &= [4nt(R_{int} + nt)] / A \quad \forall j, k \in \{1, 2, 3\}, \\ f_{jj}(n) &= [4nt(R_{int} + nt)] / A \quad \forall j \in \{4, 5, 6\}, \\ f_{j4}(n) &= \pm 2nt^2 / A \quad \forall j \in \{1, 2, 3\}, \\ f_{56}(n) &= \pm 2nt^2 / A, \end{aligned} \quad (16)$$

The sign of the functions $f_{j4}(n)$, $f_{56}(n)$ depend on the fibres wrapping angle. In particular, if the first lamella is characterized by a wrapping fibres angle $\theta > 0$, the sign of these functions is negative and viceversa. These function, thus, depend exclusively on the number of lamellae because, as already highlighted, the lamella thickness t and the radius R_{int} are equal for all the lamellae.

It is interesting to note that, if the volumetric fractions are the same for all the lamellae, the following relationships subsist :

$$\begin{aligned}
\gamma^{(i)} &= R_{\text{int}}^2 / A & \forall i \in \{1, 2, \dots, 2n\} \\
f_{jk}(n) &= [2n R_{\text{int}}^2] / A & \forall j, k \in \{1, 2, 3\}, \\
f_{jj}(n) &= [2n R_{\text{int}}^2] / A & \forall j \in \{4, 5, 6\}, \\
f_{j4}(n) &= f_{56}(n) = 0 & \forall j \in \{1, 2, 3\},
\end{aligned} \tag{17}$$

The homogenized overall elastic constants can be, therefore, written explicitly as function of the number of lamellae and of the elastic constants in the helicoidal reference system.

$$\begin{aligned}
\bar{c}_{11}^{\text{cyl}} &= \frac{4nt(R_{\text{int}} + nt)}{A} \cdot c_{11}^{\text{hel}}, \quad \bar{c}_{12}^{\text{cyl}} = \frac{4nt(R_{\text{int}} + nt)}{A} \cdot (c_{12}^{\text{hel}} \cos^2 \theta + c_{13}^{\text{hel}} \sin^2 \theta), \\
\bar{c}_{13}^{\text{cyl}} &= \frac{4nt(R_{\text{int}} + nt)}{A} \cdot (c_{13}^{\text{hel}} \cos^2 \theta + c_{12}^{\text{hel}} \sin^2 \theta), \\
\bar{c}_{22}^{\text{cyl}} &= \frac{4nt(R_{\text{int}} + nt)}{A} \cdot (c_{22}^{\text{hel}} \cos^4 \theta + 2(c_{23}^{\text{hel}} + 2c_{44}^{\text{hel}}) \sin^2 \theta \cos^2 \theta + c_{33}^{\text{hel}} \sin^4 \theta), \\
\bar{c}_{23}^{\text{cyl}} &= \frac{4nt(R_{\text{int}} + nt)}{A} \cdot (c_{23}^{\text{hel}} \cos^2 2\theta + (c_{22}^{\text{hel}} + 2c_{23}^{\text{hel}} + c_{33}^{\text{hel}} - 4c_{44}^{\text{hel}}) \sin^2 \theta \cos^2 \theta), \\
\bar{c}_{33}^{\text{cyl}} &= \frac{4nt(R_{\text{int}} + nt)}{A} \cdot (c_{33}^{\text{hel}} \cos^4 \theta + 2(c_{23}^{\text{hel}} + 2c_{44}^{\text{hel}}) \sin \theta \cos \theta + c_{22}^{\text{hel}} \sin^4 \theta), \\
\bar{c}_{44}^{\text{cyl}} &= \frac{4nt(R_{\text{int}} + nt)}{A} \cdot (c_{22}^{\text{hel}} - 2c_{23}^{\text{hel}} + c_{33}^{\text{hel}} + 4c_{44}^{\text{hel}} - (c_{22}^{\text{hel}} - 2c_{23}^{\text{hel}} + c_{33}^{\text{hel}} - 4c_{44}^{\text{hel}}) \cos 4\theta), \\
\bar{c}_{55}^{\text{cyl}} &= \frac{4nt(R_{\text{int}} + nt)}{A} \cdot (c_{55}^{\text{hel}} \cos^2 \theta + c_{66}^{\text{hel}} \sin^2 \theta), \\
\bar{c}_{66}^{\text{cyl}} &= \frac{4nt(R_{\text{int}} + nt)}{A} \cdot (c_{66}^{\text{hel}} \cos^2 \theta + c_{55}^{\text{hel}} \sin^2 \theta), \\
\bar{c}_{14}^{\text{cyl}} &= \frac{nt^2}{A} (-c_{12}^{\text{hel}} + c_{13}^{\text{hel}}) \sin 2\theta, \\
\bar{c}_{24}^{\text{cyl}} &= -\frac{nt^2}{2A} [c_{22}^{\text{hel}} - c_{33}^{\text{hel}} + (c_{22}^{\text{hel}} - 2c_{23}^{\text{hel}} + c_{33}^{\text{hel}} - 4c_{44}^{\text{hel}}) \cos 2\theta] \sin 2\theta, \\
\bar{c}_{34}^{\text{cyl}} &= \frac{nt^2}{A} [-c_{22}^{\text{hel}} + c_{33}^{\text{hel}} + (c_{22}^{\text{hel}} - 2c_{23}^{\text{hel}} + c_{33}^{\text{hel}} - 4c_{44}^{\text{hel}}) \cos 2\theta] \sin 2\theta, \\
\bar{c}_{56}^{\text{cyl}} &= \frac{nt^2}{A} (c_{55}^{\text{hel}} - c_{66}^{\text{hel}}) \sin 2\theta
\end{aligned} \tag{18}$$

Table A.2 reports the estimated values of the compliance moduli for different types of osteons, expressed in $[N / \mu m^2]$. The osteon is supposed to be constituted by two phases, (1) and (2), characterized by the thickness t , while the inner radius, R_{int} , is $2t$. l_1 and l_2 indicate the local values of the compliance moduli for the two phases, while h refers to the homogenized estimate of the compliance moduli, evaluated employing the relationship (8). Different kinds of osteons have been examined and a new classification is introduced, based on the differences in the mechanical properties induced by the wrapping fibers angle. The first three types of osteons, i.e. L-type (L), T-type (T) and circular A-type osteons (AC), belong to the category of the “orthotropic osteons” because the local and homogenized pseudo trigonal compliance moduli vanish and the mechanical behavior results, thus, orthotropic. Besides, there is not a clean separation between the three macro categories individuated. AC osteons are, in fact, a particular case of the category of the “orthogonal plywood osteons”, characterized by a right angle between the directions of two adjacent lamellae. When the wrapping fibers angle is different from $\theta = 0$ or $\theta = \frac{\pi}{2}$, all the local and homogenized compliance moduli are different from zero and, so, the mechanical behavior turns out to be pseudo-trigonal. The last category includes the “osteons with alternate angles”, that is to say that two adjacent lamellae are characterized by equal wrapping fibers angles, but opposite in sign. Also for this category there is an intersection with the previous one for $\theta = \frac{\pi}{4}$. The pseudo trigonal behavior outcrops also for “alternate angles osteons”, underling that the overall orthotropic osteons behavior proposed by Franzoso and Zysset (Franzoso and Zysset 2009) and Yoon and Cowin (Yoon and Cowin 2008) can be used to justify exclusively the behavior of the first category of osteons. Moreover, the homogenization technique proposed in this paper furnishes an easier way to estimate the elastic constants.

		ORTHOGONAL PLYWOOD												ALTERNATE ANGLES								
		ORTHOTROPIC OSTIONS						AL														
		E_1	E_2	ν_{12}	ν_{21}	G_{12}	E_1	E_2	ν_{12}	ν_{21}	G_{12}	E_1	E_2	ν_{12}	ν_{21}	G_{12}	E_1	E_2	ν_{12}	ν_{21}	G_{12}	
S_{11}	60.98	60.98	60.98	60.98	60.98	60.98	60.98	60.98	60.98	60.98	60.98	60.98	60.98	60.98	60.98	60.98	60.98	60.98	60.98	60.98	60.98	60.98
S_{12}	-20.37	-20.37	-14.46	-14.46	-14.46	-16.68	-15.94	-18.89	-17.79	-17.05	-17.42	-17.42	-17.42	-17.42	-17.42	-17.42	-17.42	-17.42	-17.42	-17.42	-17.42	-17.42
S_{13}	-14.46	-14.46	-20.37	-20.37	-14.46	-20.37	-18.15	-18.89	-15.94	-17.05	-17.79	-17.42	-17.42	-17.42	-17.42	-17.42	-17.42	-17.42	-17.42	-17.42	-17.42	-17.42
S_{22}	53.48	53.48	43.86	43.86	43.86	47.47	45.38	50.19	48.39	50.19	45.38	47.49	47.49	47.49	47.49	47.49	47.49	47.49	47.49	47.49	47.49	47.49
S_{23}	-13.21	-13.21	-13.21	-13.21	-13.21	-13.21	-13.21	-13.21	-13.21	-13.21	-13.21	-13.21	-13.21	-13.21	-13.21	-13.21	-13.21	-13.21	-13.21	-13.21	-13.21	-13.21
S_{33}	43.86	43.86	53.48	53.48	53.48	49.87	50.19	45.38	47.19	45.38	50.19	48.39	47.49	47.49	47.49	47.49	47.49	47.49	47.49	47.49	47.49	47.49
S_{44}	119.05	119.05	119.05	119.05	119.05	119.05	119.05	119.05	119.05	119.05	119.05	119.05	119.05	119.05	119.05	119.05	119.05	119.05	119.05	119.05	119.05	119.05
S_{55}	140.85	140.85	138.89	138.89	140.85	138.89	139.62	139.38	139.74	139.38	140.36	139.99	140.36	139.87	139.87	139.87	139.87	139.87	139.87	139.87	139.87	139.87
S_{66}	138.89	138.89	140.85	140.85	138.89	140.85	140.11	140.36	139.38	139.74	140.36	139.99	140.36	139.87	139.87	139.87	139.87	139.87	139.87	139.87	139.87	139.87
S_{14}	0.00	0.00	0.00	0.00	0.00	0.00	0.00	0.00	0.00	0.00	0.00	0.00	0.00	0.00	0.00	0.00	0.00	0.00	0.00	0.00	0.00	0.00
S_{15}	0.00	0.00	0.00	0.00	0.00	0.00	0.00	0.00	0.00	0.00	0.00	0.00	0.00	0.00	0.00	0.00	0.00	0.00	0.00	0.00	0.00	0.00
S_{16}	0.00	0.00	0.00	0.00	0.00	0.00	0.00	0.00	0.00	0.00	0.00	0.00	0.00	0.00	0.00	0.00	0.00	0.00	0.00	0.00	0.00	0.00
S_{24}	0.00	0.00	0.00	0.00	0.00	0.00	0.00	0.00	0.00	0.00	0.00	0.00	0.00	0.00	0.00	0.00	0.00	0.00	0.00	0.00	0.00	0.00
S_{25}	0.00	0.00	0.00	0.00	0.00	0.00	0.00	0.00	0.00	0.00	0.00	0.00	0.00	0.00	0.00	0.00	0.00	0.00	0.00	0.00	0.00	0.00
S_{26}	0.00	0.00	0.00	0.00	0.00	0.00	0.00	0.00	0.00	0.00	0.00	0.00	0.00	0.00	0.00	0.00	0.00	0.00	0.00	0.00	0.00	0.00

Table A.2

Estimated compliance moduli for different kinds of osteons

A.5 Analytical poroelastic solution for a solid FGMC composed by two phases under radial pressure

An analytical poroelastic solution is determined for an osteon, represented with a solid FGMC, constituted by two hollow cylinder phases, (1) and (2). The two phases have the same thickness, t , the internal radius is denoted with R_{int} and the solid is loaded with a radial pressure on the external surface and with the pressure of the interstitial fluid on the internal surface. With reference to the cylindrical coordinate system $\{r, \varphi, x_3\}$, the equilibrium equations in each phase, in the absence of body forces, are given by

$$\begin{aligned}\sigma_{rr,r} + r^{-1}\sigma_{r\varphi,\varphi} + \sigma_{r3,3} + r^{-1}(\sigma_{rr} - \sigma_{\varphi\varphi}) &= 0 \\ \sigma_{r\varphi,r} + r^{-1}\sigma_{\varphi\varphi,\varphi} + \sigma_{\varphi 3,3} + 2r^{-1}\sigma_{r\varphi} &= 0 \\ \sigma_{r3,r} + r^{-1}\sigma_{\varphi 3,\varphi} + \sigma_{33,3} + r^{-1}\sigma_{r3} &= 0\end{aligned}\quad (19)$$

The relationships between the strains ε_{ij} and the displacements u_i are

$$\begin{aligned}\varepsilon_{rr} &= u_{r,r}, \quad \varepsilon_{\varphi\varphi} = r^{-1}(u_{\varphi,\varphi} + u_r), \quad \gamma_{r\varphi} = r^{-1}(u_{r,\varphi} + r u_{\varphi,r} - u_\varphi) \\ \varepsilon_{33} &= u_{3,3}, \quad \gamma_{r3} = u_{3,r} + u_{r,3}, \quad \gamma_{\varphi 3} = r^{-1}(u_{3,\varphi} + r u_{\varphi,3})\end{aligned}\quad (20)$$

In a saturated porous medium the strain $\boldsymbol{\varepsilon}$ is linearly related, not only to the stress $\boldsymbol{\sigma}$, but also to the fluid pressure p in the fluid-filled pores; thus, one can write the strain–stress–pore pressure relation in a generic phase (i) as

$$\boldsymbol{\sigma}^{(i)} = \mathbf{C}^{(i)} : \boldsymbol{\varepsilon}^{(i)} - \mathbf{A}^{(i)} p^{(i)} \quad (21)$$

where the superscript (i) denotes the elastic modulus of the generic i -th phase of the FGMC; $\mathbf{C}^{(i)}$ is elastic constants matrix; $p^{(i)}$ is the pore pressure and $\mathbf{A}^{(i)}$ is the Biot effective stress coefficient tensor. The equation (21) includes the effect of the pore pressure. If the pore pressure is zero, the equation (21) will coincide with the anisotropic Hooke's law.

Moreover, the pressure $p^{(i)}$ satisfies the diffusion equation for the pressure field in poroelastic problems. In the hypothesis of isotropy respect to the permeability, $\mathbf{K}_p = \kappa \mathbf{I}$, where κ is a constant. In the case of incompressible steady-state poroelastic problem, the diffusion equation becomes

$$p_{,rr}^{(i)} + r^{-1} p_{,r}^{(i)} + r^{-2} p_{,\varphi\varphi}^{(i)} + p_{33}^{(i)} = 0 \quad (22)$$

In an elastic axial-symmetrical problem, the displacement solution and pore pressure for the two phases do not depend on the anomaly and, thus, the following expressions can be considered

$$\begin{aligned} u_r^{(i)} &= u_r^{(i)}(r, x_3), & u_\varphi^{(i)} &= u_\varphi^{(i)}(r, x_3), \\ u_3^{(i)} &= u_3^{(i)}(r, x_3) & p^{(i)} &= p^{(i)}(r, x_3) \quad \forall i \in \{1, 2\} \end{aligned} \quad (23)$$

It is possible to prove that the displacement field solution in this poroelastic steady-state problem is given by

$$\begin{cases} u_r^{(i)} = C_1^{(i)} r^{\lambda^{(i)}} + C_2^{(i)} r^{-\lambda^{(i)}} + \left[\frac{C_4^{(i)}}{c_{11}^{(i)} - c_{22}^{(i)}} + h_1^{(i)} \varepsilon_0 \right] r + h_2^{(i)} \phi r^2 \\ u_\varphi^{(i)} = \phi r x_3, & u_3^{(i)} = \varepsilon_0 x_3, & p^{(i)} = C_3^{(i)} + C_4^{(i)} \log r \end{cases} \quad \forall i \in \{1, 2\} \quad (24)$$

where $C_1^{(i)}, C_2^{(i)}, C_3^{(i)}, C_4^{(i)}, \varepsilon_0, \phi$ are the integration constants and the coefficients $h_1^{(i)}, h_2^{(i)}, \lambda^{(i)}$ are given by

$$h_1^{(i)} = (c_{23}^{(i)} - c_{13}^{(i)}) / (c_{11}^{(i)} - c_{22}^{(i)}), \quad h_2^{(i)} = (c_{24}^{(i)} - 2c_{14}^{(i)}) / (4c_{11}^{(i)} - c_{22}^{(i)}), \quad \lambda^{(i)} = \sqrt{c_{22}^{(i)} / c_{11}^{(i)}},$$

In particular, $\phi^{(i)}$ and $\varepsilon_0^{(i)}$ are the two coefficients representing the unit wrapping angle and axial strain, respectively.

The strain components are, then, evaluated by applying the relationships between the strains ε_{ij} and the displacements (20),

$$\begin{aligned}\varepsilon_{rr}^{(i)} &= \frac{C_4^{(i)} + h_1^{(i)}}{c_{11}^{(i)} - c_{22}^{(i)}} + C_1^{(i)} \lambda^{(i)} r^{\lambda^{(i)}-1} - C_2^{(i)} \lambda^{(i)} r^{-(1+\lambda^{(i)})} + 2h_2^{(i)} \phi r, \\ \varepsilon_{\phi\phi}^{(i)} &= \frac{C_4^{(i)} + h_1^{(i)}}{c_{11}^{(i)} - c_{22}^{(i)}} + C_1^{(i)} \lambda^{(i)} r^{\lambda^{(i)}-1} - C_2^{(i)} \lambda^{(i)} r^{-(1+\lambda^{(i)})} + 2h_2^{(i)} \phi r, \\ \varepsilon_{33}^{(i)} &= \varepsilon_0^{(i)}, \quad \gamma_{\phi 3}^{(i)} = \phi r, \quad \gamma_{r3}^{(i)} = \gamma_{r\phi}^{(i)} = 0,\end{aligned}\tag{25}$$

In the hypothesis of linear elastic behavior for the materials and of perfect contact at the cylindrical interfacial boundaries (no de-lamination or friction phenomena), the satisfaction of both the equilibrium and the compatibility equations at the boundary surfaces between two adjacent phases need to be imposed. The total unknown parameters to determine result ten and can be summarized as follows

$$C_1^{(1)}, C_2^{(1)}, C_3^{(1)}, C_4^{(1)}, C_1^{(2)}, C_2^{(2)}, C_3^{(2)}, C_4^{(2)}, \varepsilon_0, \phi\tag{26}$$

Their number is equal to the number of the algebraic equations to solve. First of all, the two equilibrium and compatibility equations at the interfaces are written as

$$\begin{cases} u_{rr}^{(1)}(r = R_{\text{int}} + t) = u_{rr}^{(2)}(r = R_{\text{int}} + t) \\ \sigma_{rr}^{(1)}(r = R_{\text{int}} + t) = \sigma_{rr}^{(2)}(r = R_{\text{int}} + t) \end{cases}\tag{27}$$

The Cauchy equilibrium equations on the external cylindrical boundary surface are given by

$$\begin{cases} \sigma_{rr}^{(1)}(r = R_{\text{int}}) = \mathbf{t}_{\text{int}} \\ \sigma_{rr}^{(2)}(r = R_{\text{int}} + 2t) = \mathbf{t}_{\text{ext}} \end{cases}\tag{28}$$

where \mathbf{t}_{int} and \mathbf{t}_{ext} are the radial load on internal and external lateral surface of the cylinder, respectively. Moreover, the displacement components along the x_3 -direction and hope

direction on both basis are equal to zero. As a consequence, the integration constants ε_0, ϕ are equal to zero.

Finally, it remains to consider the equilibrium equations in x_3 -direction and about x_3 -direction on one of the basis. Therefore, without loss of generality, for $x_3 = 0$ it can be written

$$\begin{cases} \int_0^{2\pi} \int_R^{R+t} \sigma_{33}^{(1)}(x_3 = 0) r dr d\vartheta + \int_0^{2\pi} \int_{R+t}^{R+2t} \sigma_{33}^{(2)}(x_3 = 0) r dr d\vartheta = F_3, \\ \int_0^{2\pi} \int_R^{R+t} \sigma_{\vartheta 3}^{(1)}(x_3 = 0) r^2 dr d\vartheta + \int_0^{2\pi} \int_{R+t}^{R+2t} \sigma_{\vartheta 3}^{(2)}(x_3 = 0) r^2 dr d\vartheta = \mathfrak{M}_t \end{cases} \quad (29)$$

where F_3 and \mathfrak{M}_t are the total axial force and the torque applied at $x_3 = 0$, respectively.

The pore pressure $p^{(i)}$ in both phases satisfies the following boundary conditions

$$\begin{cases} p^{(1)}(r = R_{\text{int}}) = p_{\text{int}}, \\ p^{(2)}(r = R_{\text{int}} + 2t) = p_{\text{ext}}, \\ p^{(1)}(r = R_{\text{int}} + t) = p^{(2)}(r = R_{\text{int}} + t), \\ p_{,r}^{(1)}(r = R_{\text{int}} + t) = p_{,r}^{(2)}(r = R_{\text{int}} + t), \end{cases} \quad (30)$$

where $p_{\text{int}}, p_{\text{ext}}$ are the pore pressure on internal and external lateral surface of the cylinder, respectively. By solving the boundary conditions (30), the integration constants $C_3^{(1)}, C_4^{(1)}, C_3^{(2)}, C_4^{(2)}$ result

$$\begin{aligned} C_3^{(1)} = C_3^{(2)} &= p_{\text{int}} - \frac{p_{\text{ext}} - p_{\text{int}}}{\log(R_{\text{int}} + 2t) - \log(R_{\text{int}})}, \\ C_4^{(1)} = C_4^{(2)} &= + \frac{p_{\text{ext}} - p_{\text{int}}}{\log(R_{\text{int}} + 2t) - \log(R_{\text{int}})}, \end{aligned} \quad (31)$$

Let us assume that the solid matrix of the porous material and the fluid are incompressible. Then, the Biot effective stress coefficient tensor $\mathbf{A}^{(i)}$ is given by the identity matrix.

By applying the relationship (21) and the notation of Voigt, the stress vector is obtained as

$$\begin{aligned} \sigma_k^{(i)} = & C_1^{(i)} \left(c_{2k}^{(i)} + c_{1k}^{(i)} \lambda^{(i)} \right) r^{\lambda^{(i)}-1} + C_2^{(i)} \left(c_{2k}^{(i)} - c_{1k}^{(i)} \lambda^{(i)} \right) r^{-(1+\lambda^{(i)})} + \\ & -C_3^{(i)} + C_4^{(i)} \left(\frac{c_{1k}^{(i)} + c_{2k}^{(i)}}{c_{11}^{(i)} - c_{22}^{(i)}} - \log r \right) \quad \forall k \in \{1, 2, \dots, 6\} \end{aligned} \quad (32)$$

The parameters $C_1^{(1)}, C_2^{(1)}, C_1^{(2)}, C_2^{(2)}$ are, instead, determined by solving the algebraic system constituted by the equations (27)-(28). For the sake of simplicity, the two hollow phases are supposed to be transversally isotropic in the helicoidal coordinate system with plane of isotropy r - c . Moreover, the following relationships between the elastic constants are considered

$$\begin{aligned} E_{rr} = E_{cc} = E, \quad E_{tt} = \alpha E, \quad \nu_{rt} = \nu_{tc} = \nu_{rc} = \nu, \\ G_{rt} = G_{tc} = \alpha G = \alpha E / [2(1+\nu)], \quad G_{rc} = G = E / [2(1+\nu)] \end{aligned} \quad (33)$$

where E and ν are the Young's modulus and the Poisson's coefficient in the plane of isotropy and α is a parameter weighting the transverse isotropy. Applying the relationship (33), the elastic constants in the helicoidal system become

$$\begin{aligned} c_{11}^{hel} = c_{33}^{hel} = \frac{2G k_1 (\nu^2 - \alpha)}{\alpha - 1}, \quad c_{13}^{hel} = \frac{2G k_1 \nu (\nu + \alpha)}{1 - \alpha}, \\ c_{22}^{hel} = \frac{2G k_1 \alpha^2 (1 - \nu^2)}{1 - \alpha}, \quad c_{12}^{hel} = c_{23}^{hel} = \frac{2G k_1 \alpha \nu (1 + \nu)}{1 - \alpha}, \\ c_{55}^{hel} = G, \quad c_{44}^{hel} = c_{66}^{hel} = \alpha G, \end{aligned} \quad (34)$$

where $k_1 = (\alpha - 1) / [\alpha(\nu - 1) + 2\nu^2]$. The elastic constants in the cylindrical reference system are evaluated as functions of the elastic constants in the helicoidal one

$$\mathbf{C}^{cyl} = \mathbf{C}^{hel} + k_1 G \begin{bmatrix} \mathbf{C}^{(a)} \sin^4 \theta + \mathbf{C}^{(b)} \sin^2 \theta + \mathbf{C}^{(c)} \sin^2 \theta \sin(2\theta) + \\ + \mathbf{C}^{(d)} \sin(2\theta) + \mathbf{C}^{(e)} \sin^2(2\theta) \end{bmatrix} \quad (35)$$

where the matrix $\mathbf{C}^{(a)}, \mathbf{C}^{(b)}, \mathbf{C}^{(c)}, \mathbf{C}^{(d)}, \mathbf{C}^{(e)}$ are constituted by the following coefficients

$$\begin{aligned}
c_{22}^{(a)} &= c_{33}^{(a)} = c_{44}^{(a)} = k_2, & c_{23}^{(a)} &= -k_2, & c_{24}^{(c)} &= -k_2, & c_{34}^{(c)} &= k_2, \\
c_{12}^{(b)} &= 2\nu^2, & c_{13}^{(b)} &= -2\nu^2, & c_{22}^{(b)} &= \alpha(1+3\nu)(1-\nu) - \nu^2, & c_{23}^{(b)} &= k_2 \\
c_{33}^{(b)} &= 3\nu^2 + \alpha(3+\nu)(\nu-1), & c_{44}^{(b)} &= k_2, & c_{55}^{(b)} &= (\alpha-1)/k_2, \\
c_{66}^{(b)} &= (1-\alpha)/k_2, & c_{14}^{(d)} &= -\nu^2, & c_{24}^{(d)} &= \alpha\nu(\nu-1), \\
c_{34}^{(d)} &= \alpha(\nu-1) + \nu^2, & c_{56}^{(d)} &= (\alpha-1)/2k_2, & c_{22}^{(e)} &= c_{33}^{(e)} = -k_2/4, \\
c_{44}^{(e)} &= -k_2/4, & c_{23}^{(e)} &= k_2/4
\end{aligned} \tag{36}$$

The coefficients absent in the relationships (36) result zero.

By applying the equations (24), it is possible to evaluate the divergence of the displacement field in the two phases as

$$e^{(i)} = C_1^{(i)}(\theta)(1+\lambda^{(i)})r^{\lambda^{(i)}-1} + C_2^{(i)}(\theta)(1-\lambda^{(i)})r^{-(1+\lambda^{(i)})} + \frac{2C_4^{(i)}}{c_{11}^{(i)} - c_{22}^{(i)}} \tag{37}$$

CHAPTER VII

CONCLUSIONS AND FUTURE PERSPECTIVES

7.1 Conclusions

Many analytical and numerical approaches have been proposed in order to solve poroelastic problems describing the behavior of biological tissues. The main difficulty associated to numerical strategies concerns the solution of the *coupled* poroelastic equations for determining the solid response in terms of deformation and filtration. The proposal of this work is to find a strategy to numerically solve poroelastic problems employing the Finite Element Method (FEM). In particular, the strategy presented is based on the well known similarity between thermoelasticity and poroelasticity theories. This analogy allows to solve transient poroelastic problems as corresponding thermoelastic ones, interpreting the temperature as a pressure and thermal gradients as velocities. With this aim, the relationship between thermoelasticity and poroelasticity is formulated in terms of dimensionless parameters to ensure numerical stability, because the elasticity moduli, filtration coefficients and porosity have essentially different orders of magnitude. Thus, the dimensionless equations obtained are implemented in numerical FEM-based computations. Such transferring to equivalent thermoelastic problems enables to apply the FEM package ANSYS[®] 11, which provides opportunities to solve coupled thermoelastic problems in transient non linear settings.

7.2 Future Perspectives

The poroelasticity – thermoelasticity duality theory represents a fundamental tool to solve numerical problems describing the behavior of biological tissues. As illustrated in Chapter VI, the problem of the drug delivery to solid tumors has been modeled in the isotropic linear hypothesis. A following step might consist, thus, in the introduction of nonlinearities for both the permeability and elasticity. Besides, the therapeutic fluid agent is simply guided by pressure gradients, as described by Darcy's law, and, thus, also a diffusion process, described by Fick's law needs to be investigated. However, because the CED

technique represents a challenging approach to overcome the physiological barriers in brain tumors treatment, other several analyses are necessary to investigate, for example, the influence of different infusion protocols on drug effectiveness and on brain tissue failure or back-flow effects.

Moreover, with respect to the study presented in Chapter VI related to the influence of osteon trigonal microstructure on the mechanotransduction phenomena in bone, further interesting aspects could be investigated. In particular, two problems may be stressed. The first one is concerning the transient response of the poroelastic osteon to different load conditions, with the aim of analyzing the effect of load frequency on the mechanical behavior of the bone basic unit. The second study could be instead aimed to understand the role of osteon trigonal poroelastic features on the crack-propagation and crack-stopping across lamellae.

Poroelasticity theory can also be employed to model the mechanical arterial behavior. Despite recent advances on the anatomical description and measurements of the coronary tree and on the corresponding physiological, physical and numerical modeling aspects, the complete modeling of the arteries and veins is still out of reach. Therefore, in order to model blood perfusion in the cardiac tissue, the description should be limited to the detailed flows at a given space scale, simplifying the modeling of the smaller scale flows by aggregating these phenomena into macroscopic quantities, by some kind of “homogenization” procedure. To that purpose, the modeling of the fluid-solid coupling within the framework of porous media appears appropriate. Finite strain poroelastic models have already been proposed, albeit with ad hoc formulations for which compatibility with thermodynamics laws and incompressibility conditions is not established. Poroelastic models have also been considered in the framework of fluid structure interaction, e.g. to model blood vessel walls, with some extensions including drug transport. The FEM strategy proposed could be employed to perform parametrical analyses on arterial behavior.

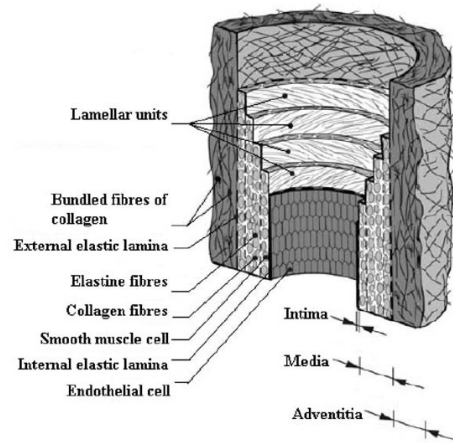


Figure 7.1

Diagrammatic scheme of the layered structure of the wall of elastic artery

However, the PTD could pave the way for a number of interesting applications, like the characterization of the viscoelastic properties of polymeric gels, such as agarose, and many biomaterials.

REFERENCES

- Allard E., Passirani C., Benoit JP., (2009), *Convection-enhanced delivery of nanocarriers for the treatment of brain tumors*, Biomaterials, 30, 2302-2318
- Ardizzoni A., (2001) *Osteocyte lacunar size-lamellar thickness relationships in human secondary osteons*, Bone, 28, 215-219
- Argoubi M., Shirazi-Adl A., (1996), *Poroelastic creep response analysis of a lumbar motion segment in compression*, Journal of Biomechanics, 29, 1331-1339
- Ascenzi A., Bonucci E., (1968) *The compressive properties of single osteons*, The Anatomical Record, 161, 377-391
- Ascenzi MG., Lomovtsev A., (2006) *Collagen orientation patterns in human secondary osteons, quantified in the radial direction by confocal microscopy*, Journal of Structural Biology, 153, 14-30
- Ateshian GA., Warden WH., Kim JJ., Grelsamer RP., Mow VC., (1997), *Finite deformation biphasic material properties of bovine articular cartilage from confined compression experiments*, Journal of Biomechanics, 30, 1157-1164
- Athanasίου KA., Natoli RM., (2008), *Introduction to Continuum Biomechanics*, Morgan & Claypool Publishers
- Bàca V., Kachlik D., Horák Z., Stingl J., (2007) *The course of osteons in the compact bone of the human proximal femur with clinical and biomechanical significance*, Surgical and Radiologic Anatomy, 29(3), 201-207
- Barou O., Mekraldi S., Vico L., Boivin G., Alexandre C., Lafage-Proust MH., (2002) *Relationship between Trabecular Bone Remodeling and Bone Vascularization: A Quantitative Study*, Bone, 30(4), 604-612

- Basser P.J., (1992), *Interstitial pressure, volume, and flow during infusion into brain tissue*, *Microvascular Research*, 44, 143-165
- Baxter L., Jain R.K., (1989), *Transport of fluid and macromolecules in tumors I. Role of interstitial pressure and convection*, *Microvascular Research*, 37, 77-104
- Beraudi A., Stea S., Montesi M., Baleani M., Viceconti M., (2009) *Collagen orientation in human femur, tibia and fibula shaft by circularly polarized light*, *Bone*, 44, S253-S338
- Biot MA., (1955) *Theory of elasticity and consolidation for a porous anisotropic solid*, *Journal of Applied Physics*, 26 (2), 182-185
- Boley BA., Weiner JH., (1997), *Theory of thermal stresses*, Dover Publications, INC., Minesola, New York
- Bonucci E., (2009) *The osteocyte: the underestimated conductor of the bone orchestra*, *Rendiconti Lincei Scienze Fisiche e Naturali*, 20, 237-254
- Cederbaum G., Li L., Schulgasser K., (2000), *Poroelastic Structures*, Elsevier
- Chen X., Sarntinoranont M., (2007), *Biphasic Finite Element Model of solute transport for direct infusion into nervous tissue*, *Annals of Biomedical Engineering*, 35, 2145-2158
- Cohen B., Lai WM., Mow VC., (1998), *A Transversely Isotropic Biphasic Model for Unconfined Compression of Growth Plate and Chondroepiphysis*, *Journal of Biomechanical Engineering*, 120, 491-496
- Cowin SC., Moss-Salentijn L., Moss ML., (1991) *Candidates for the Mechanosensory System in Bone*, *Journal of Biomechanical Engineering*, 113, 191-197
- Cowin SC., (2001), *Bone Mechanics Handbook*, CRC Press
- Cowin SC., (2002) *Mechanosensation and fluid transport in living bone*, *Journal of musculoskeletal & neuronal interactions*, 2(3), 256-260
- Cowin SC., Doty SB., (2007) *Tissue Mechanics*, Springer
- Cowin SC., Mehrabadi MM., (2007), *Compressible and incompressible constituents in anisotropic poroelasticity: The problem of unconfined compression of a disk*, *Journal of the Mechanics and Physics of Solids*, 55, 161-193

- Cowin SC., Gailani G., Benalla M., (2009) *Hierarchical poroelasticity: movement of interstitial fluid between porosity levels in bones*, Philosophical Transactions of the Royal Society A, 13, 367, 1902, 3401-3444
- Detourney E., Cheng AHD., (1993), *Fundamentals of poroelasticity*, in: *Comprehensive Rock Engineering: Principles, Practice & Projects*, Vol. II (J. A. Hudson, ed.) Pergamon, Oxford
- Franzoso G., Zysset PK., (2009) *Elastic Anisotropy of Human Cortical Bone Secondary Osteons Measured by Nanoindentation*, Journal of Biomechanical Engineering, 131, 021001-1/11
- Garcia JJ., Smith JH., (2008), *A Biphasic Hyperelastic Model for the Analysis of Fluid and Mass Transport in Brain Tissue*, Annals of Biomedical Engineering, 37, 375-386
- Heneghan P., Riches PE., (2008), *Determination of the strain-dependent hydraulic permeability of the compressed bovine nucleus pulposus*, Journal of Biomechanics, 41, 903-906
- Giraud-Guille MM., (1988) *Twisted plywood architecture of collagen fibrils on human compact bone osteons*, Calcified Tissue International, 42, 167-180
- Gross TS., Edwards JL., McLeod KJ., Rubin CT., (1997) *Strain Gradients correlate with sites of periosteal bone formation*, Journal of Bone and mineral Research, 12 (6), 982-988
- Gupta HS., Stachewicz U., Wagermaier W., Roscherger P., Wagner HD., Fratzl P., (2006) *Mechanical modulation at the lamellar level in osteonal bone*, Journal of Materials Research, 21(8), 1913-1921
- Han Y., Cowin SC., Schaffler MB., Weinbaum S., (2004), *Mechanotransduction and strain amplification in osteocyte cell processes*, PNAS, 101 (47), 16689-16694
- Hert J., Fiala P., Petrtyl M., (1994) *Osteon orientation of the diaphysis of the long bones in man*, Bone, 15(3), 269-277
- Hoc T., Henry L., Verdier M., Aubry D., Sedel L., Meunier A., (2006) *Effect of microstructure on the mechanical properties of Haversian cortical bone*, Bone, 38, 466-474

- Holmes MH., Mow VC., (1990), *The non linear characteristics of soft gels and hydrated connective tissues in ultrafiltration*, Journal of Biomechanics, 23, 1145-1156
- Huang J., Rapoff AJ., Haftka RT., (2006), *Attracting cracks for arrestment in bone-like composites*, Materials and Design, 27, 461-469
- Iatridis JC., Setton LA., Foster RJ., Rawlins BA., Weidenbaum M., Mow VC., (1998), *Degeneration affects the anisotropic and non linear behaviors of human anulus fibrosus in compression*, Journal of Biomechanics, 31, 535-544
- Ivanchenko O., Sindhvani N., Linninger A., (2010), *Experimental techniques for studying poroelasticity in brain phantom gels under high flow microinfusion*, Journal of Biomechanical Engineering, 132, 1-8
- Jain R.K., (1988), *Determinants of tumor blood flow: a review*, Cancer Research, 48, 2641
- Jasiuk I., Ostoja-Starzewski M., (2004) *Modeling of bone at a single lamella level*, Biomechanics and Modeling in Mechanobiology, 3, 67-74
- Kerr JF., Wyllie AH., Curie AR., (1972), *Apoptosis: a basic biological phenomenon with wide-ranging implications in tissue kinetics*, British Journal of Cancer, 26, 239-257
- Knothe Tate ML., (2003) *Whither flows the fluid in bone? An osteocyte's perspective*, Journal of Biomechanics, 36, 1409-1424
- Lai WM., Mow VC., (1980), *Drag-induced compression of articular cartilage during a permeation experiment*, Biorheology, 17, 111-123
- Lemaire T., Naili S., Rémond A., (2006) *Multiscale analysis of the coupled effects governing the movement of interstitial fluid in cortical bone*, Biomechanics and Modeling in Mechanobiology, 5, 39-52
- Lenz C., Nackenhorst U., (2004) *A numerical approach to mechanosensation of bone tissue based on a micromechanical analysis of a single osteon*, PAMM., 4, 342-343
- Li, X.G., von Holst, H., Ho, J., Kleiven, S. *Three Dimensional Poroelastic Simulation of Brain Edema: Initial Studies on Intracranial Pressure*, Proceedings of World Congress on Medical Physics and Biomedical Engineering, September 7 - 12, 2009, Munich, Germany., Vol. 25/4, pp. 1478-1481.

- Linninger A.A., Somayaji M.R., Erickson T., Guo X., Penn R.D., (2008), *Computational methods for predicting drug transport in anisotropic and heterogeneous brain tissue*, Journal of Biomechanics, 41, 2176-2187
- Marotti G., Muglia MA., (1988) *A scanning electron microscope study of human bony lamellae. Proposal for a new model of collagen lamellar organization*, Archivio italiano di Anatomia e Embriologia, 93(3), 163-176
- Martin RB., Boardman DL., (1993) *The effects of collagen fiber orientation, porosity, density, and mineralization on bovine cortical bone bending properties*, Journal of Biomechanics, 26, 1047-1054
- Martin RB., Gibson VA., Stover SM., Gibeling JC., Griffin LV., (1996) *Osteonal Structure in the Equine Third Metacarpus*, Bone, 19(2), 165-171
- Mehrabadi MM., Cowin SC., Jaric J., (1995) *Six-dimensional orthogonal tensor representation of the rotation about an axis in three dimensions*, International Journal Solids Structures, 32, 439-449
- Minchinton AI., Tannock IF., (2006), *Drug penetration in solid tumors*, Nature Reviews, 6, 583-592
- Mohsin S., O'Brien FJ., Lee TC., (2006), *Osteonal crack barriers in ovine compact bone*, Journal of Anatomy, 208, 81-89
- Mollica F., Jain R.K., Netti P.A., (2003), *A model for temporal heterogeneities of tumor blood flow*, Microvascular Research, 65, 56-60
- Mow VC., Kuei SC., Lai WM., Armstrong CG., (1980), *Biphasic creep and stress relaxation of articular cartilage in compression: Theory and experiments*, Journal of Biomechanical Engineering, 102, 73-84
- Netti P.A., Baxter L.T., Boucher Y., Skalak R., Jain R.K., (1995), *Time-dependent behavior of interstitial fluid pressure in solid tumors: implications for drug delivery*, Cancer Research, 55, 5451-5458
- Netti P.A., Roberge S., Boucher Y., Baxter L.T., Jain R.K., (1996), *Effect of Transvascular fluid exchange on pressure-flow relationship in tumors: a proposed mechanism for tumor blood flow heterogeneity*, Microvascular Research, 52, 27-46

- Netti P.A., Baxter L.T., Boucher Y., (1997), *Macro- and Microscopic fluid transport in living tissues: application to solid tumors*, AICHE Journal, 43, 818-834
- Netti P.A., Travascio F., Jain R.K., (2003), *Coupled Macromolecular Transport and Gel Mechanics: Poroviscoelastic Approach*, AICHE Journal, 49(6), 1580-1596
- O'Brien FJ., Taylor D., Lee TC., (2007) *Bone as a composite material: The role of osteons as barriers to crack growth in compact bone*, International Journal of Fatigue, 29, 1051-1056
- Qin YX., Kaplan T., Saldanha A. Rubin C., (2003) *Fluid pressure gradients, arising from oscillations in intramedullary pressure, is correlated with the formation of bone and inhibition of intracortical porosity*, Journal of Biomechanics, 36, 1427–1437
- Raghavan R., Brady ML., Rodriguez-Ponce MI., Hartlep A., Pedain C., Sampson JH., (2006), *Convection-enhanced delivery of therapeutics for brain disease, and its optimization*, Neurosurgery focus, 20(3), 1-13
- Ramasamy JG., Akkus O., (2006) *Local variations in the micromechanical properties of mouse femur: The involvement of collagen fiber orientation and mineralization*, Journal of Biomechanics, 40, 910-918
- Reddy LH., (2005), *Drug delivery to tumors: recent strategies*, Journal of Pharmacy and Pharmacology, 57, 1231-1242
- Reisinger AG., Pahr DH., Zysset PK., (2010) *Sensitivity analysis and parametric study of elastic properties of an unidirectional mineralized bone fibril-array using mean field methods*, Biomechanics and Modeling in Mechanobiology
- Reisinger AG., Pahr DH., Zysset PK., (2010) *Elastic anisotropy of bone lamellae as a function of fibril orientation pattern*, Biomechanics and Modeling in Mechanobiology
- Rémond A., Naïli S., Lemaire T., (2008) *Interstitial fluid flow in the osteon with spatial gradients of mechanical properties: a finite element study*, Biomechanics and Modeling in Mechanobiology, 7, 487–495.
- Rho JY., Khun-Spearing L., Zioupos P., (1998) *Mechanical Properties and the hierarchical structure of bone*, Medical Engineering & Physics, 20, 92-102

- Rho JY., Zioupos P., Currey JD., Pharr GM., (1999) *Variations in the individual thick lamellar properties within osteons by nanoindentation*, Bone, 25, 295-300
- Riches PE., Dhillon N., Lotz J., Woods AW., McNally DS., (2002), *The internal mechanics of the intervertebral disc under cyclic loading*, Journal of Biomechanics, 35, 1263-1271
- Roose T., Netti PA., Munn LL., Boucher Y., Jain RK., (2003) *Solid stress generated by spheroid growth estimated using a linear poroelasticity model*, Microvascular Research, 66, 201-212
- Rüggeberg M., Speck T., Paris O., Lapierre C., Pollet B., Koch G. Burgert I., (2008) *Stiffness gradients in vascular bundles of the palm Washingtonia robusta*, Philosophical Transactions of the Royal Society B, 275, 2221–2229
- Ruimerman R., Van Rietbergen B., Hilbers P., Huiskes R., (2005) *The effects of Trabecular-Bone Loading Variables on the Surface Signaling Potential for Bone Remodeling and Adaptation*, Annals of Biomedical Engineering, 33(1), 71-78
- Rutkowski JM., Swartz MA., (2007), *A driving force for change: interstitial flow as a morphoregulator*, Trends in Cell Biology, 17, 44-50
- Sampson J.H., Akabani G., Archer G.E., Berger M.S., Coleman R.E., Friedman A.H., Friedman H.S., Greer K., Herndon II J.E., Kunwar S., McLendon R.E., Paolino A., Petry N.A., Provenzale J.M., Reardon D.A., Wong T.Z., Zalutsky M.R., Pastan I., Bigner D.D., (2008), *Intracerebral infusion of an EGFR-targeted toxin in recurrent malignant brain tumors*, Neuro-Oncology, 10(3), 320-329
- Skedros JG., Mendenhall SD., Kiser CJ., Winet H., (2009) *Interpreting cortical bone adaptation and load history by quantifying osteon morphotypes in circularly polarized light images*, Bone, 44, 392-403
- Smit TH., Burger EH., Huyghe JM., (2002), *A case for strain-induced fluid flow as a regulator of BMU-coupling and osteonal alignment*, Journal of Bone and Mineral Research, 17(11), 2021-2029
- Smith J.H., Humphrey J.A.C., (2007), *Interstitial transport and transvascular fluid exchange during infusion into brain and tumor tissue*, Microvascular Research, 73, 58-73

- Soltz MA., Ateshian GA., (1998), *Experimental verification and theoretical prediction of cartilage interstitial fluid pressurization at an impermeable contact interface in confined compression*, Journal of Biomechanics, 31, 927-934
- Terzaghi K., (1943), *Theoretical Soil Mechanics*, Wiley, New York
- Urciuolo F., Imperato G., Netti PA., (2008), *Effect of Dynamic Loading on Solute Transport in Soft Gels Implication for Drug Delivery*, AIChE Journal, 54, 824-834
- Velardi F., Fraternali F., Angelillo M., (2006), *Anisotropic constitutive equations and experimental tensile behavior of brain tissue*, Biomechanical Modeling in Mechanobiology, 5, 53-61
- Vogelbaum MA., (2007), *Convection enhanced delivery for treating brain tumors and selected neurological disorders: symposium review*, Journal of Neuro-Oncology, 83, 97-109
- Wagermaier W., Gupta HS., Gourrier A., Burghammer M., Roscheger P., Fratzl P., (2006) *Spiral twisting of fiber orientation inside bone*, Biointerphases, 1(1), 1-5
- Walker W.L., Cook J., (1996), *Drug delivery to brain tumors*, Bulletin of Mathematical Biology, 58(6), 1047-1074
- Weiner S., Traub W., Wagner HD., (1999) *Lamellar Bone: Structure-Function Relations*, Journal of Structural Biology, 126, 241-255
- Yuan F., (1998), *Transvascular drug delivery in solid tumors*, Seminars in Radiation Oncology, 8(3), 164-175
- Yoon YJ., Cowin SC., (2008) *The estimated elastic constants for a single bone osteonal lamella*, Biomechanics and Modeling in Mechanobiology, 7, 1-11
- Yoon YJ., Cowin SC., (2008) *An estimate of anisotropic poroelastic constants of an osteon*, Biomechanics and Modeling in Mechanobiology, 7, 13-26
- Zimmerman RW., (2000), *Coupling in poroelasticity and thermoelasticity*, International Journal of Rock Mechanics and Mining Sciences, 37, 79-87